Politecnico di Milano

School of Civil, Environmental and Land Management Engineering

Physics-based numerical simulations to study the seismic response of the Mexico City basin

A Thesis Submitted in Partial Fulfilment
of the Requirements for the Degree of

Master of Science in Civil Engineering

by

Victor Moises Hernández Aguirre
912762

Advisor:
Prof. Roberto Paolucci

Co-Advisor:
Prof. Ilario Mazzieri

Academic Year 2020-2021

To the memory of my beloved father.
Thank you for all the sacrifices you made and
for the invaluable lessons that you taught me.

Acknowledgements

I would first like to extend my deepest gratitude to my supervisor, Prof. Roberto Paolucci, for his invaluable advice, insightful suggestions and mentorship. Without his persistent help, the goal of this project would not have been realized.

I am indebted to Ilario Mazzieri for the patient guidance and continuous support in the construction of the numerical mesh and on the use of SPEED. His willingness to give his time so generously has been very much appreciated.

I am also grateful to Chiara Smerzini for the support on the way. I'd also like to recognize the assistance with SPEED that at some point I received from Karim, Maria and Srihari, and their contributions to the development of 3PTOOL.

I very much appreciate the time and interest that Prof. Ezio Faccioli has put in the revision of this work.

I gratefully acknowledge the funding received from the Mexican Consejo Nacional de Ciencia y Tecnología, to undertake my studies at Politecnico di Milano.

My appreciation also goes out to my friends in Milano and back in Mexico, for their encouragement and support in difficult moments. Especially to those that are not here anymore.

Hannah, thank you for your unfailing support and for sharing this adventure with me.

Finally, my deep and sincere gratitude to my family for their continuous love, help and support. I am grateful to my brother and my parents for always being there for me and for giving me the opportunities and experiences that have made me who I am. This accomplishment would not have been possible without them.

Abstract

Mexico City is one of the cities with the highest seismic risk worldwide. This is mainly because of the complicated seismotectonic environment of Mexico and the well-known large amplification of ground motion caused by the extremely soft clay deposits found in the Mexico City basin and the underlying consolidated deposits.

The primary purpose of this thesis is to investigate whether or not it is possible to generate realistic synthetic ground motions in the low-frequency range for the Mexico City basin, using 3D physics-based numerical simulations with a seismic point source representing a local crustal earthquake.

In the first part of the thesis, the most important characteristics of the ground motion in Mexico City induced by the September 19, 1985 and the September 19, 2017 earthquakes, which have been the most destructive, were analyzed. Then, a 3D numerical model for Mexico City was constructed considering the main features of the basin's lacustrine sediments. The 3D model was employed to carry out numerical simulations using the high-performance spectral element code SPEED. Results were validated against available records from a Mw3.0 local earthquake. In general, a fair and good fit with records was obtained using a hysteretic damping model. After some slight modifications, this model could be used for the simulation of ground motions during larger magnitude earthquakes.

The numerical results suggest that higher-mode surface waves dominate the wavefield in the lake zone of Mexico City, as evident from the measured phase velocities and vertical displacements along vertical arrays. This implies that surface waves mainly propagate in the consolidated deposits. Since in the deep deposits the attenuation is much smaller than for the superficial clay, surface waves can propagate long distances. The role of the soft clay deposits is that of amplifying the ground motion.

Keywords: 3D Physics-based numerical simulations; Mexico City Basin; Site effects; Earthquakes; Surface waves.

Contents

Acknowledgements i

Abstract iii

Contents vi

List of figures xv

List of tables xvii

1 Introduction 1
- 1.1 Background . . . 1
- 1.2 The unusual case of Mexico City . . . 5
- 1.3 Aim and Objectives . . . 7
- 1.4 Thesis organization . . . 8

2 Seismicity in Mexico and Site Effects in Mexico City 11
- 2.1 Seismotectonic environment in Mexico . . . 11
- 2.2 Seismicity in the Mexico basin . . . 15
- 2.3 Significant historical earthquakes in Mexico . . . 17
- 2.4 Geotechnical characterization of Mexico City's subsoil . . . 21
  - 2.4.1 Stratigraphy and geotechnical zonification . . . 23
  - 2.4.2 Dynamic properties . . . 26
  - 2.4.3 Subsidence . . . 29
- 2.5 The September 19, 1985 M_S8.1 earthquake . . . 31
- 2.6 The September 19, 2017 Mw7.1 earthquake . . . 45

3 3D Physics-Based Numerical Simulations 55
- 3.1 Introduction . . . 55
- 3.2 SPEED: SPectral Elements in Elastodynamics with Discontinuous Galerkin . . . 58
- 3.3 Seismic Source in SPEED . . . 65

3.3.1 Point source 65
3.3.2 The Kinematic dislocation model 68
3.4 Construction of the 3D Model for Mexico City 69
3.5 Validation case study: Mw3.0 July 17, 2019 earthquake 76
3.6 Calibration with hill zone records 78

4 Analysis of results **81**
4.1 Results for case 3D-Qv 81
4.1.1 Comparison with records 86
4.1.2 Surface waves 91
4.2 Results for case 3D-Qh 97
4.2.1 Comparison with records 100
4.2.2 Surface waves 103
4.3 Comparison and Discussion 104

5 Conclusions **109**

Bibliography **113**

Appendices **125**

A Basic Engineering Seismology Concepts **127**
A.1 Seismic waves 128
A.2 Strong ground motion 130
A.3 Ground motion prediction equations 132
A.4 Response spectrum 133
A.5 One-dimensional ground response analysis 134

List of Figures

1.1 Global Seismic Risk Map. The main map presents the geographic distribution of average annual loss (USD) normalized by the average construction costs of the respective country. In the lower panel there are three maps: (i) a global seismic hazard map showing Peak Ground Acceleration (PGA) with a 10% probability of being exceeded in 50 years for rock conditions; (ii) a global exposure map depicting the distribution of residential, commercial and industrial buildings; and (iii) a map depicting an estimate of average annual human losses due to earthquake induced structural collapse of buildings. The black circle encloses the location of Mexico. [From Silva et al. (2018)]. 4

1.2 View of Mexico City. [Source: www.flickr.com/photos/eneas]. . . . 5

1.3 Epicenters of the earthquakes with magnitude M>6 that took place in Mexico during the period 1950-2020. The epicenters of the earthquakes of September 19, 1985 and September 19, 2017 are highlighted. [Source: earthquake.usgs.gov]. 6

2.1 Geodynamic setting and main continental magmatic provinces of Mexico. MAT: Middle American Trench; TMVB: Trans-Mexican Volcanic Belt. [Adapted from Ferrari et al. (2012)]. 12

2.2 Cross section through a subduction zone before an earthquake (above) and during an earthquake (below). [From Hyndman and Wang (1995)]. 12

2.3 Composite model: tomographic and RF image showing the flat and descending segments of the slab (purple line). The key features are the flat under-plated subduction for 250 km, and the location and truncation of the slab at 500 km. The zone separating the ocean crust from the continental Moho is estimated to be less than 10 km in thickness. NA = North America, C = Cocos, LC = lower crust, LVM = low velocity mantle, OC = oceanic crust. The contour lines indicate wave speed. [From Pérez-Campos et al. (2008)]. 14

2.4 Geology and Tectonics of the Mexico Basin. [Modified from Santoyo-Villa et al. (2005)]. 15

2.5 Digital elevation model (DEM) of the Mexico Basin area showing faults and focal mechanisms of earthquakes in the region. Black thick contour encloses Mexico City. [From Singh et al. (2020)]. . . 16
2.6 Collapsed buildings in Mexico City after the September 19, 1985 earthquake. a) Hotel Regis [Source:La Jornada], b) Administrative building [Source:Munich-Re]. 18
2.7 Location of the most important earthquakes in Mexico since 1900. [From Servicio Sismológico Nacional (2017)]. 19
2.8 Collapsed buildings in Mexico City after the September 19, 2017 earthquake. a) Building at Medellin 176 b) Building at Simon Bolívar 190. [Source:ProtoplasmaKid/WikimediaCommons /CC-BY-SA4.0]. 20
2.9 E-W Geological section crossing Mexico City [Adapted fromSantoyo-Villa et al. (2005)]. 22
2.10 The Mexico basin lakes as the Spanish found them in 1519. Nowadays there is only one small lake near Xochimilco. [Adapted from DDF (1975)]. 23
2.11 A typical section of the stratigraphic sequence of Mexico City. [Adapted from Santoyo-Villa et al. (2005)]. 24
2.12 Contour map of the contact between clay and deep deposits. [From Juárez-Camarena et al. (2016)]. 24
2.13 Depth contours of the estimated pre-Chichinautzin basin topography. [Adapted from Cruz-Atienza et al. (2016)]. 25
2.14 Geotechnical zoning map for Mexico City according to the building code. Zone I=Hills, Zone II=Transition, Zone III=Lake bed. [Adapted from GCDMX (2017)]. 26
2.15 Experimental shear modulus degradation and damping curves of samples retrieved from the former Texcoco Lake zone. [From Mayoral et al. (2016)]. 27
2.16 V_S profiles (below) obtained from down-hole and P-S suspension logging tests located at different sites in the lake zone (above) as reported by Jaime (1987). 28
2.17 Evolution of subsidence in the Historic Center of Mexico City during the period 1898-2005. [From Auvinet et al. (2013)]. 29
2.18 Changes in V_S from P-S suspension logging tests performed in 1986 and 2000 at SCT site (left), and change in G_{max} from resonant column and cyclic triaxial tests on samples retrieved from the same site (right). [From Ovando-Shelley et al. (2007)]. 30
2.19 Maps of T_0 for Mexico City in (a) 1985 and (b) 2010. [From Arroyo et al. (2013)]. 31

2.20 Locations of strong motion stations in Guerrero array on 19 September 1985. Short dashed lines show limits of aftershocks of large earthquakes in this region since 1951. Peak ground accelerations (cm/s^2)are given for each station for the north, east and vertical components, respectively, in parentheses. [From Anderson et al. (1986)]. 32

2.21 Ground motion stations active in Mexico City during the 1985 Michoacán earthquake. 33

2.22 North-south component of acceleration for statios Caleta de Campos and La Villita (left) and their corresponding Fourier amplitude spectra (right). 34

2.23 Peaks of horizontal components of acceleration plotted against distance outside the boundary of the aftershock zone. [Adapted from Anderson et al. (1986)]. 34

2.24 E-W accelerograms for three sites in the Mexico City (left). E-W and N-S elastic acceleration response spectra (5% damping) for the same sites (right). 35

2.25 Spectral ratios from the horizontal components of motions at the SCT (left) and CDAO (right) stations with respect to the TACY station. 36

2.26 Collapsed buildings in Mexico City during the 1985 Michoacán earthquake (yellow dots) placed on the map of estimated T_0 for 1985 (Arroyo et al., 2013). 37

2.27 Ground velocity and displacement at Caleta de Campos during the 19 September earthquake derived from accelerograms. [From (Anderson et al., 1986)]. 38

2.28 Vertical displacement records obtained at different sites in Mexico City, showing ripples with periods of about 2-3 sec superposed to longer waves. [After Mena et al. (1986)]. 39

2.29 Transfer function for SCT site considering a clay layer over an elastic half-space. 40

2.30 Comparison between observed and predicted transfer functions for CDAO and SCT sites using a 1D model with the geotechnical profiles proposed by Seed et al. (1988). [After Kawase and Aki (1989)]. . . 41

2.31 Recorded and synthetic accelerograms (NS component) at a) CDAO and b) SCT stations. Modeling was performed with one-dimensional Haskell's method. [From Sanchez-Sesma et al. (1988)]. 42

2.32 2D model of the large scale structure of Mexico City valley proposed by Bard et al. (1988). 43

2.33 (a) Tectonic context. Black squares are epicenters from seismicity in the month of September 2017. Normal faulting focal mechanisms for previous large events in 1980 and 1999 and for the 2017 Mw8.2 Tehuantepec earthquake are shown. The black contours are the 20 km slab depths from Ferrari et al. (2012). White star is the hypocenter for the 2017 Puebla-Morelos earthquake. (b) Slip model, the white star is the event hypocenter. Color scale is the same as in (a). (c) Source time function for the slip model. [From Melgar et al. (2018)]. 45

2.34 Ground motion stations active in Mexico City during the 2017 Puebla-Morelos earthquake. Values in white color represent the PGA (in gals) for the each station. 46

47figure.caption.47

2.36 (a,b) North–south and east-west accelerograms, recorded at CU station (hill zone), of the 1985 M_S8.1 Michoacán earthquake, (c,d) and the 2017 M_w7.1 Puebla-Morelos earthquake. (e) Fourier amplitude spectra (geometric mean of the two horizontal components) at SCT of the two earthquakes. (f) Geometric mean of elastic response spectra (5% damping) at SCT of the two earthquakes. There is a clear difference in the frequency content; the FAS of the 1985 event (interplate) is peaked between 0.3 and 0.7 Hz, whereas that of the 2017 earthquake (intraslab) is peaked between 0.6 and 1.1 Hz. 48

2.37 (a,b) North–south and east-west accelerograms, recorded at SCT station (lake zone), of the 1985 M_S8.1 Michoacán earthquake, (c,d) and the 2017 M_w7.1 Puebla-Morelos earthquake. (e) Fourier amplitude spectra (geometric mean of the two horizontal components) at SCT of the two earthquakes. (f) Geometric mean of elastic response spectra (5% damping) at SCT of the two earthquakes. 49

2.38 Recorded response spectra during the Puebla-Morelos 2017 earthquake for the different seismic zones. The higher SA were measured in the transition and IIIa seismic zones, where most of the buildings collapsed. [From Mayoral et al. (2019)]. 50

2.39 Zoom to the Roma and Condesa neighborhoods. Black dots represent the collapsed buildings, while green dots represent severely damaged buildings. 51

2.40 E-W accelerograms at stations CI05 (a) and CO56 (b). c) Amplification functions of the E-W component of stations CI05 and CO56 with respect to station TACY (hill zone). d) SA of the E-W component of stations CI05 and CO56. 52

2.41 Design spectra in force during the Puebla-Morelos 2017 earthquake for different dominant site periods, according to the 2004 Mexico City's building code. 52

2.42 Collapsed building with flat slab system at Viaducto Miguel Alemán 106, Piedad-Narvarte, before the 2017 Puebla-Morelos earthquake (left) and after the earthquake (right). [From Galvis et al. (2017)]. 53

2.43 a) Residential building collapsed due to soft first story at Balsas 18, Miravalle, before the 2017 Puebla-Morelos earthquake (left) and after the earthquake (right). [From Galvis et al. (2017)]. 53

3.1 Overview of approaches for earthquake ground motion prediction. [From Paolucci et al. (2014)]. 56

3.2 Sketch of an idealized model for physics-based numerical simulation of earthquake ground motion. These models encompass a properly characterized seismic source, the propagation path through heterogeneous earth media and site or soil-structure interaction effects. [From Smerzini (2010)]. 57

3.3 Procedure to generate 3D numerical Simulations. [From Infantino (2016)]. 59

3.4 Examples of different mesh algorithms: a) structured, b) unstructured, c) conforming and d) non-conforming. [From Smerzini (2010)]. 62

3.5 3D example of non-conforming domain decomposition. The whole domain is composed of different non-overlapping polygonal subdomains, made by hexahedral elements. Discontinuous Galerkin discretization allows to deal with a nonuniform polynomial degree distribution (**N**-adaptivity, e.g.,$\mathbf{N}_1 = 2$ in Ω_1 and $N_2 = 3$ in Ω_2), as well as a locally varying mesh size (**h**-adaptivity between subdomains $\Omega_1, \Omega_2, \Omega_3$ and Ω_4). [From Mazzieri et al. (2013)]. 63

3.6 a) Schematic diagram of rupture front spreading from the hypocenter over the fault plane. The expansion of the rupture area results in a space and time varying dislocation function $\Delta u(\underline{x}, t)$. b) Definition of conventional parameters used to indicate fault orientation and slip direction. [From Smerzini (2010)]. 66

3.7 The nine different force couples constituting the seismic moment tensor **M**. [From Aki and Richards (2002)]. 66

3.8 Example of slip and slip rate functions: physical meaning of the rise time τ_R. [From Smerzini (2010)]. 67

3.9 Numerical modeling of an extended seismic source. The fault plane is subdivided into a number of subfaults, defined by a set of spectral nodes at locations $\underline{x}_s^n$. Each subsource is characterized by its own parameters. [From Smerzini (2010)]. 69

3.10 Digitized depth contours of the deep deposits in QGIS, shown over the DEM of the Mexico basin. 71

3.11 Vertically exaggerated (x30) surface for the lower boundary of the clay deposits. 72

3.12 Shear-wave velocity V_S as a function of depth below CUP5 (hill zone). [Adapted from Singh et al. (1995)]. 72
3.13 Assumed clay V_S profiles for CUPJ and SCT sites. 73
3.14 Variation with depth of V_S and V_P for the deep deposits. 74
3.15 Initially created discontinuous mesh for the Mexico City area. . . . 75
3.16 3D mesh for the Mexico City area consisting of 2'446'082 spectral elements with N=5. 76
3.17 Ground motion stations active during the 17/07/2019 Mw3.0 earthquake. Values in white color represent the PGA for the NS, EW and Z components (in cm/s^2) for the corresponding station. The red star represents the epicenter of the event. 77
3.18 Vertical, north–south and east-west accelerograms, recorded at MHVM station during the 17/07/2019 Mw3.0 earthquake. [From SSN (2019)]. 78
3.19 Focal mechanism for the 17/07/2019 Mw3.0 earthquake. [From SSN (2019)]. 78
3.20 Evaluated slip velocity functions for the seismic source. 79
3.21 Comparison between synthetics (computed with the Hisada method) and records, for stations MHVM, TACY and CUP5. On the left side velocity traces are shown (low-pass filtered at 2 Hz), while on the right side FAS of accelerations are presented. The crustal model in Table 3.1 was used, taking V_S=750 m/s for the first 200 m. The good agreement using the focal mechanism estimated by Singh et al. (2020) is evident. 80

4.1 Comparison between computed (from simulation 3D-Qv) and recorded FAS of acceleration at some stations in the lake zone. From this results it is considered that the mesh is able to propagate frequencies up to 1.3 Hz. 82
4.2 Snapshots of velocity (E-W component) from simulation 3D-Qv. Amplification, diffraction and generation of surface waves at the basin edges are clearly observed. 83
4.3 Spatial distribution of the geometric mean of the horizontal components (gmh) of PGA from simulation 3D-Qv. 83
4.4 Spatial distribution of PGV from simulation 3D-Qv for components E-W and N-S, with superimposed velocity traces extracted at some stations. A two-lobed radiation pattern is evident. 84
4.5 Spatial distribution of the gmh spectral acceleration (Sa) at T=0.5 s and 1 s, from simulation 3D-Qv. 87
4.6 Comparison between computed (from simulation 3D-Qv) and recorded velocity time-histories and their corresponding FAS, at some stations in the hill and transition zones. 89

4.7 Comparison between computed (from simulation 3D-Qv) and recorded velocity time-histories and their corresponding FAS, at some stations in the lake zone. 90

4.8 Goodness-of-Fit for simulation 3D-Qv. Left: GoF scores computed on the gmh of PGA, PGV, PGD, and Sa at T = 0.5, 1.0, 1.5, and 2.0 s. Right: map of the mean GoF scores. 92

4.9 Dots represent the normalized vertical displacement measured by Shapiro et al. (2001) at different depths at four locations in the lake-bed zone, while the theoretical eigenfunctions for the Rayleigh waves fundamental mode and first overtone are represented by the black and blue lines, respectively. This experimental evidence shows that the wavefield in the lake-bed zone bed zone is dominated by higher-mode surface waves. 93

4.10 Dispersion curves of the Rayleigh waves phase velocity for two representative 1D profiles within the basin (shallow and deep sites). . 93

4.11 Upper panel: Map of Mexico City showing location of Section A for which a seismogram was extracted, and the points where vertical arrays were placed. Lower panel: Normalized seismic profiles of the E-W displacement along Section A, for simulation 3D-Qv at 0.5 Hz. The computed Rayleigh waves phase velocities correspond to the fundamental mode and first overtone. 94

4.12 Distribution with depth of vertical displacements for simulation 3D-Qv (at 0.5 Hz), for the three arrays shown in Figure 4.11. The amplitude of displacements remains nearly constant with depth, confirming that higher mode surface waves dominate the ground motion within the basin. 95

4.13 Dispersion curves of the Love waves phase velocity for a representative 1D profile at the basin center. 96

4.14 Normalized seismic profiles of the N-S displacement along Section A, for simulation 3D-Qv at 0.5 Hz. The observed Love waves phase velocities correspond to the first overtone. 96

4.15 Snapshots of velocity (E-W component) from simulation 3D-Qh. Amplification, diffraction and generation of surface waves at the basin edges are clearly observed. 97

4.16 Spatial distribution of PGV from simulation 3D-Qh for components E-W and N-S, with superimposed velocity traces extracted at some stations. A two-lobed radiation pattern is evident. 98

4.17 Comparison between computed (from simulation 3D-Qh) and recorded velocity time-histories at some stations in the lake zone. 100

4.18 Comparison between computed (from simulation 3D-Qh) and recorded velocity time-histories at some stations in the hill and transition zones. 101

4.19 Goodness-of-Fit for simulation 3D-Qh. Left: GoF scores computed on the gmh of PGA, PGV and PGD. Right: map of the mean GoF scores. 102
4.20 Normalized seismic profiles of the E-W displacement along Section A, for simulation 3D-Qh at 0.5 Hz. The observed Rayleigh waves phase velocities correspond to the fundamental mode and first overtone. 103
4.21 Particle motion trajectories in the radial-vertical plane for stations CI05 (left) and BA49 (right). Displacements are low-pass filtered at 1.3 Hz. 104
4.22 Representative spectral element for the uppermost part of the basin. LGL nodes are shown with small circles (for degree n=5). Using the not-honoring technique, clay mechanical properties are assigned to the LGL nodes above the clay basin surface. 105
4.23 Comparison of velocity time-histories and their corresponding FAS, between simulations 3D-Qv and 3D-Qh, at station CUP5 in the hill zone. 105
4.24 Comparison between normalized seismic profiles of the E-W displacement along Section A, for simulations 3D-Qv (upper panel) and 3D-Qh (lower panel). Results were low-pass filtered at 1.3 Hz. 106
4.25 Cross-section (with coordinate Y=2'146'000) with V_S values. The shape of the basin is clearly seen and the location of the hypocenter is shown with a red star. 107

A.1 (a) Diagram of the layers forming the Earth: crust, mantle, outer core and inner core; and (b) tectonic plates forming the Lithosphere. 127
A.2 Main types of faults causing earthquakes. 128
A.3 Deformations produced by body waves: (a) P-wave; (b) SV-wave. [From Kramer (1996)]. 129
A.4 Deformations produced by surface waves: (a) Rayleigh wave; and (b) Love wave. [From Kramer (1996)]. 130
A.5 Geometric dispersion of surface waves in vertically heterogeneous media: (a) qualitative sketch of amplitude decay of the fundamental mode at different wavelength; (b) dispersion curve in the wavelength-phase velocity domain; and (c) dispersion curve in the frequency-phase velocity domain. [From Foti et al. (2018)]. 130
A.6 (a) Accelerograms from events with different magnitude in the Pacific coast of Mexico, recorded at about 25 km from the corresponding epicenter; and (b) Fourier amplitude spectra for the same accelerograms. [From Anderson and Quaas (1988)]. 132
A.7 Single degree of freedom system (SDOF). 134

A.8 Response spectrum. Spectral accelerations are the maximum acceleration amplitudes of SDOF systems in response to the same input motion. The response spectrum is obtained by plotting the spectral accelerations against the periods of vibrations of the SDOF systems. [From Kramer (1996)]. 135
A.9 Geometry of the soil layer overlying an elastic halfspace. 136
A.10 Transfer function for a soil layer overlying an elastic half-space. . . 138

List of Tables

2table.caption.6
2.1 Earthquakes reported by the Mexican National Seismological Service with epicenter in Mexico City and magnitude M≥3, during the period 2010 - 2020 (SSN, 2020). 17
2.2 Subduction earthquakes with magnitude M≥7.5, reported by the SSN since 1900 (SSN, 2020). 20
2.3 Most important intermediate and deep earthquakes, with inland epicenters, reported by the SSN (SSN, 2020). 21

3.1 Crustal model. 71

Chapter 1

Introduction

1.1 Background

In the past two decades, earthquakes and tsunamis were the deadliest form of disasters accounting for 58% of total deaths, killing over 700,000 people worldwide. Low-income countries had the highest average number of deaths per disaster event. The relatively better risk governance, infrastructure, surveillance systems, and reduced exposure is likely responsible for the improved protection in countries as income levels increase (CRED, 2020).

Earthquakes can also cause enormous financial losses, as shown in Table 1.1. As a matter of fact, losses in the two-digit billion dollar range have become a reality. For instance, comparing the 1995 Kobe and the 2011 Tohoku earthquakes in Japan, the loss statistics shows a factor 3 increase for the economic loss, and a factor 13 for the insured loss (Paolucci et al., 2014). It appears likely that in industrialized countries, disaster losses have grown with population and economic growth, but have not increased significantly as a portion of national wealth (White et al., 2001). However, compared to GDP (Gross Domestic Product), losses are proportionately more impactful in poorer nations worldwide. For instance, the losses caused by the 2010 Haiti earthquake were 120 percent of the Haiti's GDP in the previous year (HRW, 2011), while for the 2011 Tohoku earthquake they were about 4 percent of the Japan's 2010 GDP (Nanto and Cooper, 2011).

Given the disastrous consequences earthquakes can cause, as just exemplified in the previous paragraphs, it is urgent and critical to anticipate, plan for and reduce disaster risk in order to more effectively protect persons, communities and countries, their livelihoods, health, cultural heritage, socioeconomic assets and ecosystems, and thus strengthen their resilience, as stated in the Sendai Framework for Disaster Risk Reduction (UNDRR, 2015). In order to do so, one of the main steps is to assess the seismic risk.

[1] www.emdat.be

Table 1.1: Ten costliest earthquake/tsunami events during the period 2010-2019. Information obtained from the EM-DAT database[1].

Date	Country	Magnitude	Overall losses [US$ bn]	Insured losses [US$ bn]	Casualties
11/3/2011	Japan	9.0	210	37.5	19'846
27/2/2010	Chile	8.8	30	8	562
16/4/2016	Japan	7.0	20	5	49
20/5/2012	Italy	6.1	15.8	1.3	7
22/2/2011	New Zealand	6.3	15	12	181
12/1/2010	Haiti	7.0	8	0.2	222'570
20/4/2013	China	7.0	6.8	0.023	198
4/9/2010	New Zealand	7.1	6.5	5	0
19/9/2017	Mexico	7.1	6	2	369
25/4/2015	Nepal	7.8	5.2	0.1	8'831

What is seismic risk? Seismic risk denotes, in a wide sense, the earthquake induced social and/or economic expected losses at a site, or within an area, during a specific time. Seismic risk (R) is usually computed as a combination of three factors (UNDRO, 1980): Hazard (H), Vulnerability (V) and Exposure (E)

$$R = H \cdot V \cdot E$$

Seismic hazard is assessed quantitatively by means of the expected ground motion (or any associated phenomenon such as ground failure) at a specific site and within a specific time. In practice, such quantitative evaluation is made either by probabilistic (e.g., peak ground acceleration vs. return period) or by deterministic approaches (seismic scenarios for given events). Exposure is the quantification of the receptors (physical, social, economic, systemic, and functional) that may be influenced by a hazard, for example, number of people and their demographics, number and type of properties, etc. Vulnerability analysis refers to the fragilities of an exposed element (physical, social, economic, systemic, and functional) that can lead to disruption and harm when facing the stress provoked by a given hazard. Seismic hazard assessment is then essential in defining the entire chain, since it is the factor that both enters into risk assessments and that constraints the definition of parameters of physical vulnerability of the built environment, as the latter need to be established according to specific levels and features of the expected stress (Margottini and Menoni, 2018).

Figure 1.1 shows a Global Seismic Risk Map created by the Global Earthquake Model Foundation[2]. The main map presents the geographic distribution of average annual loss (USD) normalized by the average construction

[2] www.globalquakemodel.org/

costs of the respective country due to ground shaking. Some of the cities that present the highest seismic risk are Tokyo, Los Angeles, Istanbul, Beijing, Taipei, Santiago and Mexico City.

Tools for earthquake ground motion prediction (EGMP) are one of the key ingredients in seismic hazard assessment. A variety of procedures for EGMP has been proposed in the past four or five decades, relying, on one side, on different information detail on the seismic source and propagation path, and, on the other side, providing different levels of output, either in terms of peak values of ground motion or of an entire time history (Paolucci et al., 2014). Among them, empirical ground motion prediction equations (GMPEs), typically calibrated on the instrumental observations from real earthquakes, are the most commonly used. However, in spite of their overall effectiveness and ease of use, GMPEs suffer of intrinsic limitations: (1) the low availability of records in the range of major potential interest for engineering applications; (2) they refer to generic site conditions; (3) they only provide peak values of ground motion; (4) they are not suitable to be used for seismic scenario studies where the realistic representation of spatial variability of ground motion is an issue.

To overcome these limitations, three-dimensional physics-based numerical simulation (PBS) of earthquake ground motion has emerged as a powerful alternative tool to the use of GMPEs. Based on the rigorous numerical solution of the elastodynamics equation, simulations provide synthetic ground motion time histories reflecting the physics of the seismic wave propagation problem from the source up to the site of interest, including directivity effects in near fault conditions, topographic and complex site effects (Smerzini and Pitilakis, 2018). The *dream* behind PBS is that they may become the engine to produce, effectively and with reasonable computing efforts, plausible realizations of future earthquakes (Paolucci et al., 2014).

In the perspective of improving tools for seismic hazard identification, Munich RE funded a research activity with Politecnico di Milano, having the main objectives, on one side, of developing a certified computer code, SPEED (SPectral Elements in Elastodynamics with Discontinuous Galerkin), to run effectively numerical simulations of seismic wave propagation in large-scale models, and, on the other side, of applying this code to produce preliminary sets of physics-based earthquake ground shaking scenarios within large urban areas (Paolucci et al., 2014). The numerical code SPEED is extensively used in the development of this work.

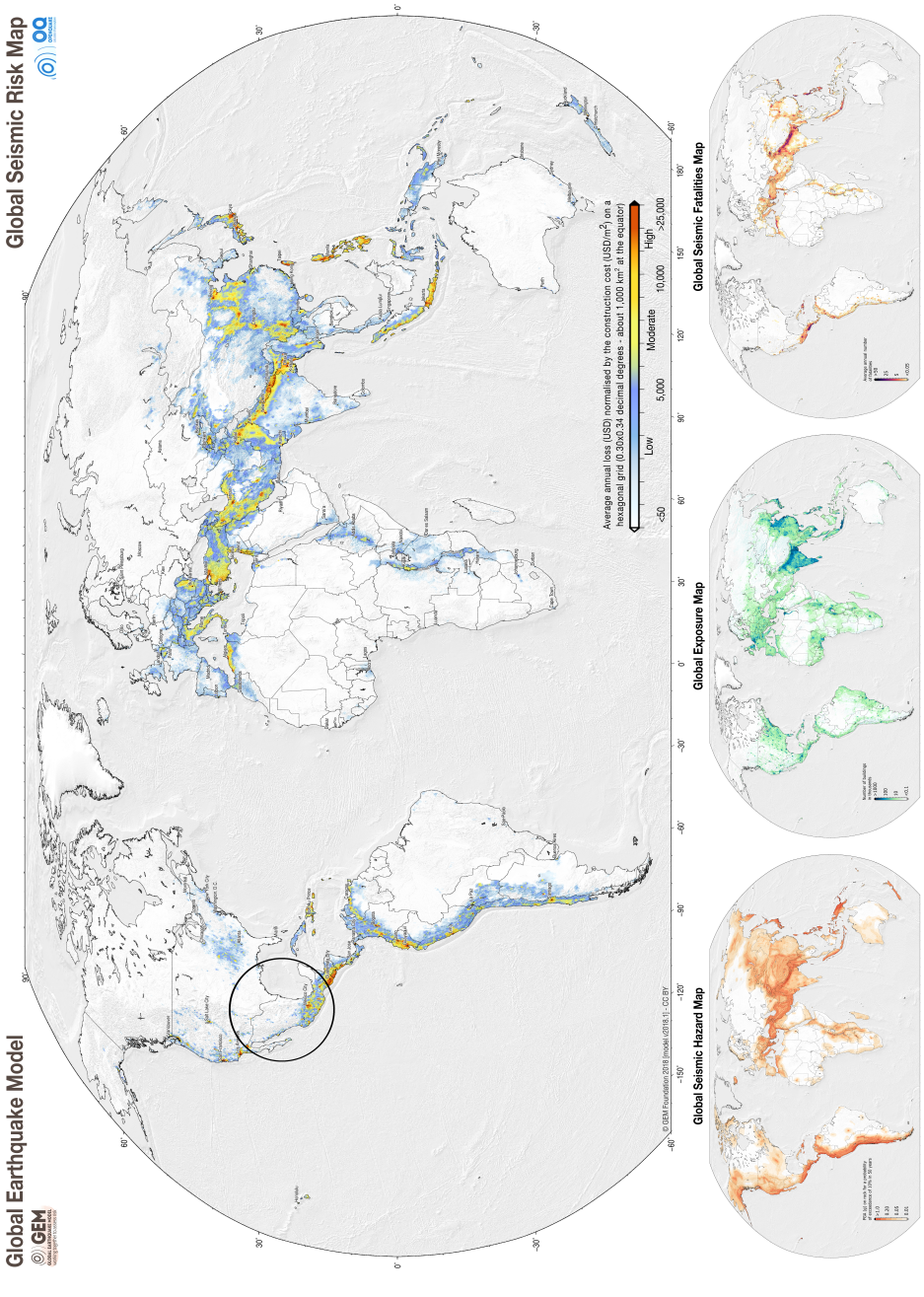

Figure 1.1: Global Seismic Risk Map. The main map presents the geographic distribution of average annual loss (USD) normalized by the average construction costs of the respective country. In the lower panel there are three maps: (i) a global seismic hazard map showing Peak Ground Acceleration (PGA) with a 10% probability of being exceeded in 50 years for rock conditions; (ii) a global exposure map depicting the distribution of residential, commercial and industrial buildings; and (iii) a map depicting an estimate of average annual human losses due to earthquake induced structural collapse of buildings. The black circle encloses the location of Mexico. [From Silva et al. (2018)].

1.2 The unusual case of Mexico City

Mexico City is the capital and largest city of Mexico. Its metropolitan area with 21'581'000 inhabitants is the fifth largest populated metropolitan area in the world (United Nations, 2018). It is located in the Valley of Mexico, on a volcanic plateau at about 2240 m above the sea level.

Mexico's capital is the oldest capital city in the Americas. The city was originally built on an island of Lake Texcoco by the Aztecs in 1325 as Tenochtitlan, which was almost completely destroyed in 1521 during the Spanish conquest. Lake Texcoco was drained starting from the 17th century, and nowadays the city rests on the lake bed's heavily saturated clay.

Figure 1.2: View of Mexico City. [Source: www.flickr.com/photos/eneas].

Located at the intersection of three large tectonic plates (North America, Rivera and Cocos plates), Mexico is one of the world's most seismically active regions. The seismicity and tectonics of southern and central Mexico are characterized by the subduction of the oceanic Cocos and Rivera plates beneath the North America Plate, along the Middle American Trench. In order to illustrate the high seismicity in Mexico, Figure 1.3 shows the epicenters of the earthquakes with magnitude M>6 that took place during the period 1950-2020.

Mexico has a long history of destructive earthquakes. The September 19, 1985 Michoacán earthquake has been the most deadliest and destructive in Mexico's history. The main shock, with a magnitude M_S8.1, was caused by the subduction of the Cocos plate beneath the continental plate of North America, in the zone known as the Michoacán gap, located about 360 km from

Mexico City. The first shock killed some 10'000 people in Mexico City, left about 50'000 homeless, and produced material losses of about 4 billion dollars, including the collapse of over 200 multistorey buildings (Esteva, 1988). The consequences of this event on the performance of urban infrastructure prompted a wealth of research on seismology, earthquake engineering, soil mechanics and structural dynamics.

Figure 1.3: Epicenters of the earthquakes with magnitude M>6 that took place in Mexico during the period 1950-2020. The epicenters of the earthquakes of September 19, 1985 and September 19, 2017 are highlighted. [Source: earthquake.usgs.gov].

The 1985 Michoacán earthquake was exceptional because despite peak ground accelerations in the epicentral area were low, still caused severe damage in Mexico City, 360 km away. Moreover, shaking duration inside the basin was exceptionally long, and there were enormous differences in intensities of shaking and associated building damage in different parts of the city. Source and path effects contributed to the severe long lasting ground motion. However, a number of experimental and theoretical results have established beyond a doubt that the determining factor of the 1985 catastrophe in Mexico City was a very large local amplification (e.g., Seed et al., 1988; Sanchez-Sesma et al., 1988; Chávez-García and Bard, 1994), i.e., site effects, caused by the presence at the surface of a very thin, extremely soft clay layer, and the underlying consolidated deposits. In fact, Singh et al. (1988a) quantified amplification factors as high as 50 at 0,5 Hz in the lake zone, relative to hard-rock zone motion.

Several authors (e.g., Sanchez-Sesma et al., 1988; Bard et al., 1988; Kawase and Aki, 1989) have concluded that the seismic response of the Mexico basin cannot be satisfactorily explained in terms of one-dimensional models, and the need for three-dimensional models has also been pointed out (e.g., Sánchez-Sesma et al., 1993; Mayoral et al., 2017).

Not only subduction earthquakes, as the Michoacán earthquake, are relevant for the seismic hazard of Mexico City, but also are intermediate-depth intraplate normal-faulting earthquakes. On September 19, 2017, two hours after the city had undergone a macroearthquake drill for the 32th anniversary of the M_S8.1 Michoacán earthquake, an Mw7.1 intraplate normal-faulting earthquake struck central Mexico, with epicenter at ∼120 km from Mexico City. This earthquake lead to 369 casualties, 228 of them in Mexico City. Furthermore, 5'765 dwellings were damaged and 52 buildings collapsed in Mexico City.

Local crustal earthquakes are also relevant for the seismic hazard of Mexico City. The Valley of Mexico has a complex geology and tectonics, there are numerous mapped faults within the valley which exceed 20 km in length (Singh et al., 2020). During the period 2010-2020, 12 earthquakes with magnitude Mw in the range 3.0-3.6 took place in the Valley of Mexico (SSN, 2020). Recently, Singh et al. (2020) estimated ground motions from an Mw5.0 scenario earthquake in the Valley of Mexico, using as empirical Green's functions recordings of an earthquake swarm activity that took place in Mexico City in 2019. Their results reveal that such an event may give rise to significant intensities in the lake-bed zone of Mexico City, and therefore a vigorous research effort is urgent to reevaluate seismic hazard posed by local, crustal earthquakes. Reliable estimation of ground motion from such earthquakes would require physics-based simulations.

The complicated seismotectonic environment of Mexico, results in the fact that Mexico City is exposed to a very high seismic hazard, which together with the large amplification of ground motion caused by lake bed's extremely soft clay and the underlying consolidated deposits, makes the study of the seismic response of the Mexico City basin a very relevant topic.

1.3 Aim and Objectives

As briefly introduced in the previous section, the wave propagation phenomenon in the Mexico City basin is quite unusual because of the large amplification of seismic waves and duration of ground motion. For these

reasons, the aim of this work is to investigate whether or not it is possible to generate realistic synthetics in the low-frequency range for the Mexico City basin, using 3D physics-based numerical simulations with a seismic point source representing a local crustal earthquake.

In order to achieve this aim, some important objectives are followed:

- To examine the most relevant characteristics of the ground motion in Mexico City induced by the September 19, 1985 and September 19, 2017 earthquakes.
- To review the research carried out after the September 19, 1985 earthquake aiming to explain the large site effects in the lake zone of Mexico City.
- To collect the relevant information regarding the geotechnical characterization of the Mexico City's subsoil.
- To construct a 3D numerical model for Mexico City considering the main features of the basin's lacustrine sediments.
- As a validation case study, to simulate the wave propagation in the Mexico City basin due to a point source representing a Mw3.0 earthquake which occurred in Mexico City on July 17, 2019, using the high-performance spectral element code SPEED.
- To compare the results of the 3D PBS with the recordings of the reference earthquake, to validate the 3D model, for possible use for simulation of ground motions during larger magnitude earthquakes.
- To discuss the main wave propagation phenomena taking place within the lake zone of Mexico City.

1.4 Thesis organization

The thesis is organized as follows. The first part of chapter 2 provides an overview of the seismotectonic environment in Mexico which is important to understand why Mexico City is threatened by such different types of earthquakes, i.e., subduction earthquakes, intraplate earthquakes and crustal earthquakes. Then, a short description of the most relevant historical earthquakes in Mexico is given. Mexico City's subsoil amplifies ground motion because of its mechanical and geometrical characteristics, hence they are described in section 2.4. Finally, the earthquakes of September 19, 1985 and

September 19, 2017 are presented and their main ground motion characteristics are analyzed. A literature review of some of the research works carried out after the Michoacán earthquake with the aim of explaining the causes of the severe long lasting ground motion in Mexico City is also presented.

Chapter 3 starts discussing the main characteristics, drawbacks and strong points of 3D physics-based numerical simulations. Then, the spectral element code SPEED, designed for the simulation of large-scale PBS, is presented. Finally, the process followed for the construction of the 3D numerical model for the Mexico City area, and the simulated case are described.

In Chapter 4 the results from the numerical simulations are presented and compared with the recordings from the earthquake. The agreement of the numerical results with the most relevant features of the observed ground motion is analyzed.

Chapter 5 discusses the findings of the research in line with the aims and objectives that guided the entire study. This chapter also draws conclusions on the major findings of the study and suggests some of the future work that could be done related to this thesis.

Chapter 2

Seismicity in Mexico and Site Effects in Mexico City

2.1 Seismotectonic environment in Mexico

The seismicity and tectonics of southern and central Mexico are characterized by the subduction of the oceanic Cocos and Rivera plates beneath the North America Plate, along the Middle American Trench (Figure 2.1). Subduction zones are prone to large earthquakes, for the two plates grinding against each other, sometimes sticking together ("locking"), the lower plate pulling the upper plate down with it and thus building up stress. When the stress builds to the breaking point, the upper plate breaks free and springs back to where it had been, thus lifting the ocean floor (Tectonics Observatory at Caltech, 2009), as schematically shown in Figure 2.2. The Cocos plate moves at about 8 cm/year (DeMets et al., 2010), thus it takes hundreds of years for stress to build up before causing a large earthquake.

The Mexican subduction zone lacks the typical "Wanati-Benioff Zone" of seismicity, which helps delineate the subducting slab in most subduction zones around the world. However, the geometry of the Cocos and Rivera Plates, are well known from seismicity, moment tensors, regional and global tomography, and receiver function studies (Ferrari et al., 2012; Pardo and Suarez, 1995; Pérez-Campos et al., 2008; Yang et al., 2009). The classic paper by Pardo and Suarez (1995), based on relocation of teleseismic events, first defined the geometry of the subducted slabs but was unable to determine the position of the slab beneath the TMVB because this region is almost devoid of earthquakes (Ferrari et al., 2012).

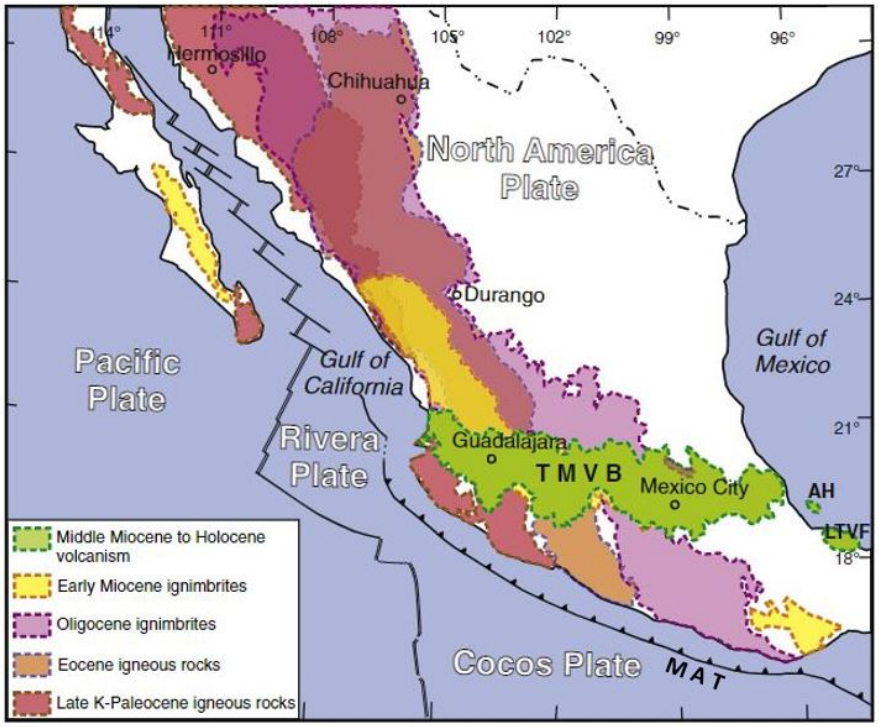

Figure 2.1: Geodynamic setting and main continental magmatic provinces of Mexico. MAT: Middle American Trench; TMVB: Trans-Mexican Volcanic Belt. [Adapted from Ferrari et al. (2012)].

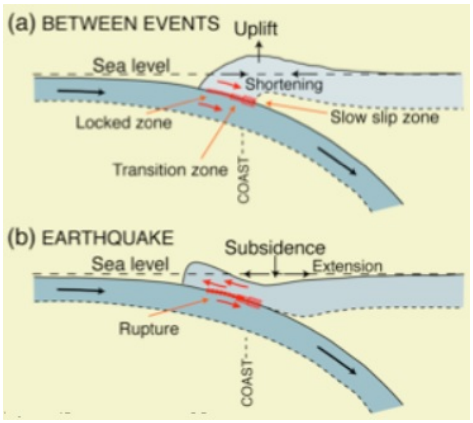

Figure 2.2: Cross section through a subduction zone before an earthquake (above) and during an earthquake (below). [From Hyndman and Wang (1995)].

During the Meso-American Subduction Experiment (MASE), a 100-station broadband array was deployed during 2005–2007 across central Mexico, from Acapulco on the Pacific coast to Tempoal, near the Gulf of Mexico in the north, passing through Mexico City. Pérez-Campos et al. (2008) used converted teleseismic waves recorded by the MASE array to determine the struc-

tural interfaces using the receiver function (RF) method. In order to complement the result from the RFs, a tomographic image of the P-wave velocity deviations from a layer model was obtained from relative travel time variations determined from the teleseismic events. The tomography method is a complementary technique to RFs since it is sensitive to dipping structures but not very sensitive to the horizontal ones. The results from the MASE experiment shown in Figure 2.3, show that the slab dips at 15° until 80 km from the coast and then flattens at 50 km depth and extends inland for 200 km, until it dives into the mantle with a dip of 75° up to a depth of 500 km. The change from flat slab to steep dip happens over a short length scale (∼50 km).

Flat slab subduction underneath central Mexico produces, in addition to low-angle thrust events at the plate contact, a wide diversity of earthquakes (Melgar et al., 2018). Downdip of the megathrust, prior to the transition to flat-slab subduction,Pacheco and Singh (2010) identified from regional moment tensor analysis a complex pattern of both normal and thrust events. In the flat slab segment, Pacheco and Singh (2010) identified only a few small magnitude earthquakes. In the transition region from flat slab to steep dip, damaging intraplate normal faulting events, like the 2017 Puebla-Morelos Mw7.1 (Melgar et al., 2018) and the 1999 Mw7.0 Tehuacán earthquakes (Singh et al., 1999), have happened before.

Subduction zones often have a chain of volcanoes, called volcanic arc. A volcanic arc is produced when the oceanic crust of the subducting plate attains high enough temperature and pressure to undergo metamorphism, releasing water which triggers melting of the mantle. The resulting magma then rises to the surface, spewing out as lava, and forming volcanoes (Tectonics Observatory at Caltech, 2009). In the case of Mexico, this volcanic arc is known as the Trans-Mexican Volcanic Belt (TMVB), that is the largest Neogene volcanic arc in North America, encompassing 160,000 km^2 and a length of almost 1000 km between 18°30 and 21°30N in central Mexico. The TMVB is built upon Cretaceous and Cenozoic magmatic provinces (Figure 2.1) and a heterogeneous basement made of tectonostratigraphic terranes of different age and lithology (Ferrari et al., 2012). The distribution of the volcanic arc is oblique (∼16°) relative to the Middle American Trench, in an unusal geometry which is not parallel to the subduction zone. Pardo and Suarez (1995) showed that this unusal geometry is due to the geometry and to the lateral changes in dip of the subducted Cocos plate beneath central Mexico.

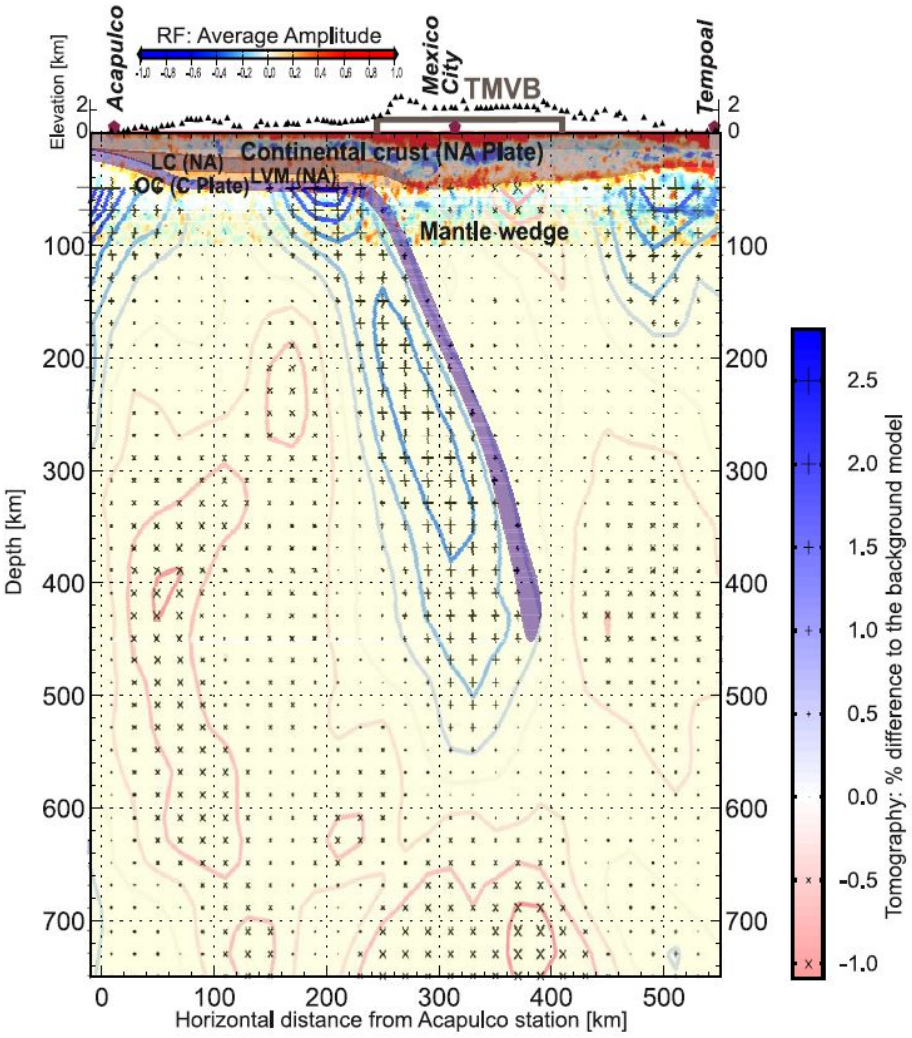

Figure 2.3: Composite model: tomographic and RF image showing the flat and descending segments of the slab (purple line). The key features are the flat under-plated subduction for 250 km, and the location and truncation of the slab at 500 km. The zone separating the ocean crust from the continental Moho is estimated to be less than 10 km in thickness. NA = North America, C = Cocos, LC = lower crust, LVM = low velocity mantle, OC = oceanic crust. The contour lines indicate wave speed. [From Pérez-Campos et al. (2008)].

The TMVB is traversed by networks of faults both parallel as well as orthogonal to its axis (Pasquaré et al., 1987). In the central part of the TMVB (CTMVB), between 99°W and 102°W, Suter et al. (2001) reported about one hundred EW striking, normal faults greater than 2 km in length. The largest of these are the Venta de Bravo fault (45 km) and the Acambay-Tixmadejé fault (34 km). This zone is characterized by shallow intraplate earthquakes. The Acambay-Tixmadejé fault ruptured in at least four Holocene earthquakes with a mean slip of 60 cm per event, a recurrence interval of 3600 yr, and

a slip rate of 0.17 mm/y (Langridge et al., 2000). Last rupture was in 1912 during the Acambay Ms7.0 earthquake, which caused severe damage in the epicentral area, but minor damage in Mexico City, located about 100 km from the epicenter (Urbina and Camacho, 1913).

2.2 Seismicity in the Mexico basin

The Mexico basin is located within the CTMVB, and is 100 km long and 80 km wide. It is bounded by NNW-SSE aligned Sierra de las Cruces volcanic range to the west, the N-S aligned Sierra Nevada volcanic range to the east that includes Popocatépetl, Iztaccíhuatl, Telapón, and Tláloc stratovolcanoes, the E-W Sierra Chichinautzin to the south, and the Apan-Tezontepec volcanic field to the north (Arce et al., 2019). The Mexico Basin has a complex geology and tectonics, as shown in Figure 2.4, that has been extensively studied (Mooser, 1975; Vazquez-Sanchez and Jaimes-Palomera, 1989; Mooser, 1996; Santoyo-Villa et al., 2005), so it is not surprising that earthquakes of small magnitudes occur in the area (SSN, 2019).

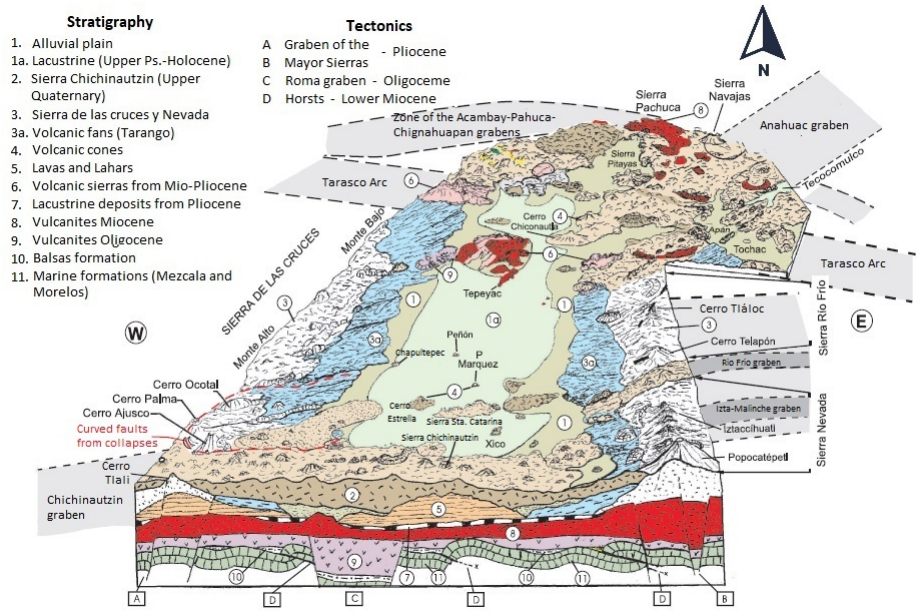

Figure 2.4: Geology and Tectonics of the Mexico Basin. [Modified from Santoyo-Villa et al. (2005)].

Seismicity in the CTMVB, near Mexico City is low. Due to sparse seismic network and complex crustal structure of the region, the earthquake locations are not sufficiently precise to map active faults, depths of the events are not well constrained, and reliable focal mechanisms are available only for a handful of earthquakes. Scarcity of data also limits the capability to estimate ground motion from future CTMVB earthquakes (Singh et al., 2020). For these reasons, the seismic hazard from earthquakes in the CTMVB suffers from large uncertainty (Bayona-Viveros et al., 2017).

Regarding the origin of earthquakes in the region, it is thought that they are generated by the reactivation of old faults (Figure 2.5). It is also considered that these events may occur as a result of the accumulation of regional stresses or that the subsidence of the Valley of Mexico could originate stresses that, although not properly generate earthquakes, could trigger them (Havskov, 1982). There is also the hypothesis that large earthquakes generated on the coast can give rise to unbalanced conditions and trigger local earthquakes (Singh et al., 1998).

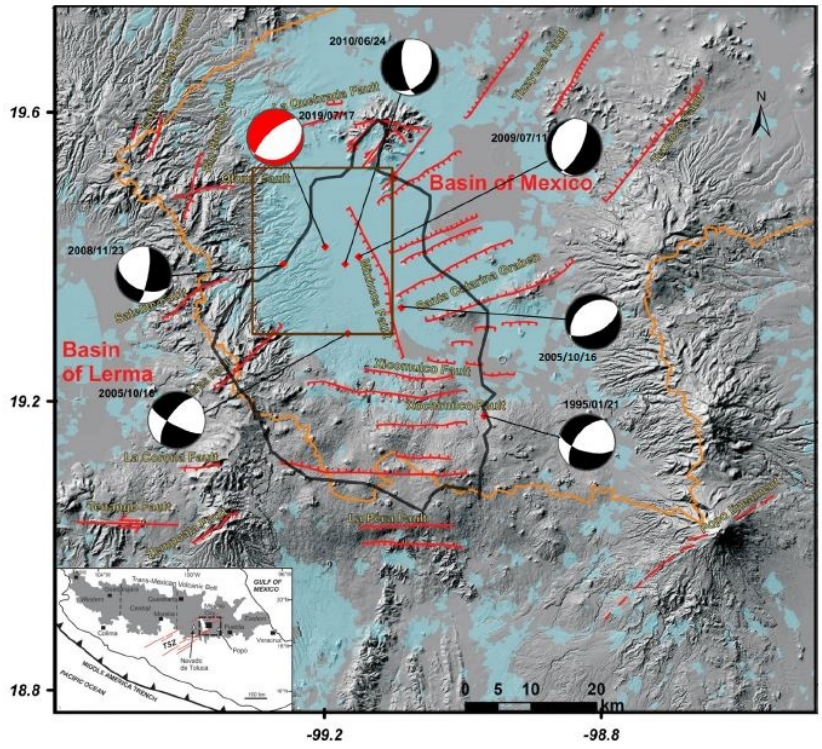

Figure 2.5: Digital elevation model (DEM) of the Mexico Basin area showing faults and focal mechanisms of earthquakes in the region. Black thick contour encloses Mexico City. [From Singh et al. (2020)].

In Table 2.1 are presented the earthquakes reported by the Mexican National Seismological Service (SSN) with epicenter in Mexico City and magnitude M≥3, during the period 2010 - 2020. The locations and focal mechanisms of the 06/24/2010 and 07/17/2019 earthquakes are shown in Figure 2.5. The later event will be discussed in the following chapter.

Table 2.1: Earthquakes reported by the Mexican National Seismological Service with epicenter in Mexico City and magnitude M≥3, during the period 2010 - 2020 (SSN, 2020).

Date	Magnitude	Latitude	Longitude	Depth [km]
06/24/2010	3.1	19.380°	-99.150°	14
07/05/2010	3.2	19.200°	-98.950°	5
10/21/2012	3.5	19.115°	-99.252°	5
12/1/2014	3.4	19.353°	-99.216°	2
2/13/2018	3.3	19.461°	-99.072°	2
3/24/2018	3.3	19.190°	-98.948°	1
5/8/2018	3.6	19.163°	-98.944°	3
7/17/2019	3.0	19.408°	-99.205°	1.1
9/23/2019	3.1	19.172°	-98.947°	12
9/23/2019	3.1	19.176°	-98.947°	12.4
12/22/2019	3.5	19.091°	-99.209°	4.1
1/4/2020	3.4	19.172°	-98.969°	2.4

2.3 Significant historical earthquakes in Mexico

As it has been previously discussed, Mexico City is affected by four types of earthquakes, which are explicitly contemplated by the Building code of Mexico City (Rosenblueth et al., 1989):

- Local earthquakes
- Continental plate earthquakes
- Intermediate-depth intraplate earthquakes
- Subduction earthquakes

However, subduction and intermediate-depth intraplate earthquakes are the most important for seismic hazard in Mexico City.

The September 19, 1985 Michoacán earthquake has been the most deadliest and destructive in Mexico's history. There were two main shocks with a difference of about 36 hours; their magnitudes were 8.1 and 7.6, respectively. They were caused by the subduction of the Cocos plate beneath the continental plate of North America, in the zone known as the Michoacán gap,

located about 360 km from Mexico City. The first shock killed some 10'000 people, left about 50'000 homeless, and produced material losses of about 4 billion dollars, including the collapse of over 200 multistorey buildings (Esteva, 1988). Most of the damages occurred in the soft soil area of Mexico City.

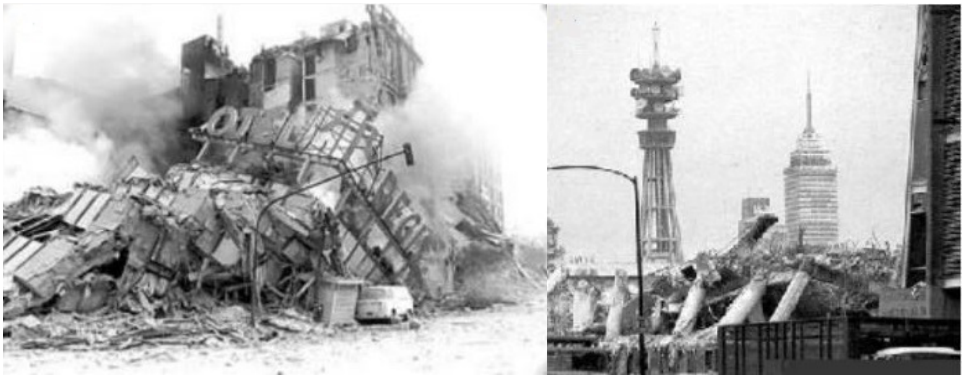

(a) (b)

Figure 2.6: Collapsed buildings in Mexico City after the September 19, 1985 earthquake. a) Hotel Regis [Source:La Jornada], b) Administrative building [Source:Munich-Re].

However, this wasn't the largest earthquake during the previous century. The largest earthquake during the 20th century took place on June 3, 1932 in the coast of Jalisco and Colima. It broke the shallow part of the Rivera subduction zone, had a magnitude of 8.2 in the Richter scale and a rupture length of about 220 km (Singh et al., 1985a). Even tough this earthquake was stronger than the Michoacan earthquake, there were no casualties in Mexico City, and just some small houses collapsed. The reason for this was its large distance to Mexico City, of more than 500 km.

Another important earthquake took place in Chiapas, in the southern part of Mexico, on September 8, 2017. It had a moment magnitude of Mw8.2, and rather than being a plate boundary thrust event, its faulting mechanism and depth indicate an intraslab normal fault rupture (Ye et al., 2017). This event is the largest intraslab earthquake documented along the Mexican subduction zone. Shaking from the earthquake was devastating in southern Mexico, with at least 102 fatalities, mostly in Oaxaca, and 41,000 homes damaged. Peak tsunami waves of 1 to 1.75 m amplitude were recorded at Salina Cruz and in Chiapas.

A list of earthquakes with magnitude M≥7.5 reported by the SSN is reported in Table 2.2. The location of the most important events is shown in Figure 2.7.

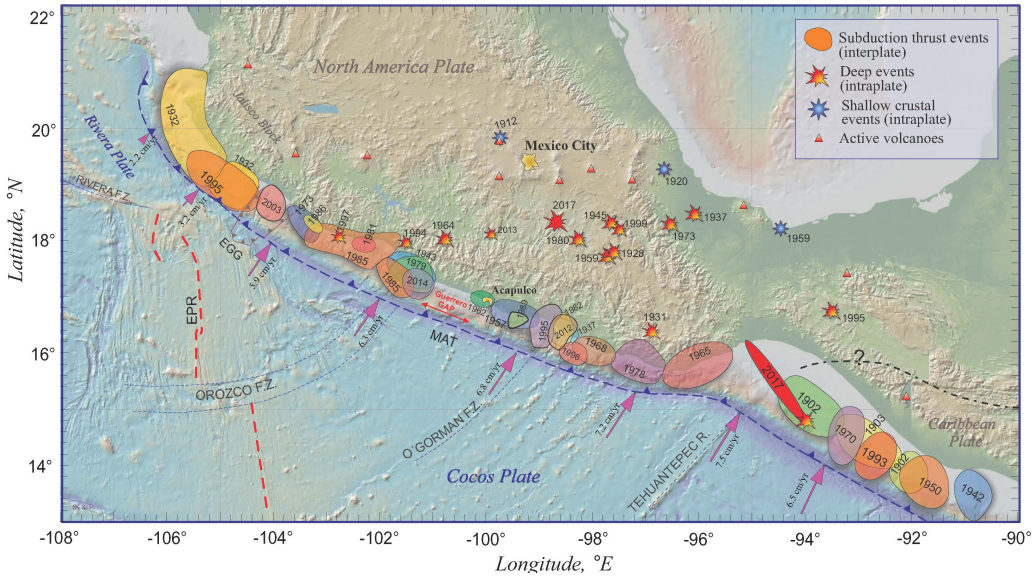

Figure 2.7: Location of the most important earthquakes in Mexico since 1900. [From Servicio Sismológico Nacional (2017)].

As mentioned earlier, intermediate-depth intraplate normal-faulting earthquakes are also paramount for seismic hazard of Mexico City. Some important earthquakes of this type include the 1931 M7.8 earthquake that had catastrophic consequences in Oaxaca (Singh et al., 1985b), the 1980 M7.1 earthquake which devastated Huajuapan de León in Oaxaca (Yamamoto et al., 1984), and the Tehuacán M7.0 earthquake of 1999 which resulted in many damaged adobe dwellings in the region close to the epicenter and damaged colonial structures in the city of Puebla (Singh et al., 1999). More recently, on September 19, 2017, two hours after the city had undergone a macroearthquake drill for the 32th anniversary of the M_S8.1 Michoacán earthquake, an Mw7.1 earthquake struck central Mexico.

The 19 September 2017 Mw7.1 Puebla-Morelos earthquake in central Mexico was the most damaging event for this densely urbanized area, where more than 28 million people live, since the 1985 M_s8.1 Michoacán earthquake. It lead to 369 casualties, as reported by Civil Protection, 228 of them in Mexico City. Furthermore, 5'765 dwellings were damaged and 52 buildings collapsed in Mexico City. Overall losses amounted to US$ 6bn, of which US$ 2bn were insured (Munich Re, 2018).

Table 2.2: Subduction earthquakes with magnitude M≥7.5, reported by the SSN since 1900 (SSN, 2020).

Date	Magnitude	Latitude	Longitude	Depth [km]
9/23/1902	7.7	16.50°	-92.50°	25
1/14/1903	7.6	15.00°	-93.00°	33
4/15/1907	7.6	16.70°	-99.20°	33
6/7/1911	7.6	17.50°	-102.50°	33
12/16/1911	7.5	16.90°	-100.70°	50
3/22/1928	7.5	15.67°	-96.10°	33
6/17/1928	7.6	16.33°	-96.70°	33
10/9/1928	7.5	16.30°	-97.30°	33
6/3/1932	8.2	19.57°	-104.42°	33
6/18/1932	7.8	19.50°	-103.50°	33
4/15/1941	7.6	18.85°	-102.94°	33
8/6/1942	7.9	14.80°	-91.30°	50
7/28/1957	7.8	17.11°	-99.10°	33
1/30/1973	7.6	18.41°	-103.02°	24
2/4/1976	7.5	15.26°	-89.20°	13
11/29/1978	7.6	16.01°	-96.59°	23
9/19/1985	8.1	18.42°	-102.47°	15
9/21/1985	7.6	17.83°	-101.68°	17
10/9/1995	8	18.99°	-104.25°	25
1/22/2003	7.6	18.60°	-104.22°	9
3/20/2012	7.5	16.26°	-98.46°	18
9/8/2017*	8.2	14.76°	-94.10°	46
*Intraslab normal-faulting event				

(a) (b)

Figure 2.8: Collapsed buildings in Mexico City after the September 19, 2017 earthquake. a) Building at Medellin 176 b) Building at Simon Bolívar 190. [Source:ProtoplasmaKid/WikimediaCommons /CC-BY-SA4.0].

The most important intermediate-depth intraplate earthquakes reported by the SSN are reported in Table 2.3. The location of some of them is shown in Figure 2.7.

Table 2.3: Most important intermediate and deep earthquakes, with inland epicenters, reported by the SSN (SSN, 2020).

Date	Magnitude	Latitude	Longitude	Depth [km]
2/10/1928	6.5	18.26°	-97.99°	84
1/15/1931	7.8	16.34°	-96.87°	40
7/26/1937	7.3	18.45°	-96.08°	85
10/11/1945	6.5	18.32°	-97.65°	95
1/6/1948	7	17.00°	-98.00°	80
5/24/1959	6.8	17.72°	-97.15°	80
7/6/1964	7.2	18.03°	-100.77°	55
8/28/1973	7.3	18.25°	-96.55°	82
6/7/1976	6.5	17.41°	-100.68°	57
10/24/1980	7.1	18.17°	-98.22°	65
12/10/1994	6.6	17.98°	-101.52°	53
10/21/1995	7.1	16.81°	-93.74°	160
1/11/1997	7.1	18.34°	-102.58°	40
6/15/1999	7	18.13°	-97.54°	63
12/11/2011	6.5	17.84°	-99.96°	54
16/06/2013	5.8	18.11°	-99.23°	55
9/19/2017	7.1	18.33°	-98.67°	51

The details of the 1985 M_s8.1 Michoacán earthquake and the 2017 M_w7.1 Puebla-Morelos earthquake will be tackled in the following sections.

2.4 Geotechnical characterization of Mexico City's subsoil

Mexico City is located on a volcanic plateau at about 2240 m above the sea level, surrounded by volcanic sierras, alluvial fans and plains. Much of the knowledge about the geological stratigraphy and deep structural features of Mexico Basin shown in Figure 2.9, has been obtained from deep boreholes drilled by Petroleos Mexicanos (PEMEX) after the 1985 earthquake (some of which are shown in Figure 2.9, namely P.Roma, P.Mixhuca and P.Texcoco) and some geophysical studies (e.g. Pérez-Cruz, 1988).

As described by Sanchez-Sesma et al. (1988), before the Pleistocene the Valley of Mexico drained to the South, to contribute to the Amacuzac river.

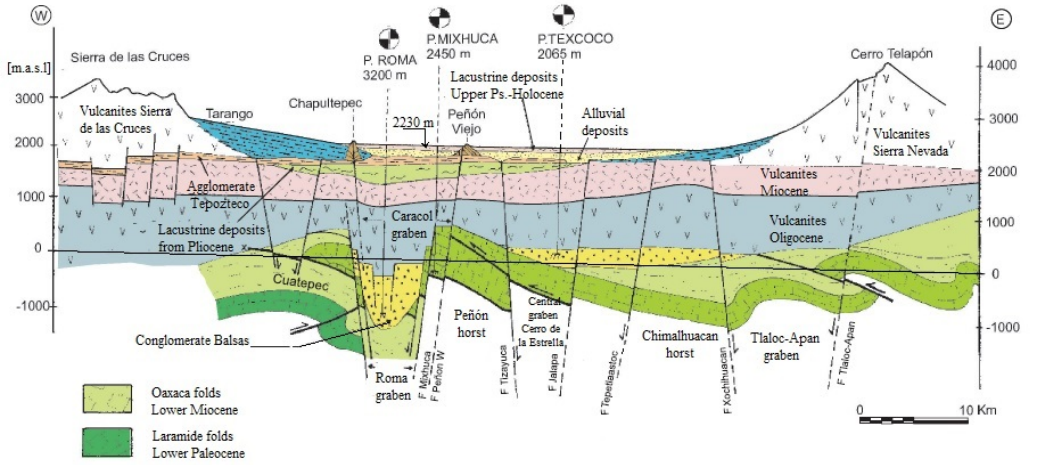

Figure 2.9: E-W Geological section crossing Mexico City [Adapted fromSantoyo-Villa et al. (2005)].

By the end of the Pliocene important fractures were predominantly EW and gave rise to basaltic effusions of the Chichinautzin mountain range, which transformed the valley into a closed basin during the Quaternary (Santoyo-Villa et al., 2005).

Afterwards, the bottom of the basin was silted up with a stratification of different type of materials, like proluvials (silts and sands), lacustrine materials (clays and silts), and volcanic sand and ash that upon weathering generated highly compressible clays (Auvinet et al., 2017). Therefore, Mexico basin presents two main geological units overlying the pre-Chichinautzin basement, i.e. a thick consolidated unit, the so-called "deep deposits", overlaid by a thin clay layer with very weak mechanical characteristics.

In 1519, when the Spanish arrived to the capital of the Aztec Empire, Tenochtitlán (nowadays Mexico City), there were five lakes within the basin, as depicted in Figure 2.10. After a series of floodings, the Spanish realized that the lakes needed to be drained. In 1607 Enrico Martinez designed a channel and tunnel at Nochistongo to deviate the course of Cuauhtitlán River to the north. This endeavor continued during the independent era, with the construction of the *Gran Canal de Desagüe* (main drainage channel) at the end of the 19th century, and the construction of a costly system of deep drainage tunnels from 1967 to 1975. The more the lakes were drained, the more the city extended on the former lake bed.

Figure 2.10: The Mexico basin lakes as the Spanish found them in 1519. Nowadays there is only one small lake near Xochimilco. [Adapted from DDF (1975)].

2.4.1 Stratigraphy and geotechnical zonification

A typical section of the stratigraphic sequence of Mexico City is presented in Figure 2.11. The clay deposits are usually inter-bedded with lenses of sandy silts and silty sands. Below the clay layer, the deep deposits are found. In the western and central part of the city, within the clay deposits, a thin layer of a very dense sandy silt is present (shown in red). It can reach up to 4 m thickness and is known as the "capa dura". Pile foundations resting on this layer have been used in many tall buildings. Below the capa dura, the clay is stiffer and is commonly know as the inferior clay formation (Marsal and Mazari, 1959). In the figure it is also possible to appreciate that at the top, there is a thin layer made of archaeological debris and artificial fills with shear wave velocity of about 200 m/s (Suarez et al., 1987), which is thicker ($\sim$12 m) in the Historical Center.

Recently, using geostatistical techniques, Juárez-Camarena et al. (2016) modeled the lower boundary of the clay deposits, i.e., the contact with the deep deposits (Figure 2.12). They made use of a Geographic Information System for Geotechnical Borings (GIS-GB) that includes more than 10'000 soil profiles collected during the last decades.

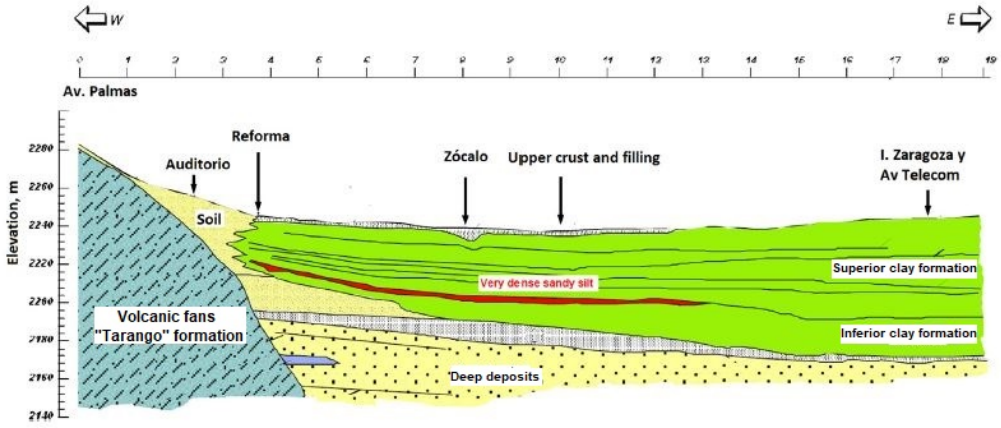

Figure 2.11: A typical section of the stratigraphic sequence of Mexico City. [Adapted from Santoyo-Villa et al. (2005)].

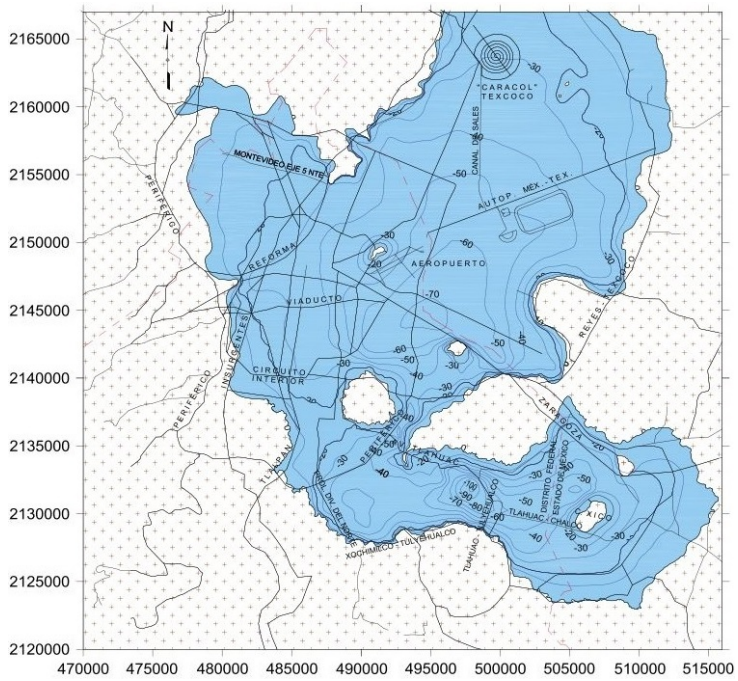

Figure 2.12: Contour map of the contact between clay and deep deposits. [From Juárez-Camarena et al. (2016)].

The properties of the clay deposits are well known from numerous borings and laboratory tests. For instance, there is extensive information about index and static mechanical properties of Mexico City clays in Marsal and Mazari (1959). Studies about its elasto-plastic constitutive modelling (e.g. Diaz-Rodriguez et al., 1992), and time dependent behavior (e.g. Diaz-Rodriguez and Santamarina, 2001) are also available. Mexico City clays present notori-

ously high Atterberg limits and natural water contents, that in some parts of the city can reach values as high as 600%. These materials have been pointed out as extremely plastic clays which, correspondingly, display very low shear strengths and rather large compressibilities (Ovando-Shelley, 2011).

On the other hand, the available information on the deep deposits is scarce. From the previously mentioned PEMEX study, it was found for the boreholes Roma-1, Mixhuca-1 and Tulyehualco-1 that the deep deposits reached depths of approximately 65 m, 200 m and 490 m, respectively (Pérez-Cruz, 1988). Marsal and Graue (1969) presented the results of some seismic refraction tests carried out in the former Texcoco lakes, in which the contact of the deep deposits with the pre-Chichinautzin basement was found at depths between 250-500 m. They also measured a V_P of 1550-1700 m/s for these materials. From some of the tests presented by (Jaime, 1987) (Figure 2.16), that will be explained later, V_S in the first meters of the deep deposits was found to be between 300-600 m/s. Based on the available information at the time, Suarez et al. (1987) created a contours map of the pre-Chichinautzin topography, which was taken as the reference for many of the 2D wave propagation analyses carried out after the 1985 Michoacán earthquake.

Recently, Cruz-Atienza et al. (2016) generated the pre-Chichinautzin topography shown in Figure 2.13 from a large data set of natural vibration periods, T_0, across the basin, considering that the depth to consistent deposits is $H = T_0(V_{S\,eq}/4)$, and assuming an average V_S of 400 m/s for the deep deposits.

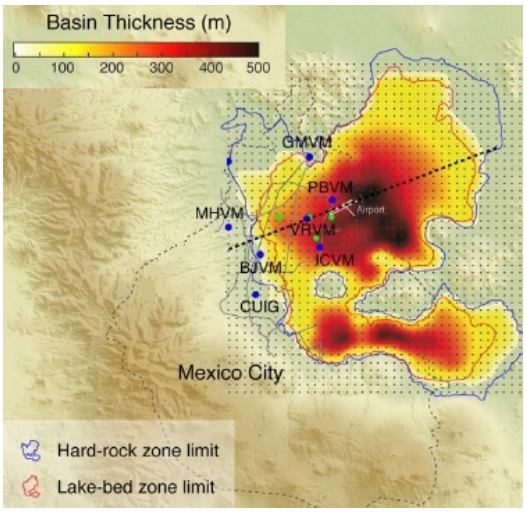

Figure 2.13: Depth contours of the estimated pre-Chichinautzin basin topography. [Adapted from Cruz-Atienza et al. (2016)].

On the basis of geotechnical characteristics, Marsal and Mazari (1959) proposed to divide the city into three main zones: Lake zone, Transition zone and Hill zone. This proposal was adopted in the Mexico City Building Code of 1976, and after some modifications, it is still considered in the latest 2017 version (GCDMX, 2017). The Building Code defines the three geotechnical zones (Figure 2.14) as follows

- Zone I. Hills, formed by rocks or hard soils that were generally deposited outside the lake are, but where sandy deposits in relatively loose state or soft clays can also be found.
- Zone II. Transition, where deep firm deposits are found at a depth of 20 m or less, and consisting predominantly of sand and silt layers interbedded with lacustrine clay layers.
- Zone III. Lake, composed of potent deposits of highly compressible clay strata separated by sand layers with varying content of silt or clay.

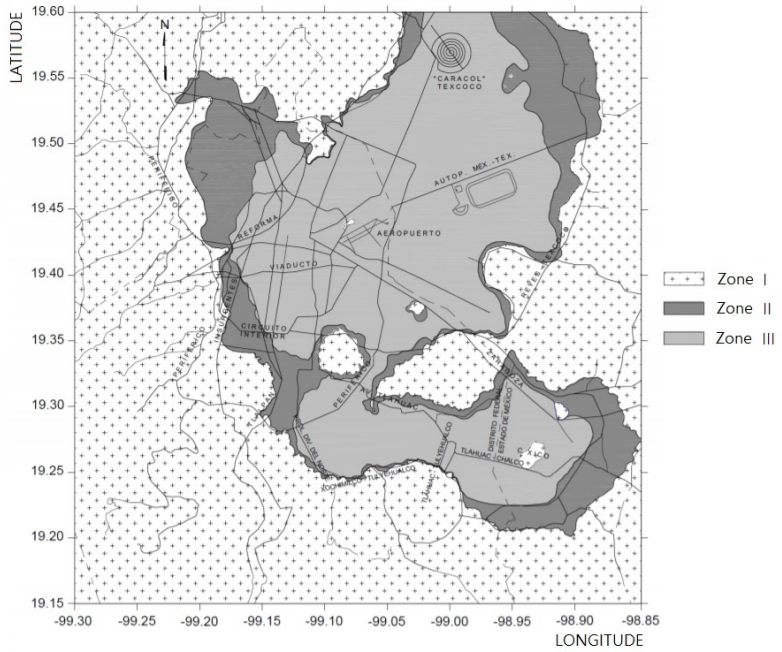

Figure 2.14: Geotechnical zoning map for Mexico City according to the building code. Zone I=Hills, Zone II=Transition, Zone III=Lake bed. [Adapted from GCDMX (2017)].

2.4.2 Dynamic properties

The study of the ciclic and dynamic properties of Mexico City clays attracted the attention of the engineering community even before the 1985 Mi-

choacán earthquake (e.g. Zeevaert, 1967; León et al., 1974; Faccioli, 1976b). Evidently, posterior to the earthquake, a thorough study of dynamic properties was carried out (e.g. Jaime, 1987; Romo et al., 1988; Diaz-Rodriguez, 1989; Romo and Ovando-Shelley, 1996). One the main characteristic of the Mexico City clays, is that due to its high plasticity index, they exhibit no significant reduction in shear modulus even for shear strains as high as 0,1%. Similarly, there is no significant increase in the damping ratio until angular distortions of the order of 0,3% (after Romo et al., 1988). This characteristic is exemplified in Figure 2.15, where results reported by Mayoral et al. (2016) from resonant column and cyclic triaxial tests carried on samples retrieved from the former Texcoco lake are presented. Based on this property of Mexico City clays, most wave propagation analyses consider visco-elastic constitutive models.

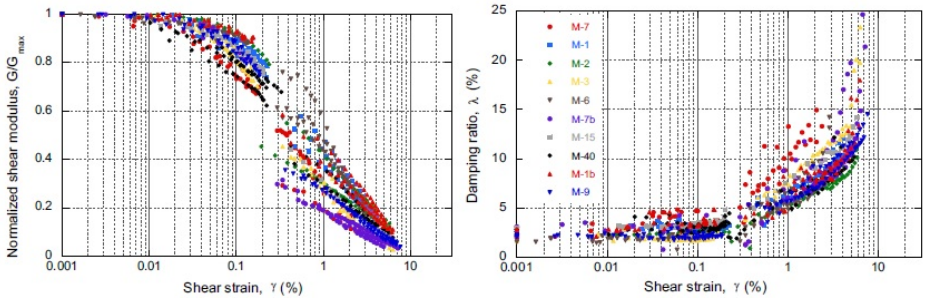

Figure 2.15: Experimental shear modulus degradation and damping curves of samples retrieved from the former Texcoco Lake zone. [From Mayoral et al. (2016)].

Mexico City clays are also characterized by very low shear wave velocities. Figure 2.16 shows profiles of shear wave velocity (V_S) for different sites in the lake zone, obtained from direct measurements in boreholes using down-hole and P-S suspension logging techniques (Jaime, 1987). The locations of the boreholes are shown over the map of the seismic zonification of Mexico City, which is quite similar to the geotechnical zonification, the main difference being that the zone III is further subdivided into zones IIIa, IIIb, IIIc and IIId, to account for the increasing depth of the clay deposits when moving from the hill zones to the center of the old lakes. Analysis of these results shows that: (1) V_S in the clay layer is lower than 100 m/s and shows an approximately linear increase with depth; (2) the location of the deep deposits is evident in various of the profiles, where V_S >300 m/s; (3) in borehole TLB, even at a depth of 75 m, the deep deposits are not reached, the reason for this is that it is located within the seismic zone IIId, where the thickness of the clay deposits is the highest.

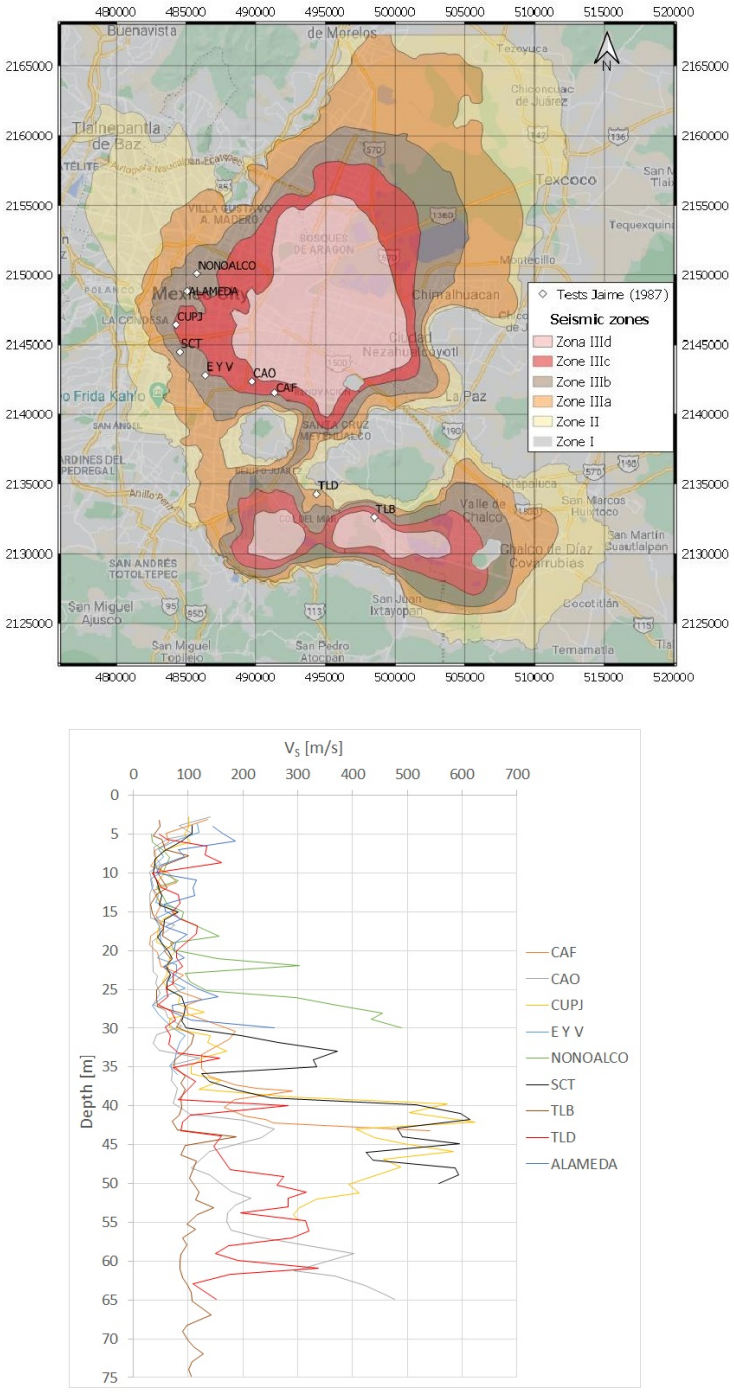

Figure 2.16: V_S profiles (below) obtained from down-hole and P-S suspension logging tests located at different sites in the lake zone (above) as reported by Jaime (1987).

2.4.3 Subsidence

The demographic development in Mexico City has created an accelerated demand of services, mostly of potable water. One of the cheapest ways to meet this demand has been the exploitation of the local aquifer by pumping water from deep wells. This has produced a water pressure drawdown in the subsoil that in turn is causing general subsidence of the former lacustrine area and soil fracturing (Auvinet et al., 2013). This problem was first identified by Roberto Gayol in 1925, and then explained by Nabor Carrillo in 1947, who pointed out as the major cause the consolidation of the clay deposits induced by increases of the effective stresses caused by a decrease of the pore water pressure due to the pumping. Subsidence has caused differential settlements and affected colonial buildings, modern structures, installations as the subway system, the Gran Canal, and the water system network.

The subsidence evolution in three sites of the Historic Center of Mexico City is presented in Figure 2.17. It is observed that the subsidence rate reached a 29 cm/year peak during 1947-1957, and is still of the order 10 cm/year for these three sites (Auvinet et al., 2013). However, in the eastern part of the basin, subsidence rates of about 30 cm/year were measured during the period 2007–2011 (Chaussard et al., 2014).

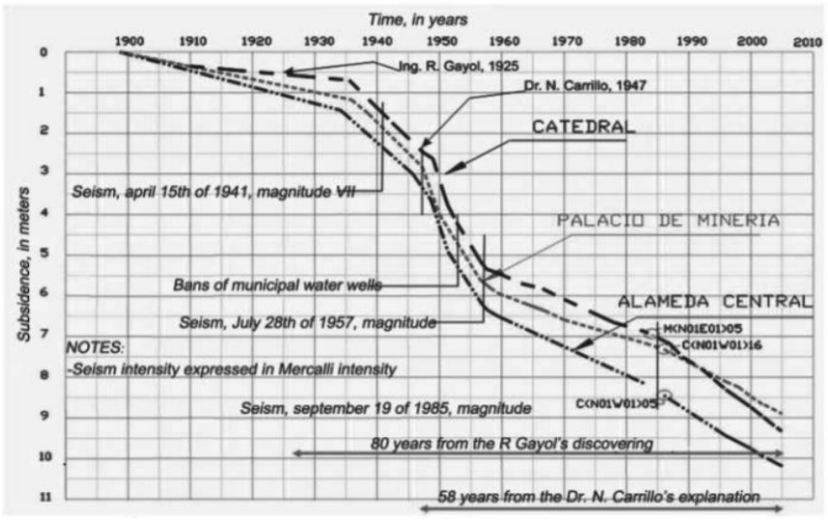

Figure 2.17: Evolution of subsidence in the Historic Center of Mexico City during the period 1898-2005. [From Auvinet et al. (2013)].

Consequently, the increase in effective stress on the subsoil modifies its static and dynamic properties (Ovando-Shelley et al., 2007). Field evidence of changes on shear wave velocities is given in Figure 2.18, from the results of

suspension logging tests performed in 1986 (Jaime, 1987) and 2000 at SCT site (Ovando-Shelley et al., 2007). The expected stiffening of the clay strata over the 15 years period is evident and can also be assessed from the results of resonant column and cyclic triaxial tests performed in those same years on samples retrieved from the same site (Figure 2.18).

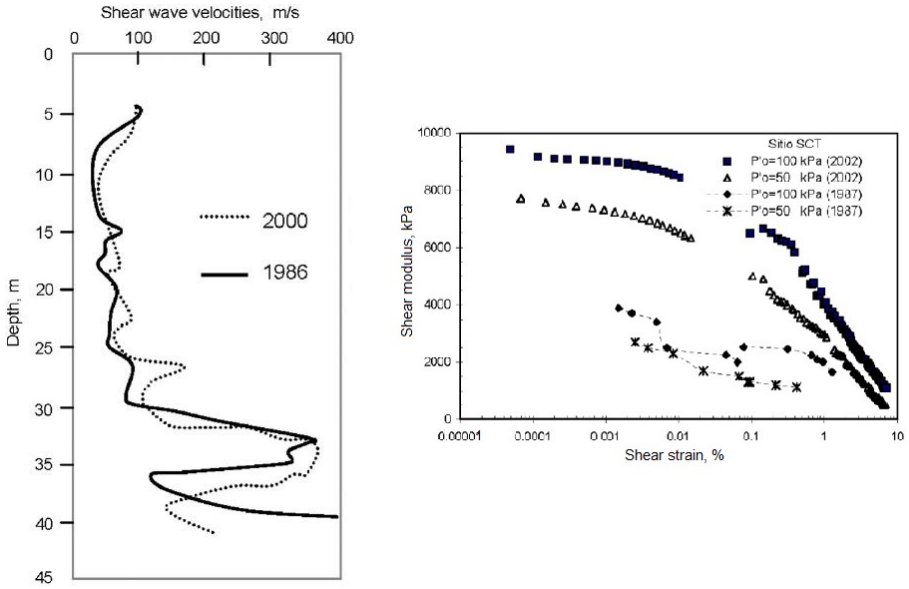

Figure 2.18: Changes in V_S from P-S suspension logging tests performed in 1986 and 2000 at SCT site (left), and change in G_{max} from resonant column and cyclic triaxial tests on samples retrieved from the same site (right). [From Ovando-Shelley et al. (2007)].

The dependency of shear wave velocity on effective stress increments can be stated explicitly from the following expression for the shear modulus at small strains, G_{max}, which was derived from the results of resonant column and cyclic triaxial tests performed on clay samples retrieved from several sites in the former lake bed (Romo and Ovando-Shelley, 1996)

$$G_{max} = \rho V_S^2 = 122 p_a \left(\frac{I}{PI - I_r} \right)^{(PI - I_r)} \left(\frac{p'_0}{p_a} \right)^{0.82} \tag{2.1}$$

where ρ is mass density, p'_0 is the in-situ mean effective stress, p_a is the atmospheric pressure, PI is the plasticity index and I_r is relative consistency. From previous equation it is evident that effective stress increments induced by water pumping from the aquifers lead to an increase of G_{max} and V_S.

The increase in V_S as subsidence takes place, together with the vertical deformation suffered by the clay deposits undergoing regional consolidation, $\delta(t)$, lead to a shortening of the dominant periods of the clay deposits, T_0, as evident from the following equation (Singh et al., 1988b)

$$T_0(t) = \frac{4(h - \delta(t))}{V_S} \tag{2.2}$$

In fact, the decrease in T_0 has been previously studied (e.g., Avilés and Pérez-Rocha, 2010; Martínez-González et al., 2012; Arroyo et al., 2013). In Figure 2.20 are presented the maps of T_0 computed by Arroyo et al. (2013) for 1985 and 2010. They estimated T_0 based on the analysis of site amplification functions obtained analyzing accelerograms recorded in several sites of Mexico City during 1985-2010. The decreases in T_0 are larger in the lake-bed zone where thicker clay deposits exist, with a maximum decrease of about 0.8 s, although there are sites in the southwest part of the lake-bed zone where T_0 has remained constant.

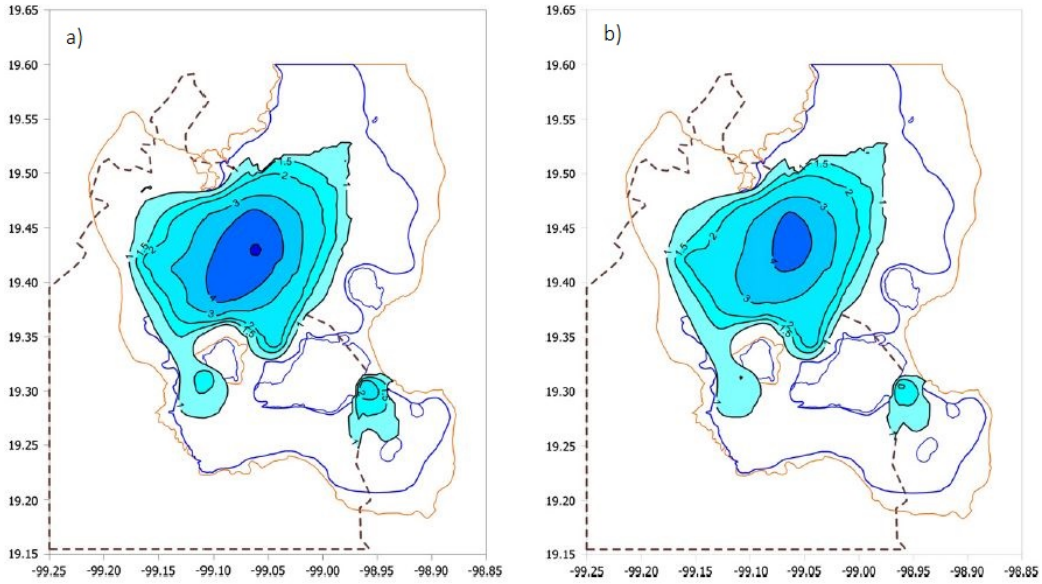

Figure 2.19: Maps of T_0 for Mexico City in (a) 1985 and (b) 2010. [From Arroyo et al. (2013)].

As it will be shown later, iso-period maps are important to understand the damage distribution caused by the 1985 and 2017 earthquakes.

2.5 The September 19, 1985 M_S8.1 earthquake

The disastrous earthquake of Sept 19, 1985 ($M_S = 8.1$) broke a segment of the plate boundary along the Mexican subduction zone known as the Michoacan gap. Analysis of body waves and long-period surface waves shows that the event was an interplate subduction event with a low dip angle fault

plane, $\delta = 9°$, striking parallel to the Mid-America trench, $\varphi = 288°$, and a small component of left lateral motion, $\lambda = 72°$, with a depth of about 17 km (Eissler et al., 1986). The synthetic seismogram which matches the observed waveform requires two subevents separated by 27 sec in time, and each with a seismic moment, M_0, of $2\text{x}10^{20}\ N-m$. The second event on September 21 ($M_S = 7.5$), can be modeled by a single source at a depth of 20 km with a seismic moment of about $1.2\text{x}10^{20}\ N-m$. Aftershock areas, slips, and stress drops of the two earthquakes are 170x50 and 66x33 km^2, 220 and 330 cm, and 19 and 43 bars, respectively (UNAM Seismology Group, 1986).

The Guerrero strong-motion accelerograph array was being installed when the 19 September 1985 earthquake occurred, thanks to a cooperative venture of the Institute of Geophysics and Planetary Physics, U.C. San Diego (J.N. Brune and J.G. Anderson) and the Instituto de Ingenieria, UNAM (J. Prince and S. Singh). The array provided 16 high dynamic range digital records of ground motion from the near-source area and up to a distance of 240 km (Figure 2.20).

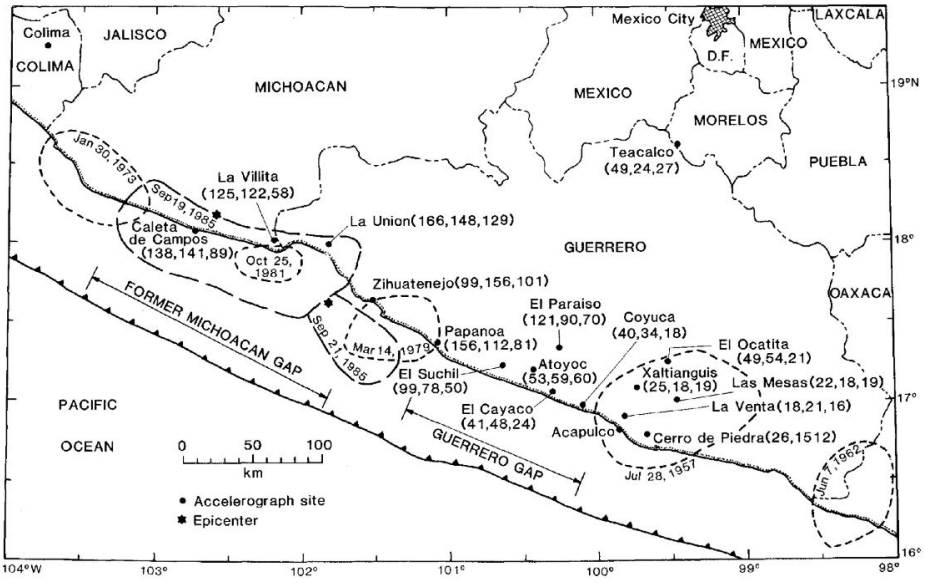

Figure 2.20: Locations of strong motion stations in Guerrero array on 19 September 1985. Short dashed lines show limits of aftershocks of large earthquakes in this region since 1951. Peak ground accelerations (cm/s^2)are given for each station for the north, east and vertical components, respectively, in parentheses. [From Anderson et al. (1986)].

In Mexico City, ground motion was recorded by seven free-field accelerometers, whose locations are shown in Figure 2.21. Stations TACY and CUIP are located on the hill regions, where the soil consists of compact sedimentary layers and basaltic lava flows, respectively. Stations SCT, CDAF and

CDAO, on the other hand are in the lake region covered by soft clay deposits. Stations SXVI and TXSO are located in the transition zone.

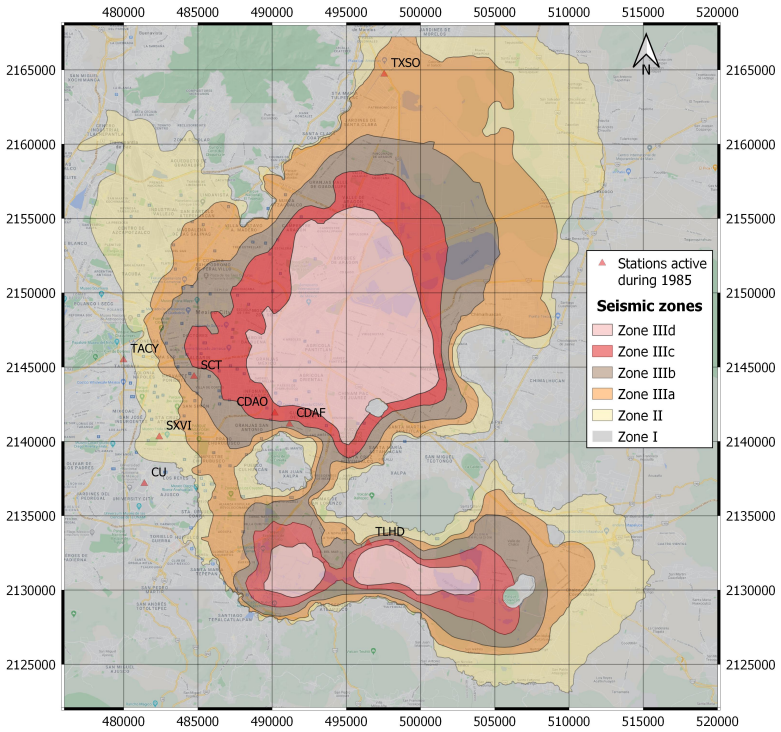

Figure 2.21: Ground motion stations active in Mexico City during the 1985 Michoacán earthquake.

Figure 2.22 shows the north-south component of acceleration for stations Caleta de Campos and La Villita, that were situated directly above the aftershock zone (see Figure 2.20). These accelerograms confirm that there were two subevents in which energy release was relatively more intense (Anderson et al., 1986). In Figure 2.23 are also presented their Fourier Amplitude Spectra (FAS, Appendix A.2). Spectral ordinates increase with frequency from 0.1 to 0.5 Hz, are relatively level to about 2 Hz, and generally decrease above 2 Hz, due to attenuation. These spectra do not show a conspicuous peak at 0.5 Hz like spectra from the lake zone in Mexico City (as it will be shown later), although there is a relative maximum in the spectrum for Caleta de Campos.

Attenuation with distance is shown in Figure 2.23, where the recorded peak horizontal accelerations (PGA) are plotted against the distance from the edge of the aftershock zone. Peak values decrease with distance except for Mexico City (points with distances>300 km). For comparison, Figure 2.24 also shows peak accelerations recorded during the Chile earthquake (M_S7.8, 3

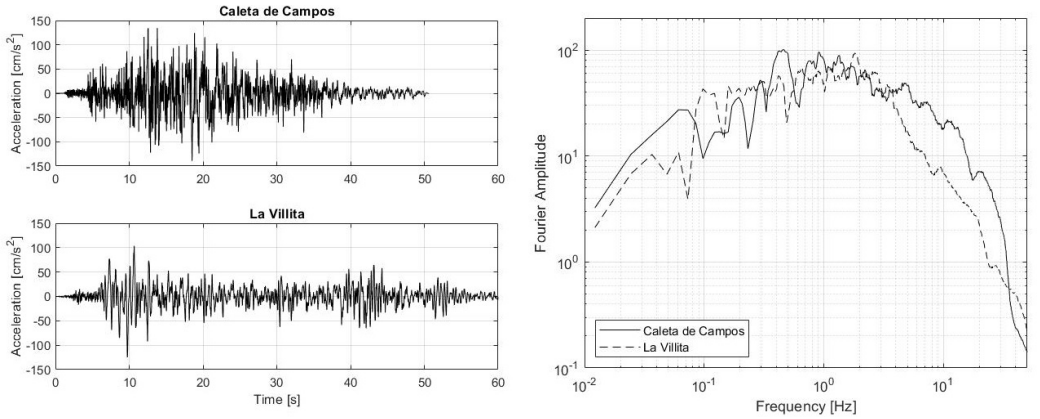

Figure 2.22: North-south component of acceleration for statios Caleta de Campos and La Villita (left) and their corresponding Fourier amplitude spectra (right).

March 1985), another subduction thrust earthquake with a geometry similar to the 19 September event. Peak accelerations for the Mexico data show much less scatter than the Chile data, and seem to be almost a lower bound (Anderson et al., 1986).

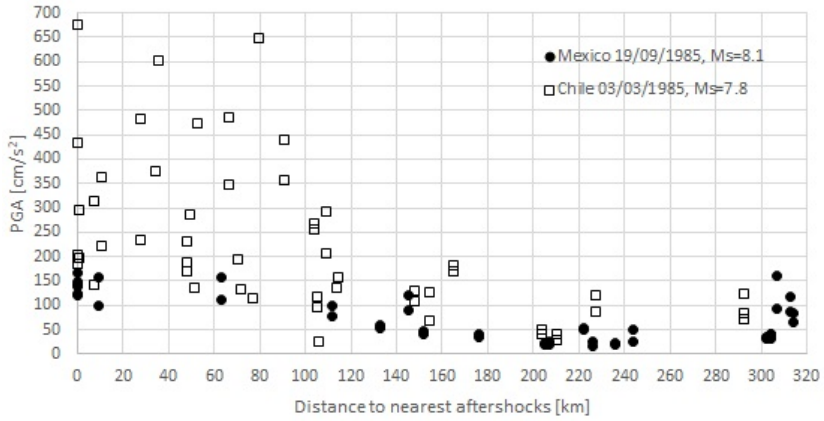

Figure 2.23: Peaks of horizontal components of acceleration plotted against distance outside the boundary of the aftershock zone. [Adapted from Anderson et al. (1986)].

Regarding the ground motion in Mexico City, Figure 2.24 shows a comparison of the east-west acceleration records for three stations. It can be seen from this figure that the ground motion records vary considerably from site to site, not only in amplitude and frequency content, but also in duration. The difference in duration is particularly pronounced for recordings CDAO (lake zone) and TACY (hill zone), where the significant durations computed from the Arias intensity (i.e., time between 5% and 95% of the Arias intensity) are 128 s and 62 s, respectively. PGA at SCT were approximately 500% of those at TACY in the E-W component, so it is evident that there was a ma-

jor amplification of ground motion in the lake zone. In Figure 2.25 are also shown the elastic absolute acceleration response spectra (SA), 5% damping (Appendix A.4), of east-west and north-south recordings for the same sites. The acceleration response spectra for two components of motion at each site show generally similar frequency contents indicating the influence of the local soil conditions in a reasonably consistent manner at each site, although these effects differ considerably from one site to another (Seed et al., 1988).

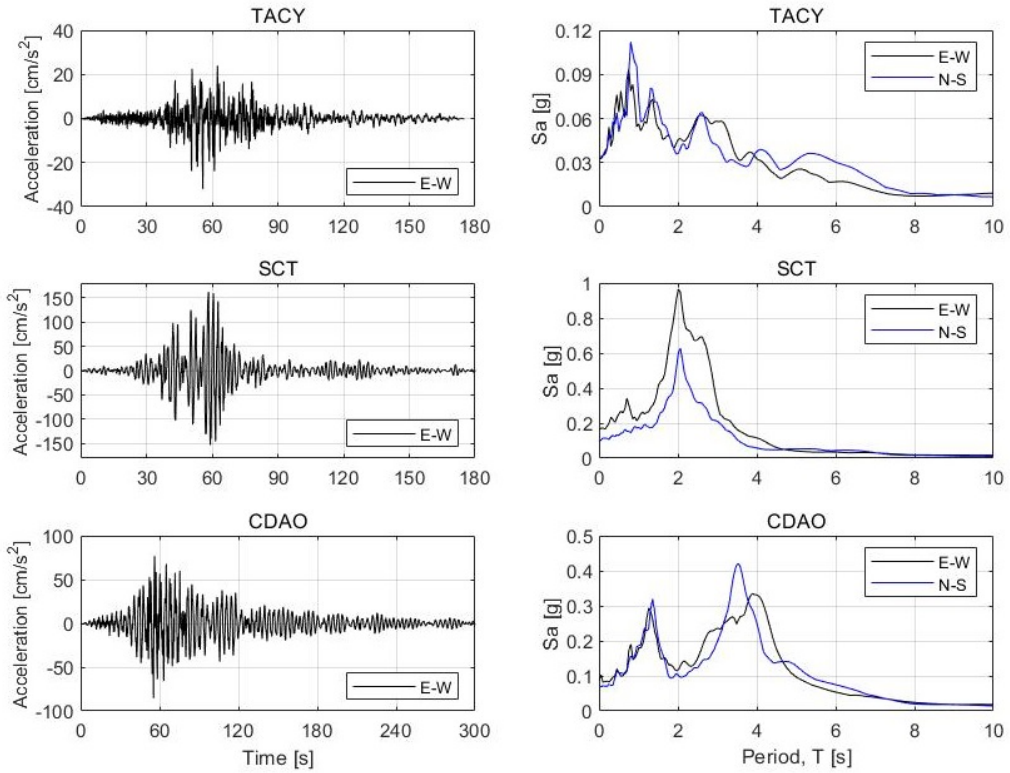

Figure 2.24: E-W accelerograms for three sites in the Mexico City (left). E-W and N-S elastic acceleration response spectra (5% damping) for the same sites (right).

The spatial variability of the ground motion in the lake zone is noticeable from the differences in the response spectra of SCT and CDAO sites; CDAO shows lower peak accelerations and maximum spectral amplifications at higher periods than at the SCT site. At CDAO site, where the thickness of clay deposits was about 56 m, PGA was 0.085 g and the peak spectral acceleration was about 0.35 g at a period of about 3.5 seconds, while at SCT site, where the deep deposits were at about 39 m depth, PGA was 0.164 g and the peak spectral acceleration was about 1 g at a period of about 2 seconds. So clearly, site conditions play a major role on the ground motion amplification.

Site effects may be evaluated experimentally. Consider that the frequency content of a seismogram may be evaluated by convolving source, path and site effects, and the instrument response (Borcherdt, 1970); therefore, the Fourier spectral ratio of the acceleration at a station (j) to the reference station (k), referred as site amplification factor, may be simplified as follows

$$\frac{A_{ij}(f)}{A_{ij}(f)} = \frac{S_i(f)P_{ij}(f)G_j(f)I_j(f)}{S_i(f)P_{ik}(f)G_k(f)I_k(f)} = \frac{G_j(f)}{G_k(f)} \tag{2.3}$$

where $S_i(f)$ is the source term of the i^{th} event, $P_{ij}(f)$ is the path term between the j^{th} station and the i^{th} event, $G_j(f)$ is the site term for the j^{th} station and $I_j(f)$ is the instrument response term for the j^{th} station. Hence, if station (k) is unaffected by any kind of site effects (rock site), the spectral ratio (2.3) represents the ground motion amplification at site (j).

To further illustrate the amplification of the ground motion, the spectral ratios derived from the horizontal components of motions at the SCT and CDAO stations with respect to the TACY station are shown in Figure 2.25. These spectral ratios depict that at the 2 second period the horizontal accelerations at the SCT site were 23-30 times those at the TACY site. In fact, Singh et al. (1988a) quantified local amplification in the lake zone using spectral ratios, relative to hill zone motion. They observed amplification factors as high as 50 at 0.5 Hz.

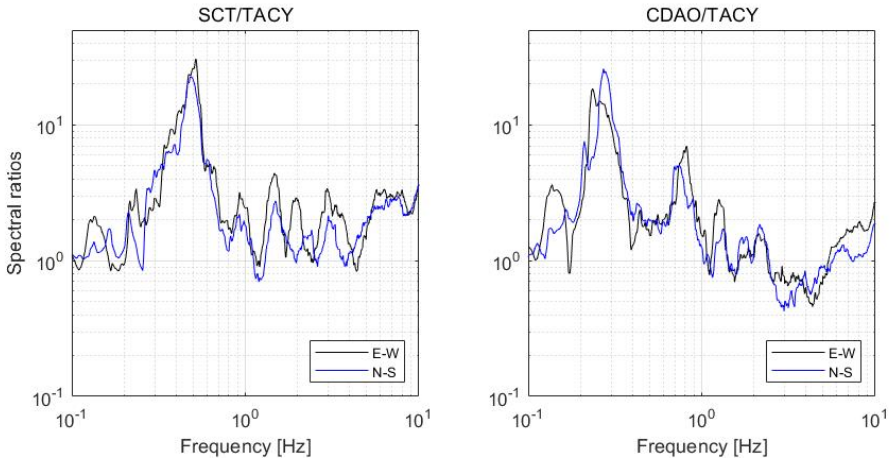

Figure 2.25: Spectral ratios from the horizontal components of motions at the SCT (left) and CDAO (right) stations with respect to the TACY station.

Nearly all buildings that collapsed during the earthquakes of 19 and 21 September were located on the lake-bed zone (Figure 2.26), where at that time the site dominant periods were ∼2 seconds (Arroyo et al., 2013). Considering that N-story buildings have, in Mexico City, a fundamental period

of elastic vibration of about N/10 seconds (Kobayashi et al., 1986), and that during strong ground shaking buildings do not behave elastically, but yield leading to a lengthening of their vibration period, most vulnerable buildings where those in the 6 to 15 story range (Hall and Beck, 1986); in fact, about 20% of these buildings that were located in the area of damage either collapsed or were severely damaged. It is said that these buildings suffered a *double resonance* effect, i.e., earthquake-ground resonance and ground-building resonance. Small 2 to 4 story buildings and modern tall buildings (more than 30 stories) suffered little or no damage.

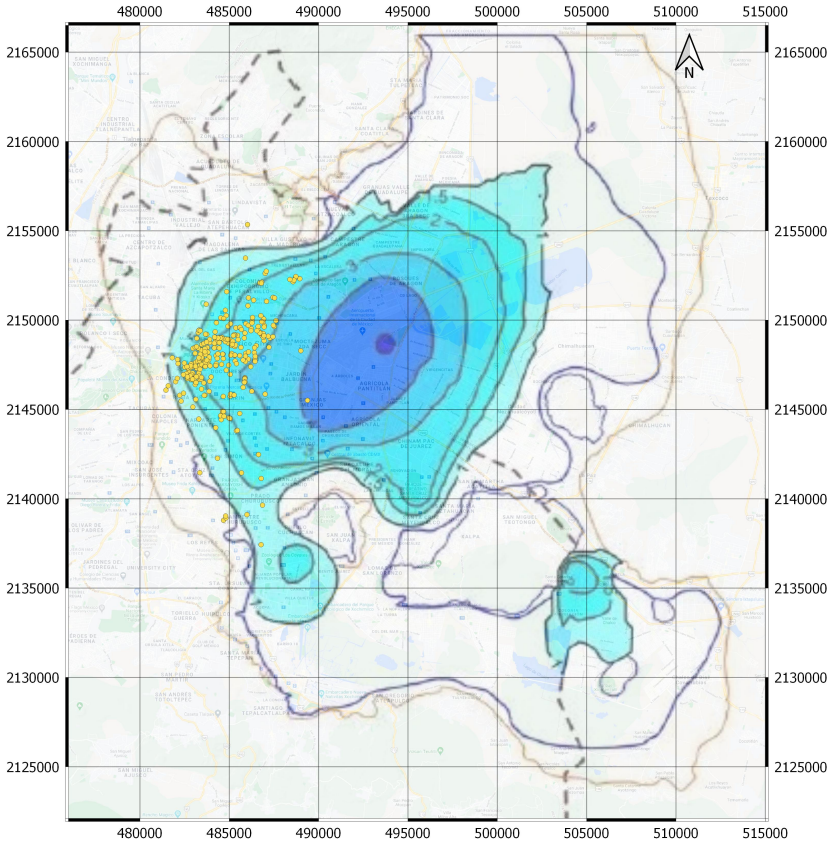

Figure 2.26: Collapsed buildings in Mexico City during the 1985 Michoacán earthquake (yellow dots) placed on the map of estimated T_0 for 1985 (Arroyo et al., 2013).

In 1985, the Building Code of 1976 was in force. The design spectra for the lake zone had maximum ordinates of 0.24 g for non-ductile structures and 0.06 g for ductile ones, while the spectral acceleration from the SCT E-W record reached ordinates of nearly 1 g, so it is not a surprise the large amount of damage (Esteva, 1988).

Some of the factors that contributed to a similar level of strong ground

motion in the epicentral region and more than 300 km from it, in Mexico City, include an anomalous high energy radiation in the frequency band critical for Mexico City, i.e., 0.3-0.7 Hz, (Singh et al., 1988b, 1990), and a regional amplification by a factor 10 in the frequency band 0.3-1 Hz observed in the hill zone of the city (Ordaz and Singh, 1992). Singh et al. (1990) studied the spectral ratios of teleseismic P-waves of the September 19 earthquake with respect to other five large Mexican subduction zone earthquakes and they found that the spectral ratios were anomalously more energetic than those predicted by the ω^{-2} source model in the frequency range 0.3-0.7 Hz. Moreover, large-amplitude ~0.4 Hz waves were also visible in the epicentral velocity traces obtained from the integration of accelerograms (Anderson et al., 1986), as shown in Figure 2.27.

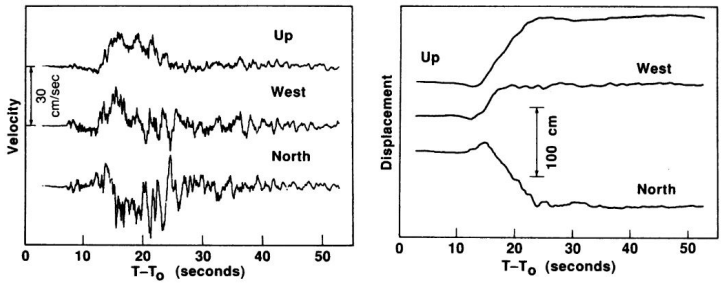

Figure 2.27: Ground velocity and displacement at Caleta de Campos during the 19 September earthquake derived from accelerograms. [From (Anderson et al., 1986)].

Additionally, time histories of vertical displacement computed from accelerograms recorded in Mexico City (Mena et al., 1986) show ripples with periods of about 2-3 sec superposed to longer waves (10-12 sec), as evident in Figure 2.28. Despite the nature of the soil beneath the recording stations is completely different, vertical motions were not much affected from site conditions (Sanchez-Sesma et al., 1988). On the other hand, horizontal components of the displacement were strongly dependent on the characteristics of the soil beneath the stations.Campillo et al. (1988) identified the long period wave as Rayleigh surface wave, whereas the observed (2-3 s) ripples were interpreted as higher-mode crust-guided Lg waves, which are quite efficient between the subduction zone and Mexico City. A comprehensive study of source characteristics and wave propagation from the source to Mexico City was presented in Campillo et al. (1989).

However, a number of experimental and theoretical results have established beyond a doubt that the determining factor of the 1985 catastrophe in Mexico City was a very large local amplification, caused by the presence at the surface of a very thin, extremely soft clay layer (Chávez-García and

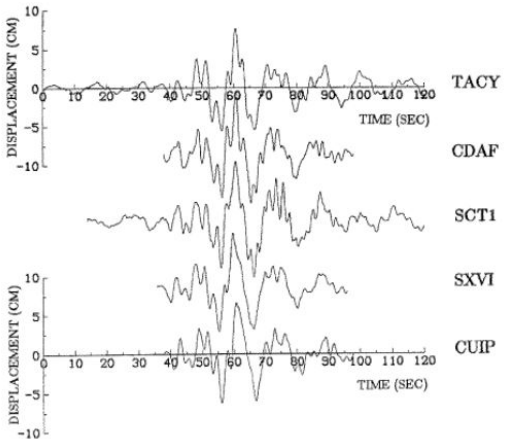

Figure 2.28: Vertical displacement records obtained at different sites in Mexico City, showing ripples with periods of about 2-3 sec superposed to longer waves. [After Mena et al. (1986)].

Bard, 1994). Amplification of the incoming seismic waves in the lake bed zone had been studied before 1985 (e.g., Rosenblueth, 1952; Zeevaert, 1964; Faccioli, 1976a). They all concluded, on the basis of available evidence, that the use of the scalar one-dimensional model of shear wave propagation was appropriate (Sanchez-Sesma et al., 1988).

Considering a one-dimensional shear wave propagation, the transfer or amplification function $H(\omega)$ for an homogeneous elastic soil layer over elastic half-space (Appendix A.5) is

$$|H(\omega)| = \frac{1}{\sqrt{cos^2\left(\omega\frac{H}{\beta_1}\right) + \eta^2 sin^2\left(\omega\frac{H}{\beta_1}\right)}} \tag{2.4}$$

where H is the thickness of the soil deposit, η is the impedance ratio $\eta = \frac{\rho_1\beta_1}{\rho_2\beta_2}$, β_1 and ρ_1 are the shear wave velocity and density of the soil layer, and β_2 and ρ_2 are the shear wave velocity and density of the elastic half-space. Considering $\beta_1 = 80\,m/s$, $\rho_1 = 1400\,kg/m^3$, $\beta_2 = 500\,m/s$ and $\rho_2 = 2000\,kg/m^3$ for the SCT site (see Figure 2.16), its transfer function would be the one shown in Figure 2.29, from which a spectral amplification of $\sim$9 is obtained for the natural frequencies $f_n = (2n+1)\beta_1/4H$, being the fundamental frequency $f_0 = \beta_1/4H = 0.5\,Hz$. The value of f_0 coincides with that obtained from the experimental transfer function (spectral ratios) of Figure 2.27, however, the very large spectral amplification at f_0 and ground motion duration cannot been explained with this simple model, as it will be shown later.

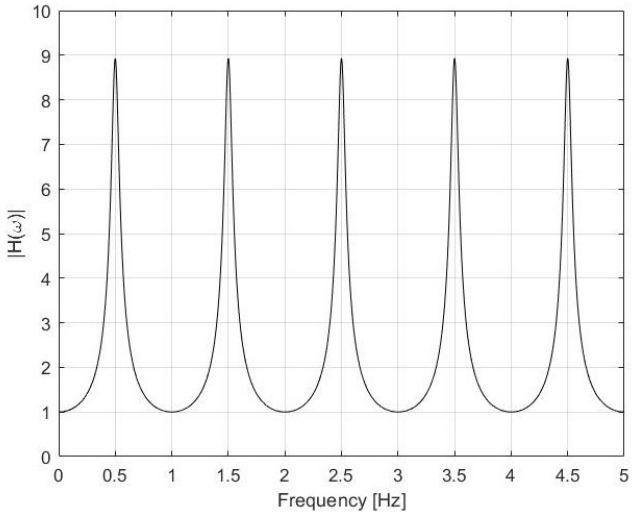

Figure 2.29: Transfer function for SCT site considering a clay layer over an elastic half-space.

Some of the first attempts to evaluate site effects in Mexico City after the Michoacán earthquake, used vertical S-wave propagation models. The use of this model was encouraged by the the fact that the clay deposits are very thin compared to their lateral extent, the high impedance contrast between the clay and its basement, and that the spectral peaks appeared in the characteristic periods of the soils nearby the recording stations. The most comprehensive study using a layered one-dimension model (SHAKE) was that of Seed et al. (1988), who performed a parametric study using a linear-equivalent constitutive model taking into account some uncertainty in the soil properties. Seed et al. (1988) concluded that their model allowed to obtain a 'fair to very good' match of observed response spectra at the surface using a hill zone record as input motion. However, Kawase and Aki (1989) questioned their results. These authors used the geotechnical 1D model proposed by Seed et al. (1988) but instead of making the comparison between observed and computed response spectra, they compared transfer functions in the frequency domain. Their result is shown in Figure 2.30, from which it is clear that in the frequency domain the match is unsatisfactory.

Sanchez-Sesma et al. (1988) concluded that the seismic response of the Mexico basin cannot be satisfactorily explained in terms of one-dimensional shear wave model. From one-dimensional calculations with Haskell's method, using the accelerogram at TACY as input, they found that it was possible to simulate the most intense part of the records at SCT and CDAO, but not the duration (Figure 2.31). Furthermore, they mentioned that the effect of lateral heterogeneities are required in order to better explain damage distri-

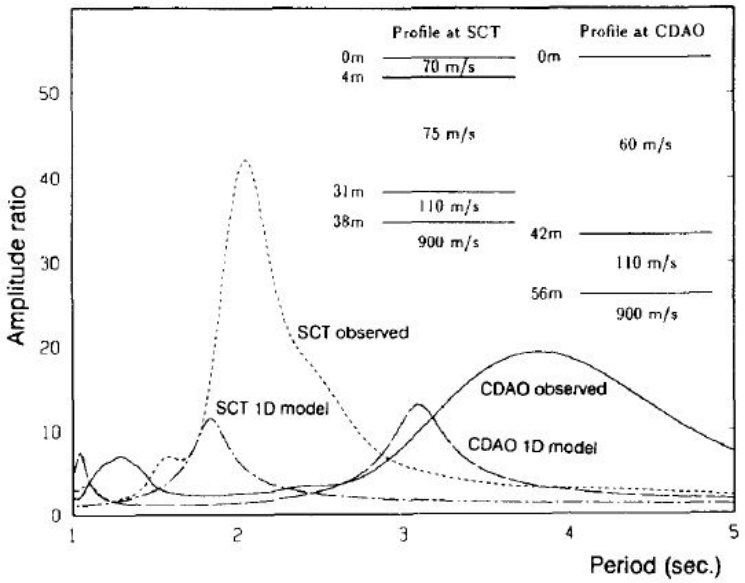

Figure 2.30: Comparison between observed and predicted transfer functions for CDAO and SCT sites using a 1D model with the geotechnical profiles proposed by Seed et al. (1988). [After Kawase and Aki (1989)].

bution. Thus, simple 1D models are able to reproduce relative amplification between soft soil and firm ground sites at Mexico City in the spectral domain, but fail completely to account for the differences in the duration of strong motion between these zones (Chávez-García and Bard, 1994). It is important to mention that long ground motion durations in the lake zone have been observed for many different earthquakes. Therefore, there have been several 2D models advanced to explain the duration characteristics of the lake zone ground motion. The majority of these models focused either on large scale or on small scale lateral heterogeneities.

Horizontal resonance of P waves was proposed by (Seligman et al., 1989) and (Mateos et al., 1993). In theirs 2D model, the two dimensions are horizontal, contrary to what is usual. They propose that the increase of ground motion duration is due to the lateral resonance of energetic, horizontally propagating P-waves, generated by S to P conversion in the clay layer-substratum interface and trapped within a horizontally closed basin. Chávez-García and Bard (1994) that there exists 2D resonance, but at extremely low frequencies and for an unrealistic velocity distribution. In a model with more realistic velocities for the sediments, laterally propagating Rayleigh waves are generated at frequencies near 0.2 Hz.

Gravity perturbations in the wavefield propagating in the soft clay layer (Lomnitz, 1990) has also been invoked to explain the late wave train arrivals

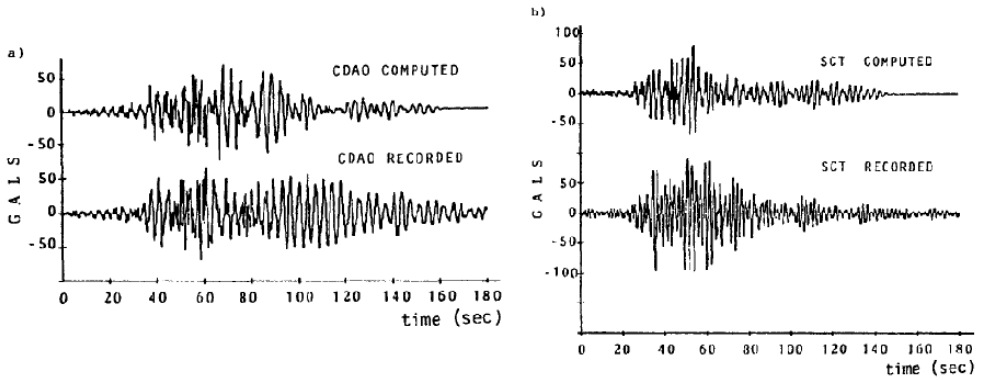

Figure 2.31: Recorded and synthetic accelerograms (NS component) at a) CDAO and b) SCT stations. Modeling was performed with one-dimensional Haskell's method. [From Sanchez-Sesma et al. (1988)].

in the records. However, Chavez-Garcia and Bard (1993) show that gravity perturbations are a very unlikely factor to contribute to strong duration in the Mexico City strong motion records.

It is well known that a closed sedimentary basin will generate surface waves in the sediments due to lateral confinement (e.g., Bard and Bouchon, 1980a,b). Sanchez-Sesma et al. (1988), Bard et al. (1988), Kawase and Aki (1989), Chávez-Pérez and Sanchez-Sesma (1992), among others, have evaluated the effect of the surface waves generated at the basin edge using 2D large scale models. For the sake of illustration, the model studied by Bard et al. (1988) is presented in Figure 2.32, they considered V_S=50 m/s and Q_s=25 for the clay layer, while for the deep deposits they evaluated different velocities profiles and considered Q_s=300. They showed that the deep deposits are responsible for a spectral amplification of 3-7 for frequencies between 0.4 and 1.2 Hz. However, even though surface waves are present and must affect significantly ground motion near the edges of the basin, they attenuate significantly over short distances, due to low velocity of the clay layer together with a low Q_s factor, and cannot propagate very far within the lake bed zone, where observed strong motion records show late arrivals with amplitude comparable to the direct-wave motion (Chávez-García and Bard, 1994). When attenuation is neglected or a large Q_s factor is used for the clay layer, results are radically different. For instance, using Q_s=300, Paolucci and Faccioli (1991) were able to reproduce the observed duration of motion, since in this case surface waves do arrive to the center of the basin with amplitudes comparable to that of the direct S-wave, however, Q_s values in the range of 10-50 are more suitable for the clay deposits according to laboratory (Romo and Ovando-Shelley, 1996) and field measurements (Jongmans et al., 1996).

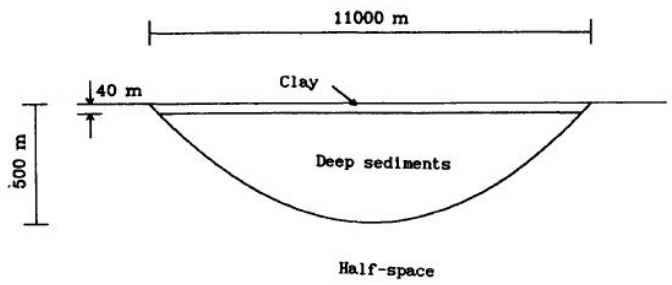

Figure 2.32: 2D model of the large scale structure of Mexico City valley proposed by Bard et al. (1988).

The effect of small scale heterogeneities (in the order of the dominant wavelength in the clay layer) has not been extensively studied because the details of the basin structure are not sufficiently known to follow a deterministic approach (Mayoral et al., 2017). However, the knowledge on the surficial clay layer has vastly increased during the last decades (e.g., Auvinet et al., 2017).

Faccioli et al. (1989) show that introducing local random variations in the V_S profile of the clay layer, an increase in the duration of motion is observed. Campillo et al. (1990) investigated the effects that small, smooth variations of the surficial clay deposits have on seismic motions. Their numerical simulations show that the amplitude and duration of the signal can increase of one order of magnitude with respect to a homogeneous flat clay layer even for periods of several seconds, over distances as small as a few hundred meters apart. This could explain in part the irregular distribution of damages.

Several authors (e.g., Singh and Ordaz, 1993; Barker et al., 1996; Shapiro et al., 1997, 2002; Iida and Kawase, 2004), suggested that long durations may be attributed to dispersion and multipathing between the source and the basin. Singh and Ordaz (1993) proposed that long duration was already in the motion at the hill zone, but that the accelerographs were not sensitive enough to detect it, and such ground motion is enough to excite vibration of the clay layer where it is enormously amplified. The origin of such effects might lie beyond the basin, in the TMVB (Flores-Estrella et al., 2007). Shapiro et al. (1997) showed that a low-velocity layer under the TMVB could cause regional amplification in the 8–10 s interval, and increase the signal duration by surface wave dispersion. Shapiro et al. (2002) concluded that the complete explanation of the extended signal duration observed in Mexico City requires models including low-velocity structures at both regional (e.g., Furumura and Kennett, 1998) and local scales (e.g., Sanchez-Sesma et al., 1988; Kawase and Aki, 1989).

Sánchez-Sesma et al. (1993) suggested 3D effects as the reason for the observed polarization patterns and long ground motion duration. The need for three-dimensional models has also been pointed out by Mayoral et al. (2017).

Shapiro et al. (2001) analyzed ground motions recorded at the surface and in boreholes at five locations in the lake-bed zone. They found that peak displacements in the lake-bed zone between 0.3–0.5 Hz at different depths for several subduction earthquakes are in accordance with theoretical eigenfunctions for the Rayleigh-waves first overtones, so they concluded that the wavefield in the lake-bed zone in Mexico City is dominated by higher-mode surface waves. A very important difference between fundamental and higher modes is that the energy of the fundamental mode is almost completely concentrated in the soft lake sediments, while the higher modes propagate in deeper layers and are thus less affected by the low Q_S of the clay. The role of the superficial clay layer is essentially a passive one of amplifying the seismic waves at the fundamental period of the site, which gives a monochromatic appearance to lake-bed records. Recently, on the basis of 3D numerical simulations results, Cruz-Atienza et al. (2016) confirmed the observation of Shapiro et al. (2001), that the seismic response of the basin is dominated by surface-waves overtones, and they show that this mechanism increases the duration of ground motion by more than 170% and 290% of the incoming wavefield duration at 0.5 and 0.3 Hz, respectively.

To sum up, the 1985 Michoacán earthquake was exceptional on several counts:

- Peak ground accelerations in the epicentral area were low, and still caused severe damage in Mexico City, 360 km away;
- shaking duration inside the basin was exceptionally long and site effects gave place to extremely large spectral accelerations;
- the enormous differences in intensities of shaking and associated building damage in different parts of the city.

Different mechanisms contributed to the severe long lasting ground motion: (i) source effects, i.e., an anomalous high energy radiation in the frequency band critical for Mexico City (0.3-0.7 Hz); (ii) path effects, i.e., duration elongation due to dispersion and multipathing, and regional amplification; (iii) local site effects by the presence of the soft clay layer and the underlying deep deposits, together with large and small scale heterogeneities.

2.6 The September 19, 2017 Mw7.1 earthquake

The 19 September 2017 Mw7.1 Puebla-Morelos earthquake in central Mexico was quite different to that of 1985. It occurred well inland of the megathrust (∼250 km, Figure 2.33) at 18:14:40 GMT (13:14:40 local time) at epicentral coordinates 98.6878°W longitude, 18.3044°N latitude and depth of 57 km, placing it beneath the continental crust and within the subducted Cocos plate (intraplate earthquake). The teleseismic (USGS) and regional (SSN) W-phase moment tensor solutions show a normal faulting mechanism with a dip angle of 44°-47° (Melgar et al., 2018).

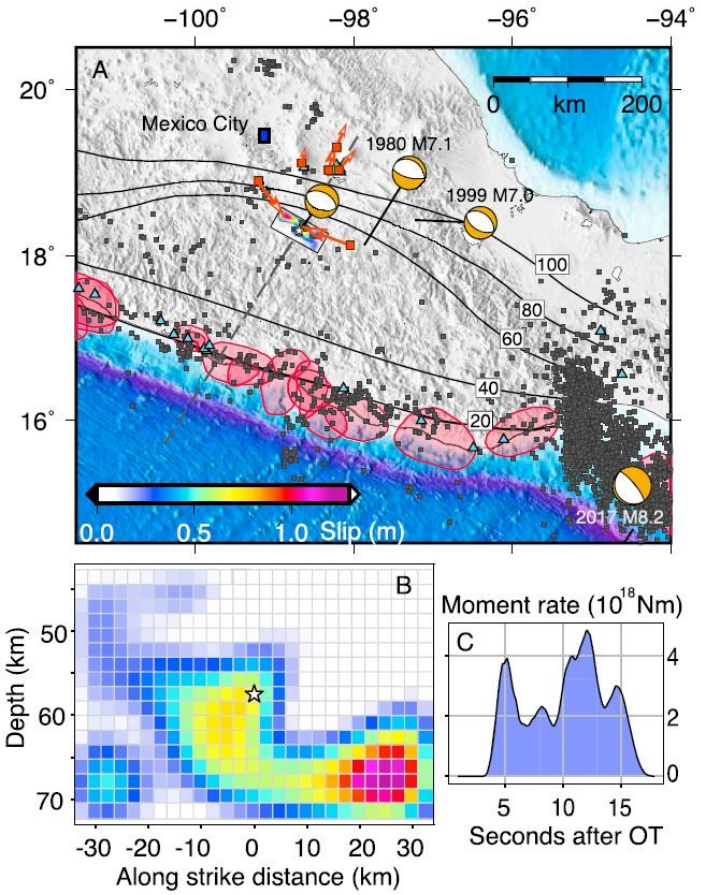

Figure 2.33: (a) Tectonic context. Black squares are epicenters from seismicity in the month of September 2017. Normal faulting focal mechanisms for previous large events in 1980 and 1999 and for the 2017 Mw8.2 Tehuantepec earthquake are shown. The black contours are the 20 km slab depths from Ferrari et al. (2012). White star is the hypocenter for the 2017 Puebla-Morelos earthquake. (b) Slip model, the white star is the event hypocenter. Color scale is the same as in (a). (c) Source time function for the slip model. [From Melgar et al. (2018)].

The proximity of the earthquake to Mexico City (∼120 km) combined with the well-known basin amplification of the ancient lake Texcoco (e.g., Singh et al., 1988a; Chávez-García and Bard, 1994; Cruz-Atienza et al., 2016) led to long duration high-intensity ground motions within the city. In the following, the main differences in the damage pattern and ground motion characteristics in Mexico City, with respect to the 19 September 1985 M_S8.1 earthquake will be highlighted. A comprehensive analysis of this event is presented in Mayoral et al. (2019).

In Figure 2.34 are shown the strong ground motion stations active during the 2017 Puebla-Morelos earthquake. These stations are operated by seismic instrumentation unit within the Engineering Seismology Laboratory of the Instituto de Ingeniería UNAM[1] (IINGEN) and Centro de Instrumentación y Registro Sísmico[2] (CIRES).

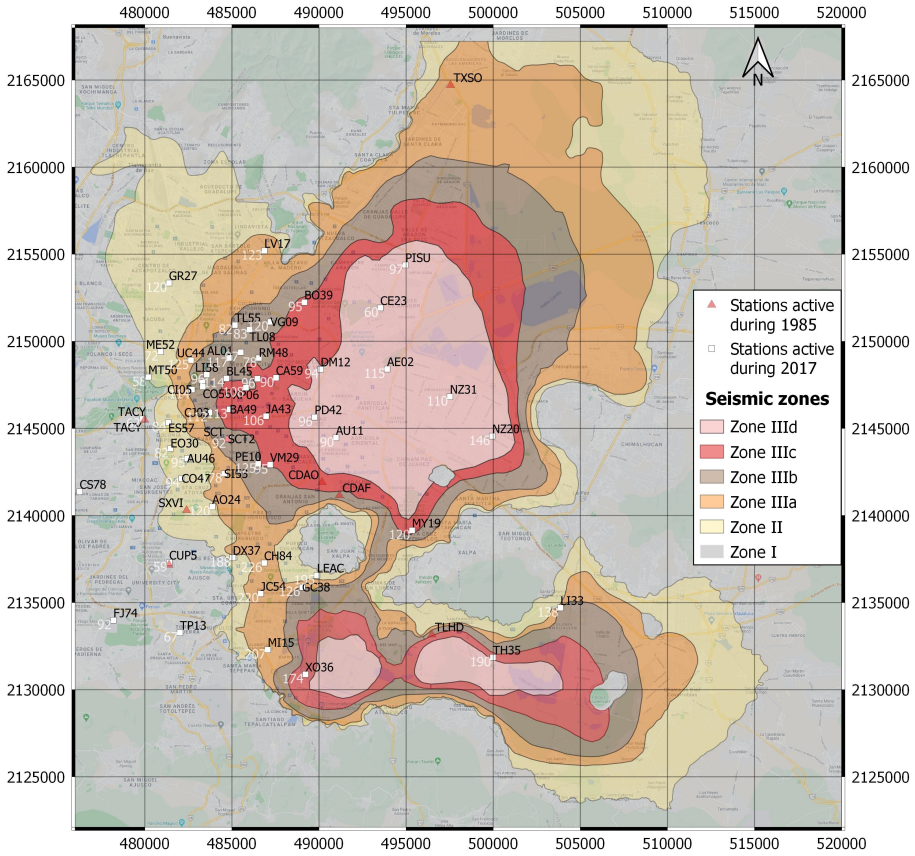

Figure 2.34: Ground motion stations active in Mexico City during the 2017 Puebla-Morelos earthquake. Values in white color represent the PGA (in gals) for the each station.

[1] http:/aplicaciones.iingen.unam.mx/AcelerogramasRSM/
[2] http://cires.org.mx/registro_es.php

Figure 2.35 shows the collapsed buildings during the 1985 Michoacán earthquake and the 2017 Puebla-Morelos earthquake, from which it is clear that the geographical distribution of the damage and its pattern are greatly different. Damage during the 2017 earthquake is concentrated in the transition and IIIa seismic zones, where the site dominant periods are between 0.5-1.5 seconds. Small and low-rise buildings were especially vulnerable, in fact, 64% of the collapsed building were in the range 1-5 stories, while the rest were in the range 6-10 stories (Galvis et al., 2017). In contrast, the damage during the 1985 earthquake occurred mostly in the lake-bed zone (dominant site periods between 1.5-2.5 s) and to high-rise buildings. This difference in the damage pattern was anticipated (e.g., Singh et al., 2015; Iglesias et al., 2002).

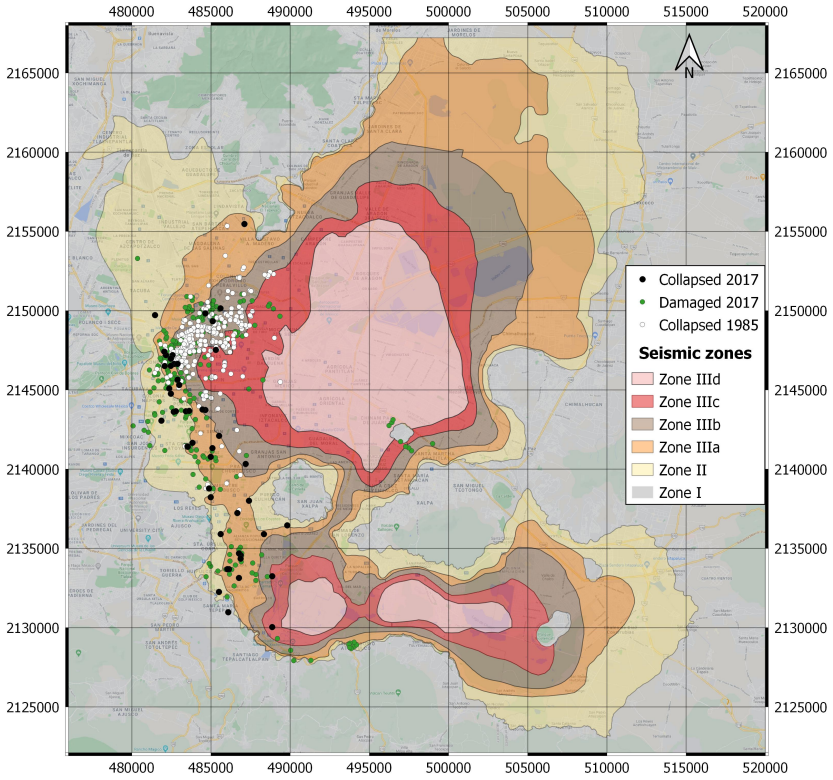

Figure 2.35: Collapsed buildings in Mexico City during the 1985 Michoacán earthquake, and the 2017 Puebla-Morelos earthquake[3].

The interplate earthquakes originate at R>300 km from Mexico City at a 15–20 km shallow depth. The damaging intraslab earthquakes, on the other hand, generally occur at R<250 km and at the 40–80 km depth (Singh et al., 2018). Furthermore, the stress drop, $\Delta\sigma$, of the intraslab events is ∼4

[3]Locations obtained from www.atlasnacionalderiesgos.gob.mx/apps/Sismo19sCDMX/

times greater than that of the interplate earthquakes (García et al., 2004). Consequently, the FAS of intraslab earthquakes at the hill zone are expected to be more enriched at higher frequencies (Singh et al., 1996; Furumura and Singh, 2002). This becomes clear when considering the equation for the corner frequency $f_c \propto (\Delta\sigma/M_0)^{1/3}$ (Brune, 1970).

Figure 2.36 shows the horizontal components of acceleration at CU during the 1985 and 2017 earthquakes. The traces of the 2017 event show that it is enriched at high frequencies as compared with the 1985 event. This is evident in Figure 2.36e,f where the geometric mean of the FAS and SA of the two horizontal components are plotted. The FAS and SA of the 2017 earthquake are greater at f >0.6Hz (T<1.6s), especially at f>1.6Hz (T<0.6s), but smaller at f <0.6Hz (T>1.6s) than during the 1985 earthquake.

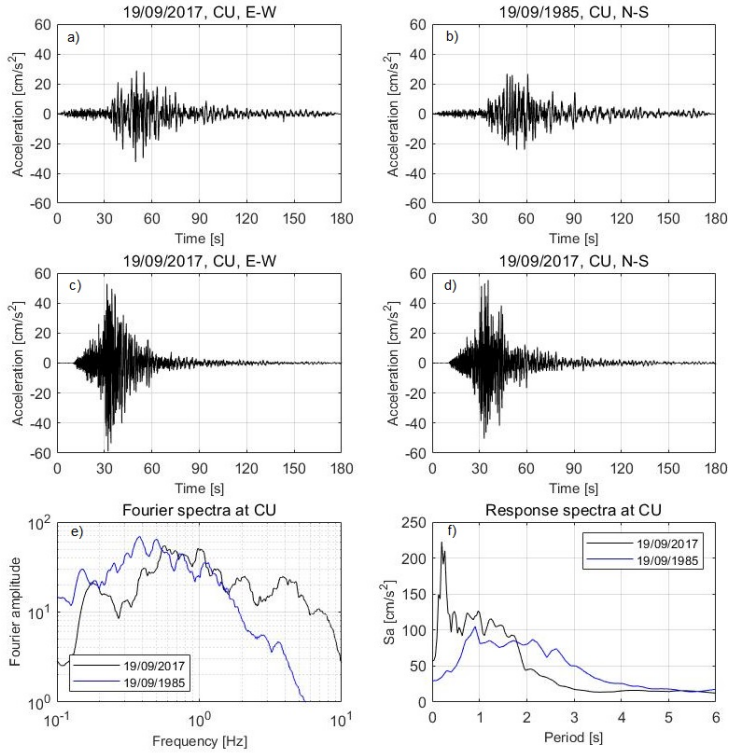

Figure 2.36: (a,b) North–south and east-west accelerograms, recorded at CU station (hill zone), of the 1985 M_S8.1 Michoacán earthquake, (c,d) and the 2017 M_w7.1 Puebla-Morelos earthquake. (e) Fourier amplitude spectra (geometric mean of the two horizontal components) at SCT of the two earthquakes. (f) Geometric mean of elastic response spectra (5% damping) at SCT of the two earthquakes. There is a clear difference in the frequency content; the FAS of the 1985 event (interplate) is peaked between 0.3 and 0.7 Hz, whereas that of the 2017 earthquake (intraslab) is peaked between 0.6 and 1.1 Hz.

Considering that the spectral amplification of seismic waves at sites in the transition and lake-bed zones with respect to CU is roughly invariant (Singh et al., 2018), from Figure 2.36e,f it is possible to conclude that the sites in the transition and lake-bed zones with dominant period T_0 $\leq$1.6 s had greater FAS and SA in 2017 than in 1985. On the other hand, the FAS and SA must have been greater in 1985 than in 2017 at sites with T_0 >1.6 s. Figure 2.37 shows the horizontal components of acceleration and the corresponding geometric mean of the FAS and SA of the two components, for SCT station during the 1985 and 2017 earthquakes. This is the only station in the lake-bed zone that recorded both events. The fact that the the peak spectral acceleration was higher for the 1985 earthquake supports the idea that sites with T_0 >1.6 s had greater FAS and SA during the 2017 earthquake. Supporting evidence of the ongoing shortening of the dominant periods due to regional subsidence (section 2.4.3) is given in Figure 2.37f, where a shortening of T_0 in SCT site from ~2 s to ~1.7 s, occurred during the period 1985-2017.

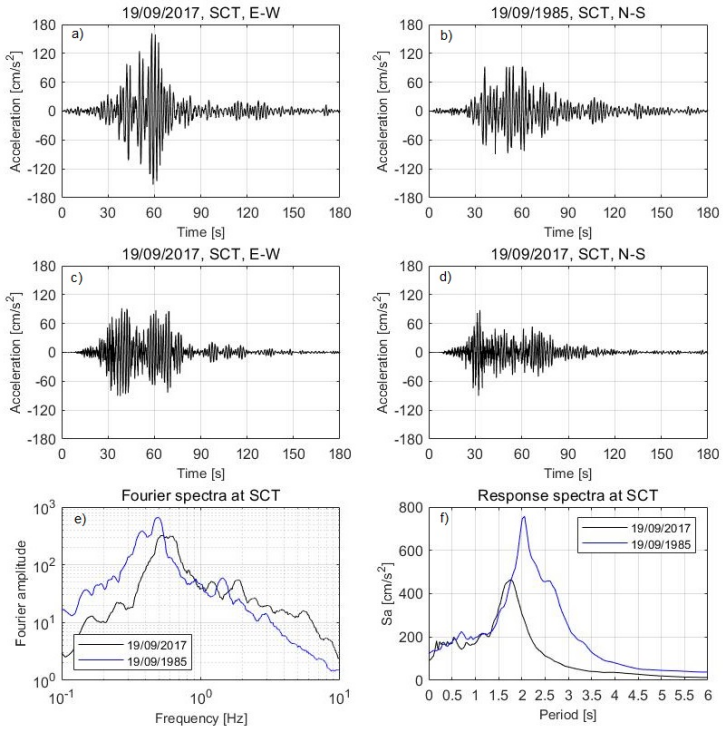

Figure 2.37: (a,b) North–south and east-west accelerograms, recorded at SCT station (lake zone), of the 1985 M_S8.1 Michoacán earthquake, (c,d) and the 2017 M_w7.1 Puebla-Morelos earthquake. (e) Fourier amplitude spectra (geometric mean of the two horizontal components) at SCT of the two earthquakes. (f) Geometric mean of elastic response spectra (5% damping) at SCT of the two earthquakes.

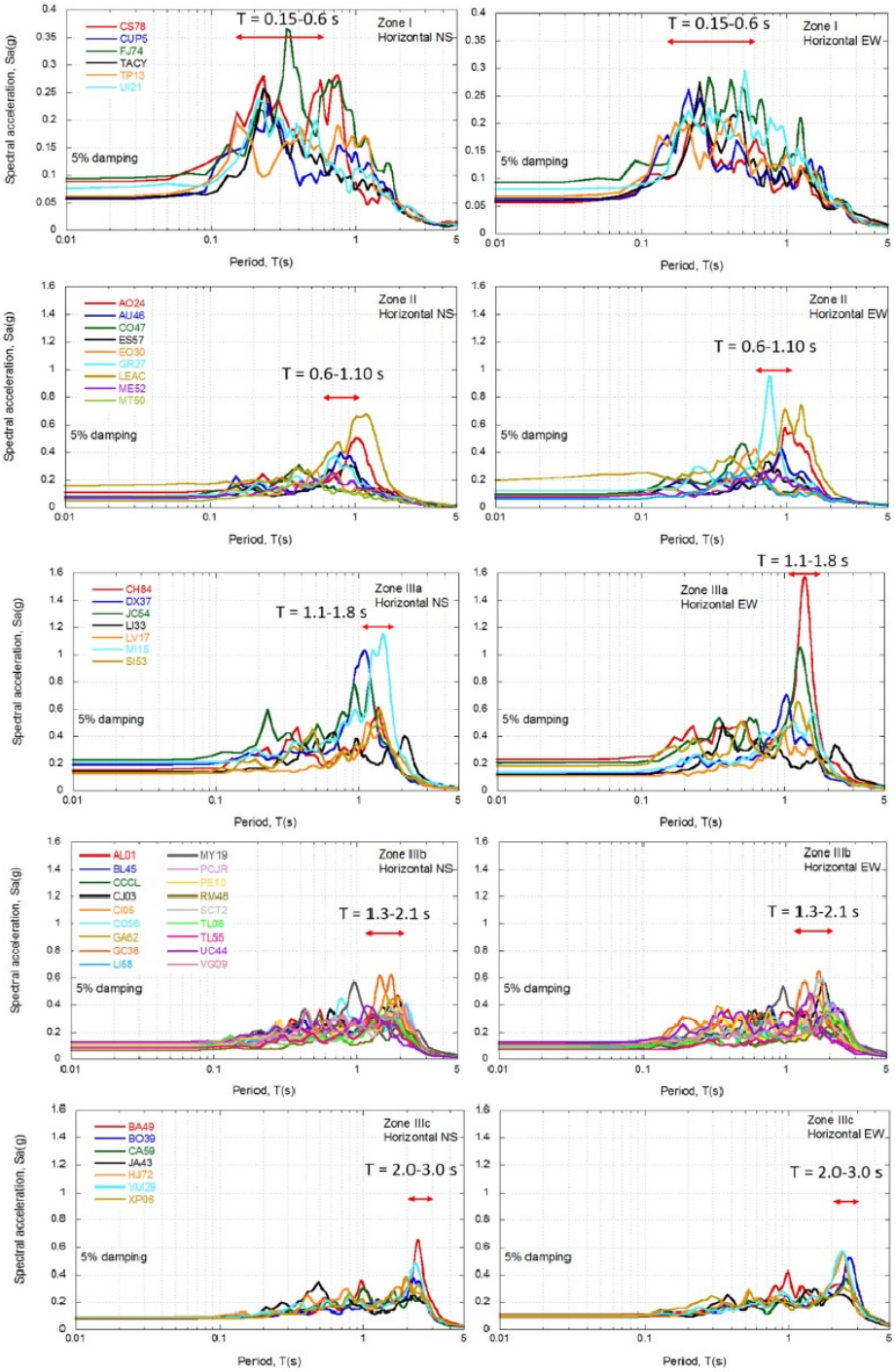

Figure 2.38: Recorded response spectra during the Puebla-Morelos 2017 earthquake for the different seismic zones. The higher SA were measured in the transition and IIIa seismic zones, where most of the buildings collapsed. [From Mayoral et al. (2019)].

Figure 2.38 shows the recorded response spectra during the September 19, 2017 earthquake for the different seismic zones. It can be observed that the larger spectral accelerations of the measured ground motions at each seismic zone fall overall within the range expected, according to the clay layer thickness and geotechnical prevailing conditions at each zone (Mayoral et al., 2019). The maximum peak ground acceleration was PGA=0.226 g, and the maximum spectral acceleration, SA=1.548 g at a period T_0 =1.42 s, registered in the station Culhuacan (CH84) in Coyoacan, located in seismic zone IIIa.

Similarly to the 1985 Michoácan Earthquake, there was an important spatial variability of ground shaking during the 2017 event. Spatial variability is briefly described for Roma and Condesa neighborhoods (Figure 2.39), which were some of the most affected areas. Figure 2.40a,b shows E-W accelerograms at stations CI05 and CO56, which are separated just ∼500 m. Duration is the first evident difference, the significant duration (Arias intensity 5-95%) for CO56 site is 69 seconds, while for CI05 site is just 50 seconds. Figure 2.40c shows the spectral ratios of both stations with respect to TACY station (hill zone), from which is evident the difference in T_0. Moreover, station CI05 shows greater amplifications for frequencies higher than 0.5 Hz, which can also be seen in Figure 2.40d where the SA of both stations is presented. These differences obviously cannot been described with one-dimensional models and most probably are the result of 3D effects.

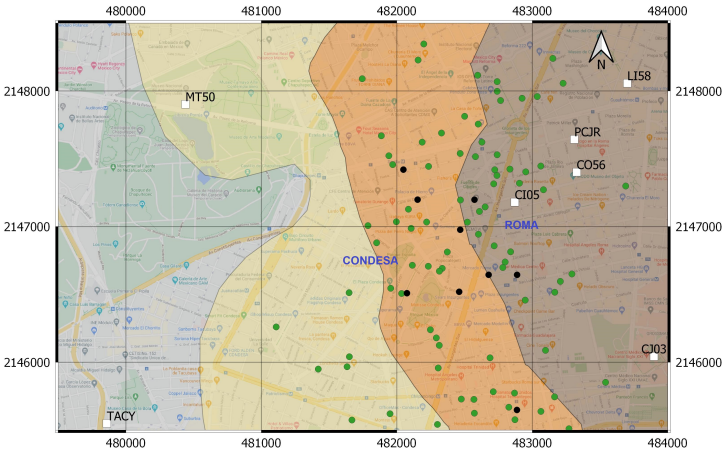

Figure 2.39: Zoom to the Roma and Condesa neighborhoods. Black dots represent the collapsed buildings, while green dots represent severely damaged buildings.

It was observed in Figure 2.35 that most of the collapsed buildings were located in the transition and IIIa seismic zones, where also the highest spectral accelerations were recorded (Figure 2.38), hence, part of the damage

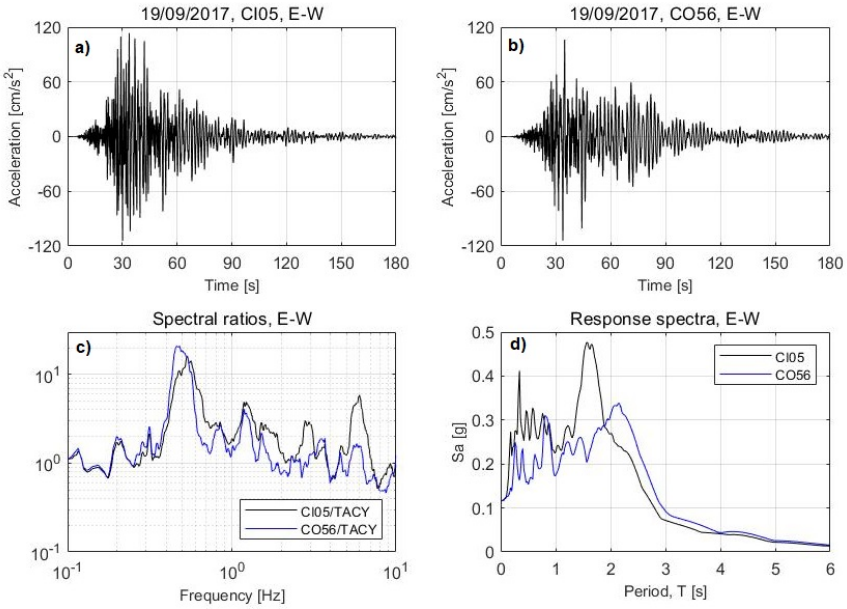

Figure 2.40: E-W accelerograms at stations CI05 (a) and CO56 (b). c) Amplification functions of the E-W component of stations CI05 and CO56 with respect to station TACY (hill zone). d) SA of the E-W component of stations CI05 and CO56.

distribution can be related to site effects. However, from the SA in Figure 2.38, the elastic design spectra of the 2004 Mexico City's building code (in force during the earthquake, Figure 2.41) was exceeded at only two sites in the lake-bed zone (CH84 and DX37), three sites in the transition zone (GR27, EO30 and CO47), and one site in the hill zone (FJ74). Therefore, the large ground motion during the 2017 earthquake was not the only cause of the disaster. In fact, in the Roma and Condesa neighborhood, the spectral intensities did not reach even 50% of the design spectrum.

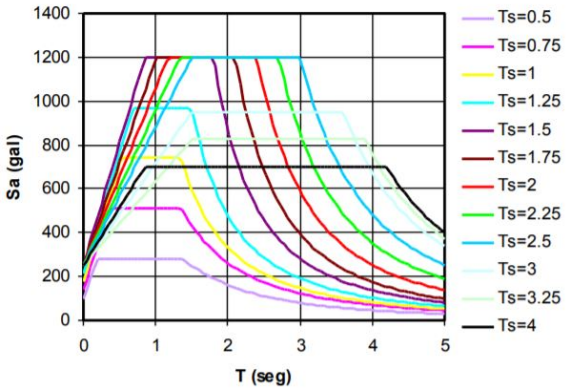

Figure 2.41: Design spectra in force during the Puebla-Morelos 2017 earthquake for different dominant site periods, according to the 2004 Mexico City's building code.

The large majority of the buildings that collapsed had one or more of the following characteristics: (1) being older pre-1985 (in 90% of the cases) non-ductile reinforced concrete structures, so probably after the 1985 earthquake, inadequate attention was given to the seismic evaluation/retrofitting of existing structures; (2) having a structural lateral resisting system consisting of flat-slabs supported by reinforced concrete columns (Figure 2.42); and (3) having a soft story, where the most common case is the presence of parking garage in the ground level while upper stories have many infill masonry walls making them laterally stronger and stiffer (Figure 2.43). Also very common (in 41% of the cases) were buildings located in block corners where effects of torsion are typically more severe (Galvis et al., 2017).

Figure 2.42: Collapsed building with flat slab system at Viaducto Miguel Alemán 106, Piedad-Narvarte, before the 2017 Puebla-Morelos earthquake (left) and after the earthquake (right). [From Galvis et al. (2017)].

Figure 2.43: a) Residential building collapsed due to soft first story at Balsas 18, Miravalle, before the 2017 Puebla-Morelos earthquake (left) and after the earthquake (right). [From Galvis et al. (2017)].

Perhaps one of the most important lessons from this earthquake is the need to devote more attention to existing structures (Galvis et al., 2017). As a matter of fact, the latest version of the Mexico City's building code, released after the earthquake, on December 15 2017, includes guidelines for assessing and retrofitting existing buildings (GCDMX, 2017).

Chapter 3

3D Physics-Based Numerical Simulations

3.1 Introduction

Tools for earthquake ground motion prediction (EGMP) are one of the key ingredients in seismic hazard assessment, both within probabilistic and deterministic frameworks, with the seminal objective to provide estimates of the expected ground motion at a site, given an earthquake of known magnitude, distance, faulting style, etc. A variety of procedures for EGMP has been proposed in the past four or five decades (Figure 3.1), relying, on one side, on different information detail on the seismic source and propagation path, and, on the other side, providing different levels of output, either in terms of peak values of ground motion or of an entire time history. The level itself of complexity of the proposed procedures ranges from the empirical ground motion prediction equations, typically calibrated on the instrumental observations from real earthquakes, up to complex 3D numerical models, involving as a whole the system including source - propagation path – shallow soil layers (Paolucci et al., 2014).

In the absence of suitable and performing numerical tools for physics-based modeling of source and path effects, research in the past was mainly directed towards statistical processing of available records to provide empirical ground motion prediction equations (GMPEs, Appendix A.3). Recently, Douglas (2011) compiled about 300 of such equations to estimate peak ground acceleration (PGA) and about 200 to estimate the response spectral ordinates, published between 1964 and 2010. However, in spite of their overall effectiveness and ease of use, GMPEs suffer of intrinsic limitations: (1) the low availability of records in the range of major potential interest for engineering applications, speciall in the near-source region of large destructive earthquakes; (2) they refer to generic site conditions; (3) they only provide peak values of ground motion, whereas the use of nonlinear time-history

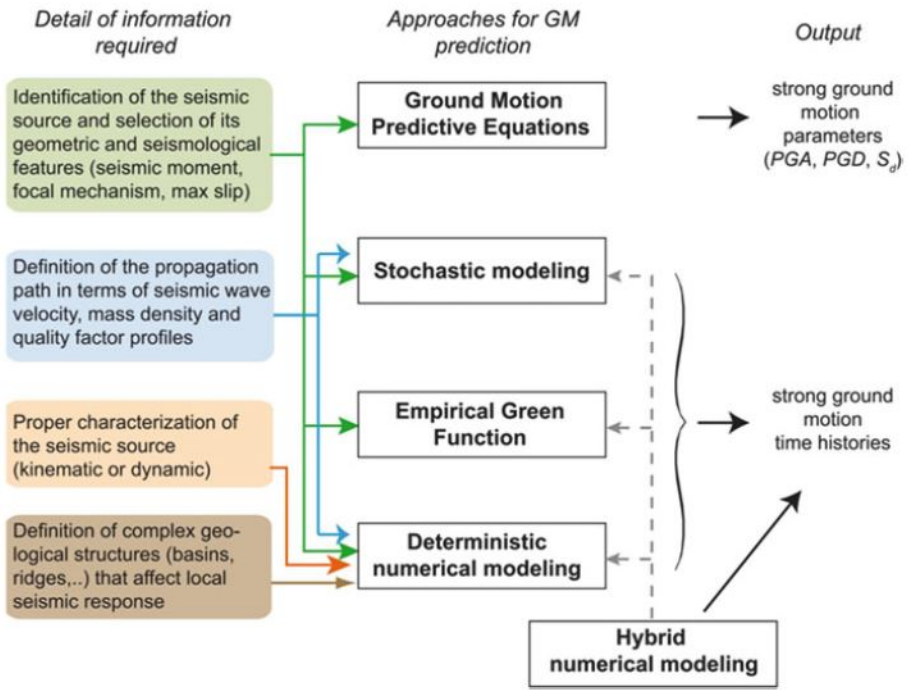

Figure 3.1: Overview of approaches for earthquake ground motion prediction. [From Paolucci et al. (2014)].

analyses requiring reliable input motions is becoming more and more relevant within many applications of performance-based seismic design; (4) they are not suitable to be used for seismic scenario studies where the realistic representation of spatial variability of ground motion is an issue.

To overcome these limitations, three-dimensional physics-based numerical simulation (PBS) of earthquake ground motion has emerged as a powerful alternative tool to the use of GMPEs. Based on the rigorous numerical solution of the elastodynamics equation, simulations provide synthetic ground motion time histories reflecting the physics of the seismic wave propagation problem from the source up to the site of interest, including directivity effects in near fault conditions, topographic and complex site effects (Figure 3.2). This is also the reason for which a high level of detail is required in the input necessary to create a 3D numerical model, and that the entire process to generate a 3D PBS become onerous.

Although the use of PBS use remains rather limited in engineering practice, such an approach has become feasible and mature enough owing to the ever-increasing availability of parallel high-performance computing, and to the increasing number of verification experiments (e.g., Bielak et al., 2010; Chaljub et al., 2010) and validation studies against real recordings (e.g.,

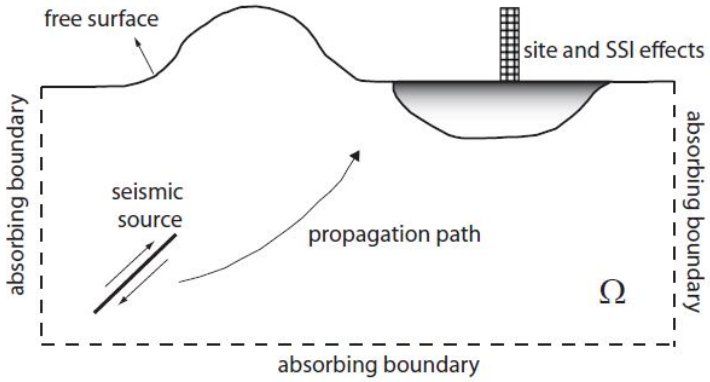

Figure 3.2: Sketch of an idealized model for physics-based numerical simulation of earthquake ground motion. These models encompass a properly characterized seismic source, the propagation path through heterogeneous earth media and site or soil-structure interaction effects. [From Smerzini (2010)].

Taborda and Bielak, 2013; Paolucci et al., 2015).

One of the main drawbacks of 3D physics-based numerical simulation is that the reliability range of synthetics is most often limited to 1-2 Hz (Paolucci et al., 2014), owing to the limitations posed both by computational constraints as well as by the lack of detailed knowledge to construct a geological model with sufficient details also at short wavelengths. This restricts its applicability in earthquake engineering applications, such as structural analyses and risk assessment studies, which require the use of ground motion time histories with realistic features in a broad range of vibration periods (0–10 Hz).

To overcome this issue, the frequency range of the numerical simulations is often enlarged to produce broadband waveforms, generally, by using hybrid approaches combining low-frequency results from deterministic PBS with high frequency signals from stochastic approaches (e.g., Boore, 2003; Mai et al., 2010) are used. More recently, Paolucci et al. (2018) presented a method in which the response spectral accelerations at short periods, are predicted from the long period spectral ordinates, obtained from the results of PBS, using an artificial neural network previously trained on a database of recorded earthquake ground motions.

Relatively few numerical codes exist for the 3D physics-based numerical simulation of earthquake ground motion, mostly belonging to the classical finite difference (e.g., Graves, 1996) and finite element (e.g., Bielak et al., 2005) schemes, while spectral element methods (SEM) (e.g., Faccioli et al., 1997; Komatitsch and Vilotte, 1998) have emerged subsequently as an alternative powerful technique, relying on a right balance between accuracy,

ease of implementation and parallel efficiency. It is not surprising that three open source codes recently made available belong to the SEM family, namely, SPECFEM3D[1], EFISPEC2[2] and SPEED[3], the latter one being illustrated in the next section.

The general procedure to perform a 3D physics-based numerical simulation with the use of SPEED, depicted in Figure 3.3, consists of the following steps

1. Collection of the input data, namely, geological and geotechnical characterization, characterization of the seismic source, topography and bathymetry;
2. Setup of the 3D numerical model with the previous information;
3. Generation of an earthquake scenario, i.e., to produce a kinematic slip model along a given fault within a prescribed magnitude. This can be accomplished with the use of dedicated pre-processing tools;
4. Numerical simulation through SPEED code running on parallel computer architectures;
5. Post-processing to generate ground shaking maps. Broadband waveforms could be obtained using a dedicated tool based on the use of an Artificial Neural Network.

3.2 SPEED: SPectral Elements in Elastodynamics with Discontinuous Galerkin

SPEED (SPectral Elements in Elastodynamics with Discontinuous Galerkin) is an open-source numerical code developed in the framework of the joint research activity between Munich Re and Politecnico di Milano, suitable to address the general problem of elastodynamics in arbitrarily complex media (Mazzieri et al., 2013). SPEED allows the simulation of large-scale seismic wave propagation in visco-elastic three-dimensional media, including the coupled effects of a seismic fault rupture, the propagation path through Earth's layers, localized geological irregularities such as alluvial basins and topographic irregularities, by exploiting non-conforming grids and/or variable approximation orders.

[1] www.geodynamics.org/cig/software/specfem3d
[2] efispec.free.fr
[3] speed.mox.polimi.it

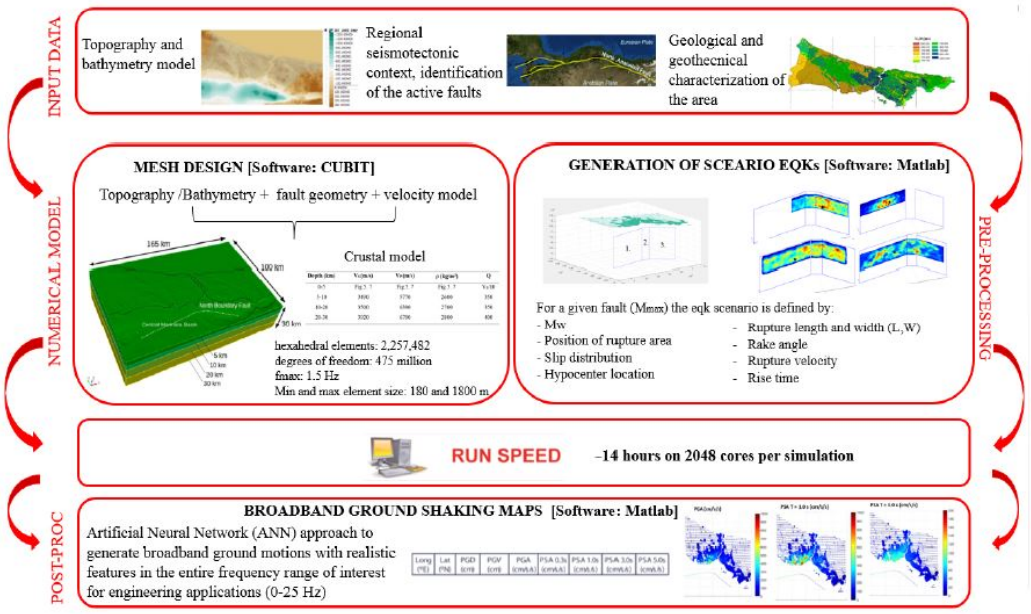

Figure 3.3: Procedure to generate 3D numerical Simulations. [From Infantino (2016)].

The spectral element method, introduced first in fluid dynamics ((Maday and Patera, 1989; Patera, 1984)), can be related to the N-version of the finite element method (Babuška et al., 1981; Babuška and Suri, 1987). As described by Mazzieri et al. (2013), the main idea behind the SEM is that the finite dimensional space is made by high order (piecewise) interpolants,that is, the Lagrangian polynomials, sampled at the Legendre–Gauss–Lobatto (LGL) quadrature points. This discretization technique retains the geometrical flexibility of low order finite elements while featuring the accuracy typical of spectral methods. Indeed, one of the key points of the SE method is the capability of providing an arbitrarily accurate numerical solution by simply enhancing the polynomial approximation degree (Canuto et al., 2006).

In the following, the fundamental equations of elastodynamics, as implemented in SPEED, area described. Consider an elastic heterogeneous medium occupying an open, bounded region $\Omega \subset R^3$, with Lipschitz boundary $\Gamma := \partial\Omega$. The boundary consists in the portions Γ_D, where the displacement vector $\mathbf{u}$ is prescribed, Γ_N where the external surface loads apply, and Γ_{NR} where suitable non-reflecting boundary conditions are imposed. It is assumed that Γ_D,Γ_N and Γ_{NR} are disjoint. For numerical wave propagation problems in unbounded earth media Γ_D is usually empty.

Having fixed the temporal interval $[0, T]$, with T real and positive, the equilibrium equations for an elastic medium, subject to an external force $\mathbf{f}$ (seismic source) read:

$$\begin{cases} \rho\partial_{tt}\mathbf{u} - \nabla\cdot\underline{\sigma}(\mathbf{u}) = \mathbf{f}, & \text{in } \Omega \text{ x } (0,T], \\ \mathbf{u} = 0, & \text{on } \Gamma_D \text{ x } (0,T], \\ \underline{\sigma}(\mathbf{u})\cdot\mathbf{n} = \mathbf{t}, & \text{on } \Gamma_N \text{ x } (0,T], \\ \text{non reflecting boundary conditions} & \text{on } \Gamma_{NR} \text{ x } (0,T], \\ \partial_t\mathbf{u} = \mathbf{u}_1, & \text{in } \Omega \text{ x } 0, \\ \mathbf{u} = \mathbf{u}_0, & \text{in } \Omega \text{ x } 0, \end{cases} \tag{3.1}$$

where $\mathbf{u} = (u_1, ..., u_d)^\top$ is the medium displacement vector, $\underline{\sigma}$ the Cauchy stress tensor, t the time variable variable, $\mathbf{n}$ is the unit outward normal vector to Γ and ρ the material density, and where $\mathbf{u}_0$, $\mathbf{u}_0$ are the given (smooth enough) functions. Here and after ∂_t denotes the partial derivative with respect to time, while $\nabla\cdot\underline{a} = \sum_{j=1}^{d}\frac{\partial\underline{a}_{ij}}{\partial x_j}$ represents the divergence of the tensor $\underline{a}$. It is assumed that on Γ_D the medium is rigidly fixed in the space and on Γ_N surface tractions $\mathbf{t}$ are prescribed. Finally, on Γ_{NR} non-reflecting boundary conditions are imposed, introducing a fictitious traction $\mathbf{t}^*$, that will be defined later. To complete the system in (3.1), initial conditions $\mathbf{u}_1$ and $\mathbf{u}_0$ are prescribed, for the displacement and velocity, respectively.

The stress tensor in (3.1) is related to the displacement field by Hooke's law

$$\underline{\sigma}(\mathbf{u}) = \lambda(\nabla\cdot\mathbf{u})\mathrm{I} + 2\mu\underline{\varepsilon}(\mathbf{u}),$$

with

$$\underline{\varepsilon}(\mathbf{u}) = \frac{1}{2}(\nabla\mathbf{u} + \nabla\mathbf{u}^\top)$$

where $\underline{\varepsilon}(\mathbf{u})$ is the strain tensor, I is the identity tensor and λ, μ are the Lamé elastic coefficients.

At the artificial model boundary Γ_{NR}, waves travelling out of the domain Ω need to be absorbed. A first order approximation (3.2) close to the one proposed by Stacey (1988) is adopted. It is based upon a one-way treatment that perfectly absorbs waves impinging at right angles to the boundary, but that is less effective for waves that graze the boundary (Clayton and Engquist, 1977).

$$\mathbf{t}^* = \rho(V_P - V_S)(\mathbf{u}_t\cdot\mathbf{n})\mathbf{n} + \rho V_S\mathbf{u}_t, \qquad \text{on } \Gamma_{NR} \tag{3.2}$$

where $V_P = \sqrt{(\lambda+2\mu)/\rho}$ and $V_S = \sqrt{\mu/\rho}$ are the propagation velocities of Primary (P) ans Secondary (S) waves, respectively. P and S waves travel from the source through the interior of the elastic medium and follow paths refracted by the varying density and stiffness of the materials encountered.

In order to model visco-elastic media within the framework of discrete grid time domain schemes, approximate techniques have been proposed making use of a suitable modification of the equation of motion (e.g. Graves, 1996). This is the approach used in SPEED to account for spatially varying visco-elastic materials (Mazzieri et al., 2013), characterized by a suitable decay factor $\xi[s^{-1}]$. The governing equation is then modified by introducing two equivalent volume forces. Thus, the equation of motion becomes

$$\rho\partial_{tt}\mathbf{u} + 2\rho\xi\mathbf{u} + \rho\xi^2\mathbf{u} - \nabla\cdot\underline{\sigma}(\mathbf{u}) = \mathbf{f}, \qquad \text{in } \Omega \text{ x } (0,T]. \tag{3.3}$$

It can be shown (Kosloff and Kosloff, 1986) that, with such replacement, all frequency components are equally attenuated, resulting in a frequency proportional quality factor

$$Q = Q_0\frac{f}{f_0},$$

where $Q_0 = \pi f_0/\xi$, being ξ the decay factor and f_0 a reference value representative of the frequency range to be propagated (see Stupazzini et al., 2009).

Furthermore, SPEED also allows to model hysteretic damping , i.e., frequency-independent Q, as in the Generalized Maxwell body model (Emmerich and Korn, 1987).

Before recasting the problem (3.1) in weak form, the following product operators are defined for vectorial and tensorial quantities, respectively

$$\mathbf{a}\cdot\mathbf{b} = \sum_{i=1}^{d} a_i b_i, \qquad \underline{a} : \underline{b} = \sum_{i,j=1}^{d} a_{ij} b_{ij}$$

The SEM does not work directly on the differential wave equation (strong formulation) but requires a weak (variational) form. By multiplying the first equation in (3.1) for an arbitrary weighting function vector $\mathbf{v}$, integrating by parts over the domain Ω, and using Green's formula, the weak form of the elastodynamic problem is obtained (Zienkiewicz and Taylor, 2000). The weak formulation of (3.1) reads: $\forall t \in (0,T]$ find $\mathbf{u} = \mathbf{u}(t) \in \mathbf{V}$ such that

$$\partial_{tt}\int_\Omega \rho\,\mathbf{u}\cdot\mathbf{v}d\Omega + \int_\Omega \underline{\sigma}(\mathbf{u}) : \underline{\varepsilon}(\mathbf{v})d\Omega = \int_{\Gamma_N}\mathbf{t}\cdot\mathbf{v}d\Gamma + \int_{\Gamma_{NR}}\mathbf{t}^*\cdot\mathbf{v}d\Gamma + \int_\Omega \mathbf{f}\cdot\mathbf{v}d\Omega \tag{3.4}$$

The problem is then spatially discretized by introducing a finite dimensional space $\mathbf{V}_\delta$ which is a suitable approximation of $\mathbf{V}$. The semi-discrete approximation of (3.4) reads: $\forall t \in (0,T]$ find $\mathbf{u}_\delta = \mathbf{u}_\delta(t) \in \mathbf{V}_\delta$ such that

$$\partial_{tt} \int_\Omega \rho\, \mathbf{u}_\delta \cdot \mathbf{v} d\Omega + \int_\Omega \underline{\sigma}(\mathbf{u}_\delta) : \underline{\varepsilon}(\mathbf{v}) d\Omega = \int_{\Gamma_N} \mathbf{t} \cdot \mathbf{v} d\Gamma + \int_{\Gamma_{NR}} \mathbf{t}^* \cdot \mathbf{v} d\Gamma + \int_\Omega \mathbf{f} \cdot \mathbf{v} d\Omega \quad (3.5)$$

The mesh process allows to split the domain Ω into a family of non overlapping quadrilaterals (in 2D) or hexahedra (in 3D). There are different types of meshes (Figure 3.4). One of the greatest advantages of SPEED is that it allows to handle non-conforming meshes, by means of the Discontinuous Galerkin (DG) discretization approach, which is introduced below.

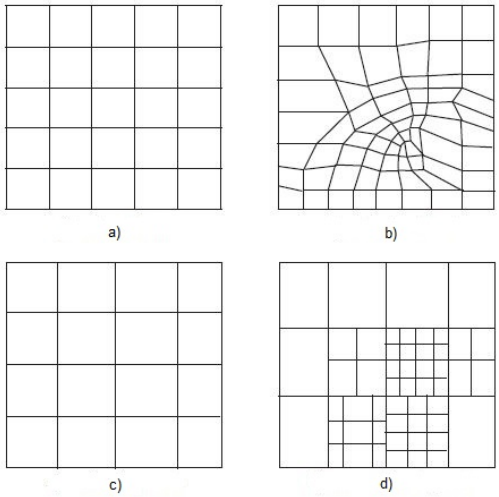

Figure 3.4: Examples of different mesh algorithms: a) structured, b) unstructured, c) conforming and d) non-conforming. [From Smerzini (2010)].

1 Level. On a first level, the domain Ω is partitioned into R non-overlapping polygonal subdomains, that is, $\Omega = \cup_{j=1}^{R} \Omega_j$, with sufficiently smooth boundary $\Gamma_j := \partial\Omega_j$. This decomposition can be geometrically non-conforming, that is, for two adjacent subdomains Ω_k, Ω_i, the surface $\Lambda := \Gamma_k \cap \Gamma_i$ may not be a complete side of either Ω_k or Ω_i (Figure 3.5).

2 Level. For each Ω_k a conforming partitioning τ_k is defined, such that $\Omega_k = \cup_{j=1}^{R_k} \Omega_k^j$. The elements Ω_k^j have tipically linear size h_k, ($h_k = \max_j h_k^j$, with $h_k^j = diam(\Omega_k^j)$) and are obtained by mapping the reference cube $\Omega^* = (-1,1)^3$ with a suitable bilinear map with nonzero Jacobian J_k^j. This second-level partition is geometrically conforming in each Ω_k, thus the intersection

of two elements $\Omega_k^j, \Omega_k^i \in \Omega_k$ for $j \neq i$, is either empty, or a vertex, or an edge, or a face of both Ω_k^j and Ω_k^i.

3 Level. The third level is represented by the so-called LGL points $\mathbf{x}_i$ in each mesh element Ω_k^i (Figure 3.5). On the reference element Ω^*, these points are defined as the tensor product of LGL points defined in the interval [-1,1]. Then they are mapped on the physical element Ω_k^i.

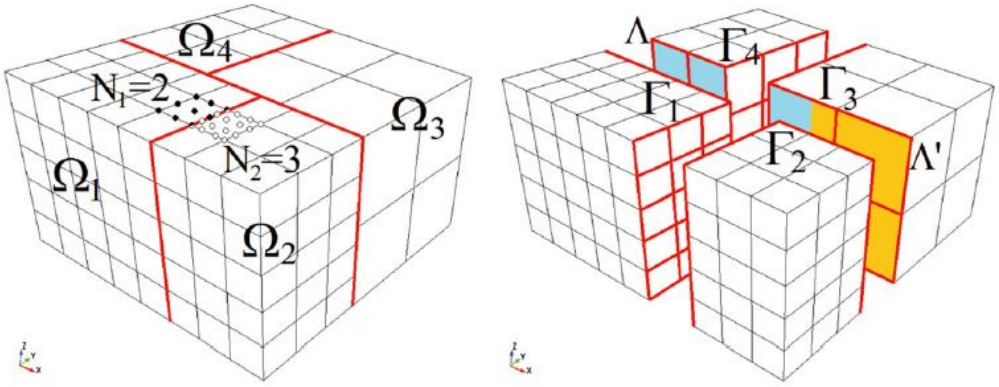

Figure 3.5: 3D example of non-conforming domain decomposition. The whole domain is composed of different non-overlapping polygonal subdomains, made by hexahedral elements. Discontinuous Galerkin discretization allows to deal with a nonuniform polynomial degree distribution (**N**-adaptivity, e.g.,$\mathbf{N}_1 = 2$ in Ω_1 and $N_2 = 3$ in Ω_2), as well as a locally varying mesh size (**h**-adaptivity between subdomains $\Omega_1, \Omega_2, \Omega_3$ and Ω_4). [From Mazzieri et al. (2013)].

At the interfaces between non-conforming subdomains Λ, the continuity of the numerical solution is enforced by treating the jumps of the displacements through a suitable DG algorithm of the interior penalty type (De Basabe et al., 2008).For the details on how to construct the finite dimensional space $\mathbf{V}_\delta$ for the Discontinuous Galerkin spectral element (DGSE) and on the DG weak formulation, the reader may refer to Antonietti et al. (2012).

The integrals appearing in the semi-discrete weak form of the equation of motion (3.5) are evaluated numerically through Legendre-Gauss-Lobatto quadrature formula. After the spatial integration and the algebraic formulation are done, a system of discrete ordinary differential equations for the nodal displacement is obtained. Finally, this system is discretized in time, i.e., the interval $(0, T]$ is subdivided into N subintervals of amplitude $\Delta t = T/N$. Time integration is carried out using the standard leap-frog scheme (Newmark method with $\beta = 0$ and $\vartheta = 1/2$) or by the the explicit fourth-order accurate Runge-Kutta method (Quarteroni et al., 2007).

The time integration scheme is stable if the time step Δt satisfies the

Courant–Friedrichs–Lewy (CFL) condition

$$\Delta t \leq C_{CFL} \frac{\Delta x}{V_P} \tag{3.6}$$

where Δx is the shortest distance between two LGL nodes and C_{CFL} is a constant depending on the dimension, the order of the scheme, the mesh geometry and the polynomial degree. An heuristic rule suggests that C_{CFL} is roughly equal 0,3–0,4 for a deformed and heterogeneous mesh (Komatitsch et al., 2005).

Another constraint on the design of the mesh is the criteria for spatial discretization. The Nyquist theorem provides the maximum spatial sampling step for a proper discretization of the computational grid, based on the minimum number of points to represent the minimum wavelength, equal to 2, so that to avoid aliasing phenomena the minimum requirement is

$$\Delta x < \frac{\lambda_{min}}{2} \tag{3.7}$$

where $\lambda_{min} = V_{min}/f_{max}$, V_{min} is the minimum wave propagation velocity and f_{max} is the maximum resolvable frequency. For the SEM/DGSE Δx is the average inter-node distance and is not constant. As rule of thumb, for a relatively low spectral degree $N \leq 5$, the characteristic dimension Δl of the spectral element is given roughly by the following expression

$$\Delta l \leq \frac{\lambda_{min}}{G_\lambda} N \tag{3.8}$$

where G_λ is the number of points per minimum wavelength and N is the degree of the interpolant polynomial. Faccioli et al. (1997) showed that, for a homogeneous medium, $G_\lambda \geq 2,5$, while in presence of strong material discontinuities, $G_\lambda \geq 4$ is more appropriate.

The fact that SPEED can deal with a non uniform polynomial degree distribution (N-adaptivity), as well as a locally varying mesh size (h-adaptivity), makes mesh design more flexible (since grid elements do not have to match across interfaces) and permits to select the best-fitted discretization parameters in each subregion, while controlling the overall accuracy of the approximation. Moreover, since the DG approach is applied only at a subdomain level, the complexity of the numerical model and the computational cost can be kept under control, avoiding the proliferation of unknowns, a drawback that is typical of classical DG discretizations (Paolucci et al., 2014).

SPEED code is naturally designed for multi-core computers or large clusters, but it can run as well on a single processor machine. It is written

in Fortran90 using its pseudo-object oriented features. It takes advantage of the hybrid parallel programming based upon the Message Passing Interface (MPI) library, relying on the domain decomposition paradigm and the OpenMP library for multithreading operations on shared memory. The mesh generation may be accomplished using a third party software, e.g. CUBIT (http://cubit.sandia.gov/) and load balancing is made easier by graph partitioning based on the METIS library (glaros.dtc.umn.edu/).

3.3 Seismic Source in SPEED

An important issue that has not been discussed is how seismic waves originate and how this process is implemented in SPEED. The objective of this section is to clarify this aspect.

During an earthquake, sliding motion initiates at a point named hypocenter, and a dislocation front expands outward over the fault separating regions that are slipping from regions that have not yet been affected by rupture propagation (Figure 3.6a). The propagation of the rupture front results, thus, in a function of space and time $\Delta u(\underline{x}, t)$ which gives the actual slip vector along the fault plane. Despite the fact that geological faults are geometrical complex 3D multi-scale structures, in almost all applications in geophysics and seismology, a plane-fault approximation is adopted as a reasonable compromise. Fault orientation is described by the strike angle, ϕ_f, the dip angle, δ_f; while the slip direction is given by the rake angle, λ_f, measured in the plane of the fault from the strike direction to the slip vector, as sketched in Figure 3.6b.

3.3.1 Point source

For a seismic source to be of internal origin, two basic conditions have to be satisfied : i) null resultant of the forces and ii) null resultant of the moment. The simplest, but realistic representation of a seismic source is a double-couple, which consists in a pair of couples of forces acting in opposite direction so that the conservation of angular moment is satisfied from a mechanical viewpoint.

The seismic moment tensor provides an effective mathematical representation of a point source. Let us define the force couple M_{ij} in a Cartesian coordinate system as a pair of opposite forces F in the i direction, separated in the j direction by a distance δ_d. The magnitude of any linear dipole is

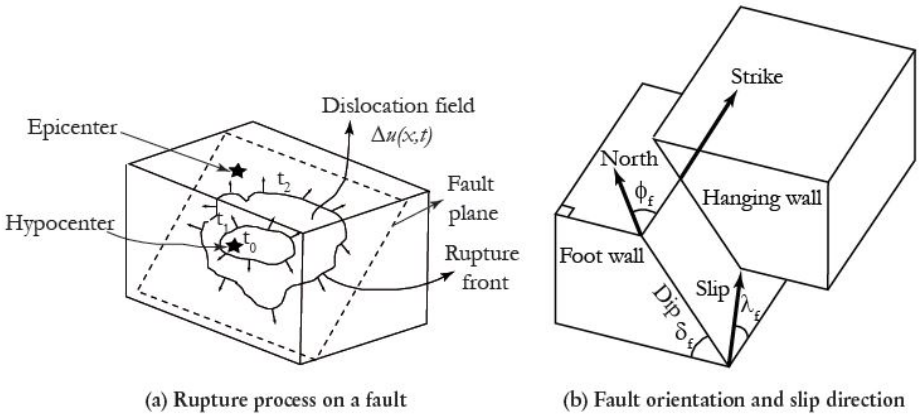

Figure 3.6: a) Schematic diagram of rupture front spreading from the hypocenter over the fault plane. The expansion of the rupture area results in a space and time varying dislocation function $\Delta u(\underline{x}, t)$. b) Definition of conventional parameters used to indicate fault orientation and slip direction. [From Smerzini (2010)].

given by $F\delta_d$ and it is assumed constant as δ_d goes to zero in the limit case of a point source. Making reference to Figure 3.7, it is, thus, natural to define the nine components of the seismic moment tensor $\mathbf{M}$ as follows

$$\mathbf{M} = \begin{bmatrix} M_{xx} & M_{xy} & M_{xz} \\ M_{yx} & M_{yy} & M_{yz} \\ M_{zx} & M_{zy} & M_{zz} \end{bmatrix} \tag{3.9}$$

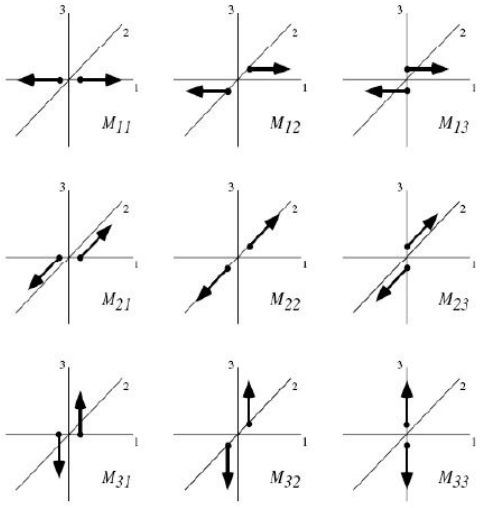

Figure 3.7: The nine different force couples constituting the seismic moment tensor $\mathbf{M}$. [From Aki and Richards (2002)].

Very often in seismology it is assumed that geometry of the source can be separated by its time variation (Madariaga, 2015), so that the seismic

moment tensor can be rewritten as follows

$$\mathbf{M}(\underline{x}, t) = \mathbf{M}(\underline{x})s(t) \tag{3.10}$$

where $\mathbf{M}$ is a time-invariant tensor that describes the geometry and orientation of the source and $s(t)$ is a non dimensional slip source function normalized to unit value. An example of a slip function is depicted in Figure 3.8, where the rise time τ_R quantifies the slip duration.

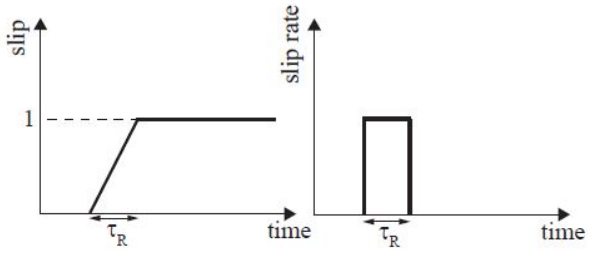

Figure 3.8: Example of slip and slip rate functions: physical meaning of the rise time τ_R. [From Smerzini (2010)].

If fault opening is disregarded, the seismic moment tensor $\mathbf{M}$ equivalent of a fault (Madariaga, 2015), can be expressed as follows

$$M_{ij} = (v_i n_j + v_j n_i) M_0 \tag{3.11}$$

where $\underline{n}$ is the unit normal vector to the fault surface, $\underline{v}$ is the unit slip vector, and M_0 is the scalar seismic moment (Aki, 1966), defined as

$$M_0 = \mu \overline{\Delta u} A \tag{3.12}$$

with μ being the shear modulus of the crustal rock and $\overline{\Delta u}$ the average dislocation on the fault plane with area A.

Another way of representing of a seismic source is by means of the seismic moment tensor density (Aki and Richards, 2002) as follows

$$m_{ij}(\underline{x}, t) = \frac{M_0(\underline{x}, t)}{V}(v_i n_j + v_j n_i) \tag{3.13}$$

where $M_0(\underline{x}, t)$ describes the time history of moment release at the source point $\underline{x}$ inside the elementary volume V, while $\underline{n}$ and $\underline{v}$ have the same meaning explained before.

As demonstrated by Madariaga (2015), m_{ij} is equivalent to a body force distribution with the following expression

$$f_i^{sism} = -\frac{\partial m_{ij}}{\partial x_j} \tag{3.14}$$

Therefore, the equilibrium equation in (3.1) can be modified as follows

$$\rho \frac{\partial^2 u_i}{\partial t^2} = \sigma_{ij,j} - m_{ij,j} \tag{3.15}$$

For the details on the introduction of the seismic moment tensor density into the SEM formulation, please refer to Faccioli et al. (1997).

3.3.2 The Kinematic dislocation model

The point source model just discussed provides a simple approach to the simulation of seismic radiation. It is probably quite sufficient for the purpose of modeling small sources situated sufficiently far from the observer so that the source looks like a single point source. For larger earthquakes, and especially for earthquakes observed at distances close to the source, the point source model is not sufficient, and one has to take into account the geometry of the source and the propagation of rupture across the fault (Madariaga, 2015).

In spite of much recent progress in understanding the dynamics of earthquake ruptures, the most widely used models for interpreting seismic radiation are the so-called dislocation models. In these models, the earthquake is simulated as the kinematic spreading of a displacement discontinuity along a fault plane.

In SPEED, the kinematic description of the seismic source uses the seismic moment tensor density $m_{ij}(\underline{x}, t)$. As presented in Smerzini (2010), the effect of fault finiteness and heterogeneity is accounted for by subdividing an extended fault into a number of subfaults (Figure 3.9). Each subfault k, for $k = 1, ..., L_{sism}$, is characterized by its own seismic moment tensor M_{ij}^k, defined as a function of the following parameters: coseismic displacement Δu^k, subfault area A^k, elastic shear modulus μ^k, unit vector normal to the fault $\underline{n}$, unit slip vector $\underline{v}^k$, rupture velocity V_R^k, rise time τ_R^k associated with the prescribed source time function $s(t)$, and location of the hypocenter $\underline{x}_{hy}$, where seismic rupture nucleates.

The seismic moment release history $M_0(t)$ at each source node $\underline{x}_s^n$ is controlled by the source slip function $s(t)$ and is shifted in time according to the distance from the hypocenter $\underline{x}_{hy}$, as follows

$$M_0^n(t))s(t - \Delta t^n; \tau_R^n)$$

with

$$\Delta t^n = \frac{\mid \underline{x}_{hy} - \underline{x}_s^n \mid}{V_R^n}$$

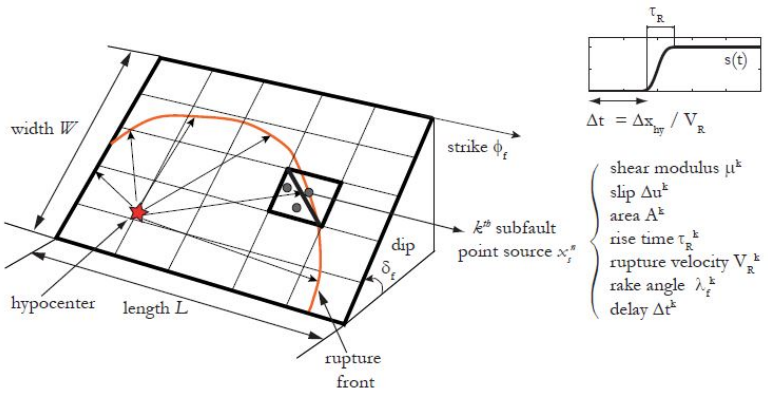

Figure 3.9: Numerical modeling of an extended seismic source. The fault plane is subdivided into a number of subfaults, defined by a set of spectral nodes at locations $\underline{x}_s^n$. Each subsource is characterized by its own parameters. [From Smerzini (2010)].

where V_R^n and τ_R^n are the rupture velocity and rise time, respectively, associated to the n^{th} point source inside the k^{th} subfault.

In this formulation, the only condition to fulfill is that the sum of the scalar seismic moments associated to each subfault is equal to that of the simulated earthquake, that is

$$M_0^{EQ} = \sum_{k=1}^{L_{sism}} M_0^k = \sum_{k=1}^{L_{sism}} \mu^k \Delta u^k A^k \tag{3.16}$$

The code features a number of options for the kinematic modelling of an arbitrarily complex seismic source, by assigning realistic distributions of co-seismic slip along an extended fault plane through ad hoc pre-processing tools. Furthermore, it is also possible to define stochastically correlated random source parameters, in terms of slip pattern, rise time, rupture velocity and rupture velocity distribution along the fault plane, which may be crucial in deterministic simulations to excite high frequency components of ground motion (Smerzini and Villani, 2012). Furthermore, SPEED allows to treat: plane wave load, Neumann surface load and volume force load.

3.4 Construction of the 3D Model for Mexico City

In the previous sections, the importance and usefulness of 3D numerical physics-based simulations have been pointed out, as well as the use of SPEED to carry out such simulations. The aim of this section is to describe the

procedure that was followed to set up the 3D numerical model for Mexico City to be used as input in SPEED. The information needed to create the model is the following

- Topography model
- Geological and geotechnical characterization
- Crustal model for the rock materials
- Characterization of the seismic source (which will be commented in the next section)

The first step was to obtain the 3D computer graphics representation of the ground topography for the Mexico basin area, i.e., the Digital Elevation Model (DEM). This information was obtained from the Mexican National Institute of Statistics, Geography and Informatics[4] (INEGI). Since surfaces are needed for the mesh creation process, the DEM was first converted into a *cloud of points* using the free open source software QGIS[5]. Then, the cloud of points was imported in the commercial computer-aided design software Rhinoceros[6], which handles geometries based on the NURBS mathematical model. In Rhinoceros, a mesh was created from the cloud of points using the command *MeshPatch*, and finally the mesh was converted into a surface with the function *Drape*.

The second step was to define the geometry of the clay and the deep deposits. The lower boundary for the clay deposits proposed by Juárez-Camarena et al. (2016) was adopted (Figure 2.12), while for the deep deposits that proposed by Cruz-Atienza et al. (2016) was used (Figure 2.13). Both models have been introduced in section 2.4.1. Once again they had to be converted into surfaces, which was done in a two-step process

1. Georeferencing and digitization of depth contours in Figures 2.12 and 2.13 using QGIS. The digitized contours of the deep deposits in QGIS are shown over the DEM of the Mexico basin in Figure 3.10.
2. Once digitized, the contours were imported in Rhinoceros, where first they were projected onto the topography surface, and then displaced in the vertical direction by their corresponding value. Finally, the contours were fitted by a surface using the command *Patch*. For illustrative purposes, the surface for the lower boundary of the clay deposits is shown in Figure 3.11 (with a vertical exaggeration x30).

[4] www.inegi.org.mx/app/geo2/elevacionesmex
[5] qgis.org/en/site
[6] www.rhino3d.com

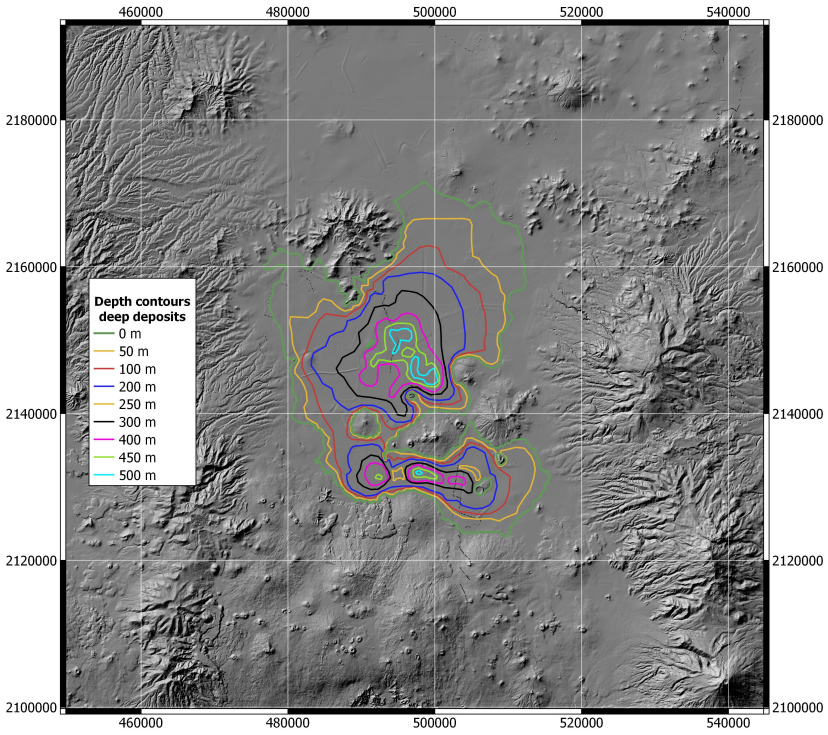

Figure 3.10: Digitized depth contours of the deep deposits in QGIS, shown over the DEM of the Mexico basin.

Regarding the crustal structure surrounding the basin, a 1D model determined from the inversion of receiver functions at the CU site (Cruz-Atienza et al., 2010) was adopted. This model includes a relatively low-velocity layer on top, associated with the ∼2 km thick TMVB (Oligocene volcanics) (Cruz-Atienza et al., 2016). The mechanical properties of the considered horizontal layers are presented in Table 3.1. The values of thickness H are measured from the center of the basin. Poisson's ratio ν is ~ 0.275.

Quality factors Q_s for the crustal materials are taken equal to $V_S/10$, which is in accordance to typical values considered in literature (e.g., Paolucci et al., 2015; Cruz-Atienza et al., 2016), while Q_p is considered as $2 \cdot Q_s$.

Table 3.1: Crustal model.

Layer	H [km]	V_S [m/s]	V_P [m/s]	ρ [kg/m^3]	Q_s	Q_p
1	2.0	1550	2782	2200	155	310
2	2.3	3150	5624	2530	315	630
3	6	3500	6283	2700	350	700

However, at some parts of the city, on top of the Oligocene volcanics are found a hundred meters or so of tuffs (e.g., site TACY) or sands, gravel,

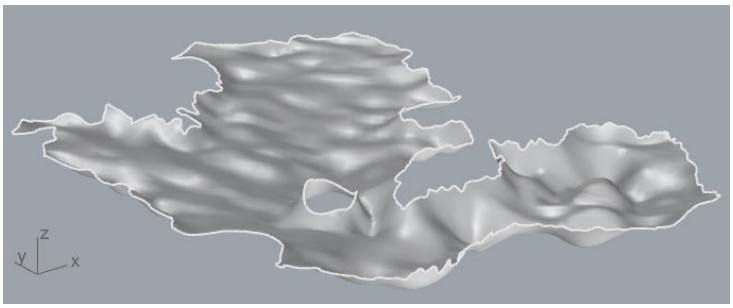

Figure 3.11: Vertically exaggerated (x30) surface for the lower boundary of the clay deposits.

and recent lava flows (e.g., site CUP5) (Singh et al., 1995). Considering the V_S profile below CU shown in Figure 3.12, after the calibration presented in Section 3.6, a V_S=750 m/s was adopted for the first 200 m of the crustal structure. Q_s=100 was assumed, while Q_p was considered as $2 \cdot Q_s$.

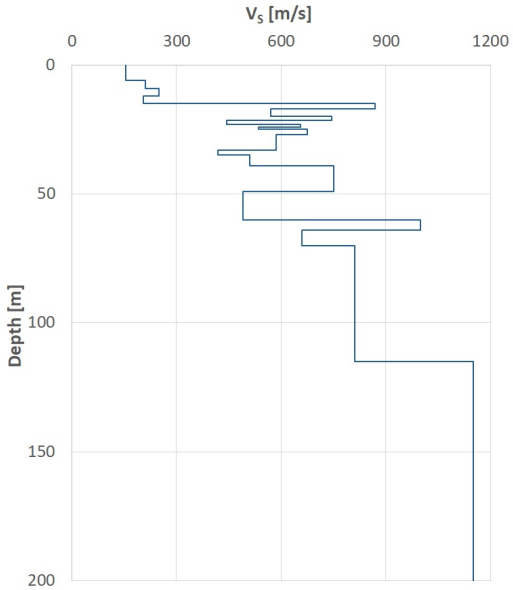

Figure 3.12: Shear-wave velocity V_S as a function of depth below CUP5 (hill zone). [Adapted from Singh et al. (1995)].

The variation of shear wave velocity with depth for the clay was defined based on the experimental results presented in Figure 2.16 (Jaime, 1987). In order to account for the increase in V_S (due to regional subsidence) since the date in which the tests were carried out, V_S values in Figure 2.16 were increased by a 15%, which is in accordance with the increase in G_{max} estimated by Ovando-Shelley et al. (2007). For every location (x_i, y_i), it was considered a linear variation of V_S from 70 m/s at the ground surface to 100 m/s at the

contact with the deep deposits. Hence

$$V_S(x_i, y_i, z) = 70 \cdot \frac{100 - 70}{H_i} \qquad [m/s] \tag{3.17}$$

where z is the depth from the ground surface (in meters), and H_i is the thickness of the clay deposits (in meters) at location (x_i, y_i), computed as $H_i = z_{ground}(x_i, y_i) - z_{deep\,deposits}(x_i, y_i)$. For instance, for sites CUPJ and SCT, where the deep deposits are found at ∼38 m depth, the assumed V_S profile will be the dashed line in Figure 3.13.

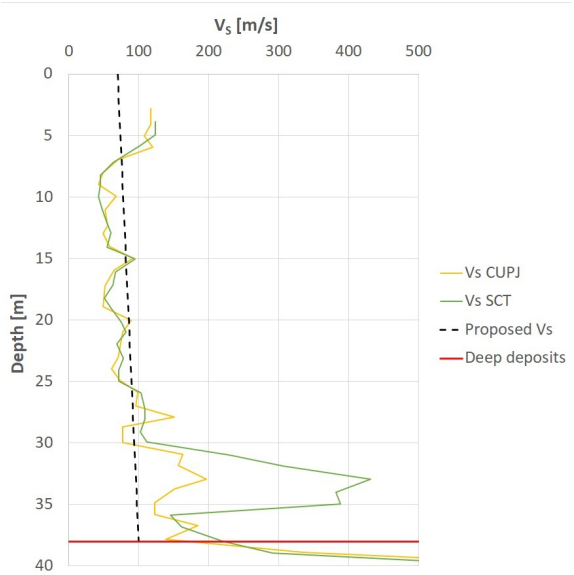

Figure 3.13: Assumed clay V_S profiles for CUPJ and SCT sites.

For the compressional wave velocity, Jaime (1987) reported values of V_P in the range of 1000-1600 m/s, obtained from P-S suspension logging tests carried out at various sites in the lake zone. From seismic refraction tests, Jongmans et al. (1996) reported V_P increasing from 500 m/s at the surface, to 1600 m/s at 40 m depth. Likewise, Pérez-Cruz (1988) measured V_P in the range 880-1550 m/s from seismic reflection tests. Here, P-wave velocity for the clay is adopted as $V_P = 13 \cdot V_S$, which corresponds to a very high value of Poisson's ratio of ~ 0.4975, that is common for the dynamic response of Mexico City clays (Jaime, 1987).

Regarding the density ρ of the clay, also a linear variation was assumed from 1300 kg/m^3 at the ground surface to 1600 kg/m^3 at the contact with the deep deposits.

For the Mexico City clays, the use of a visco-elastic model is considered to be adequate since due to their high plasticity index, they exhibit no sig-

nificant reduction in shear modulus even for shear strains as high as 0,1% (after Romo et al., 1988). Considering that Q_s for the clay is in the range of 10-50, according to laboratory (Romo and Ovando-Shelley, 1996) and field measurements (Jongmans et al., 1996), two damping models are considered:

1. Viscous damping model with frequency proportional Q factor with values $Q_s = V_S/3$, and reference frequency f_0=0.9 Hz.
2. Hysteretic damping model with $Q_s = V_S/2$.

For both cases Q_p is considered as $2 \cdot Q_s$.

It was mentioned in section 2.4.1 that at the top of the clay deposits there is a layer made of artificial fills and that within the clay there is a thin layer of a very dense sandy silt (Figure 2.11). However, since the thickness of these layers is « than the minimum wavelength to be propagated (for the frequency range considered), these layers are not considered. Indeed, Chávez-García and Bard (1994) shows that the presence at the surface of an irregular resistant layer does not contribute much to ground motion.

As to the deep deposits, V_S is defined as $V_S = 500 + 9.6 \cdot z^{0.6}$, while V_P is computed as $V_P = 1500 + 19.2 \cdot z^{0.6}$, based on the available information, which is scarce, mainly consisting of geophysical studies (e.g., Marsal and Graue, 1969; Pérez-Cruz, 1988; Martínez-Robledo, 2019). Profiles of V_S and V_P for the deep sediments are shown in Figure 3.14. The density was assumed constant with a value of ρ=1900 kg/m^3, while $Q_s = V_S/7$ and $Q_p = 2 \cdot Q_s$.

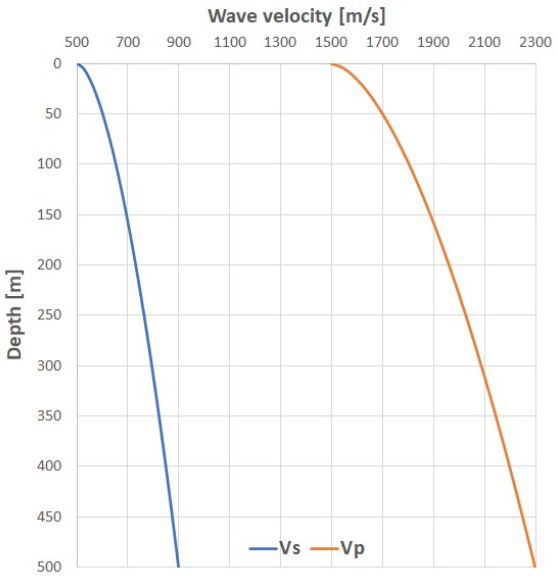

Figure 3.14: Variation with depth of V_S and V_P for the deep deposits.

Due to the high impedance contrast between the basin and the surrounding hill zone, initially a discontinuous mesh was constructed (Figure 3.15), with the idea of exploit the capability of SPEED to handle a non uniform polynomial degree distribution, as well as a locally varying mesh size, by means of the Discontinuous Galerkin formulation. However, the available walltime for one simulation (24 h) was not enough to finish the set up phase of the simulation. Therefore, the confirming mesh described in the next paragraph was employed.

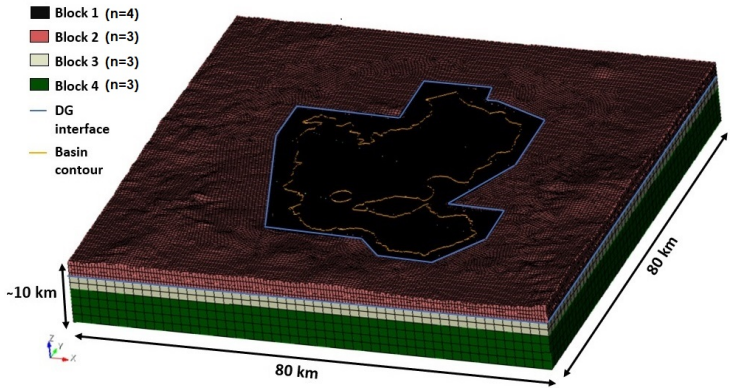

Figure 3.15: Initially created discontinuous mesh for the Mexico City area.

Once all the mechanical parameters have been defined, the mesh is designed keeping in mind condition (3.8) that defines the maximum spectral element size as a function of V_S, N (degree of the interpolant polynomial) and f_{max} (maximum frequency to be propagated), which was limited to 1 Hz in order to avoid computational overburden. The mesh was created using the software CUBIT[7], it extends over a volume of about 60 x 60 x 10 km^3 and is discretized using an unstructured hexahedral conforming mesh. The basin, i.e., clay and deep deposits, is modeled using the not-honoring technique, for which SPEED evaluates whether or not a node is located within the basin, and assigns to it properties of the basin material in case it does, or the properties of the first crustal layer otherwise. The basin lies within the mesh block 1, which has an area of ∼1649 km^2 and 450 m height, and characteristic element size Δl of 100 m. The rest of the first crustal layer (block 2) is meshed with Δl of ∼300 m, and at the contact with the crustal layer 2 (block 3), the element size is increased to ∼900 m. Crustal layer 2 has Δl going from ∼900 to ∼2700 m, which is the characteristic element size of the crustal layer 3 (block 4). The configuration of the mesh, which consists of 2'446'082 spectral elements, resulting in approximately 308.7x10^6 of total

[7] cubit.sandia.gov

degrees of freedom, is summarized in Figure 3.16.

Material	Block	V_S [m/s]	N	Δl [m]	No. elements	∼No. LGL nodes
Basin	1	70-100	5	100	1'229'094	$153.6x10^6$
Crustal 1	2	750-1550	5	300	1'203'452	$153.4x10^6$
Crustal 2	3	3150	5	900-2700	12'408	$1.55x10^6$
Crustal 3	4	3500	5	2700	1'128	$0.15x10^6$

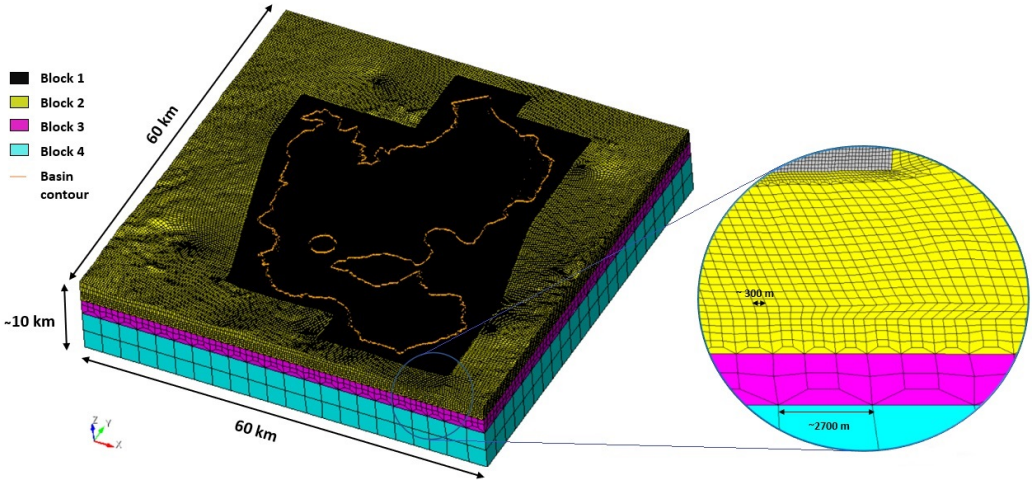

Figure 3.16: 3D mesh for the Mexico City area consisting of 2'446'082 spectral elements with N=5.

3.5 Validation case study: Mw3.0 July 17, 2019 earthquake

The simulated case is the largest event of the earthquake swarm activity, which occurred between July 12 and July 18, 2019, in the borough Miguel Hidalgo, at the western part of Mexico City. SSN (2019) reported 20 events during that week with magnitudes in the range 2.0-3.0. The largest event of the sequence, an Mw3.0 earthquake ($M_0 = 3,98x10^{13}\ N-m$), took place at 03:59 h (22:59 h local time) on July 17, with epicenter at 19.406°N latitude and 99.214°W longitude and depth of 2 km, as reported by SSN (2019). The sequence was recorded by several stations operated by different Institutions (SSN, IINGEN and CIRES). Figure 3.17 shows the epicenter for the Mw3.0 earthquake, as well as the closest stations that recorded the event with their corresponding PGA triplets (NS, EW, Z components).

Despite the magnitude of the 17/07/2019 earthquake was low, it caused panic in the city and produced PGA exceeding 0.3g at the closest station, MHVM, which is the largest ever recorded at a hill-zone site in the Valley of Mexico (Singh et al., 2020). In Figure 3.18 are presented the NS, EW

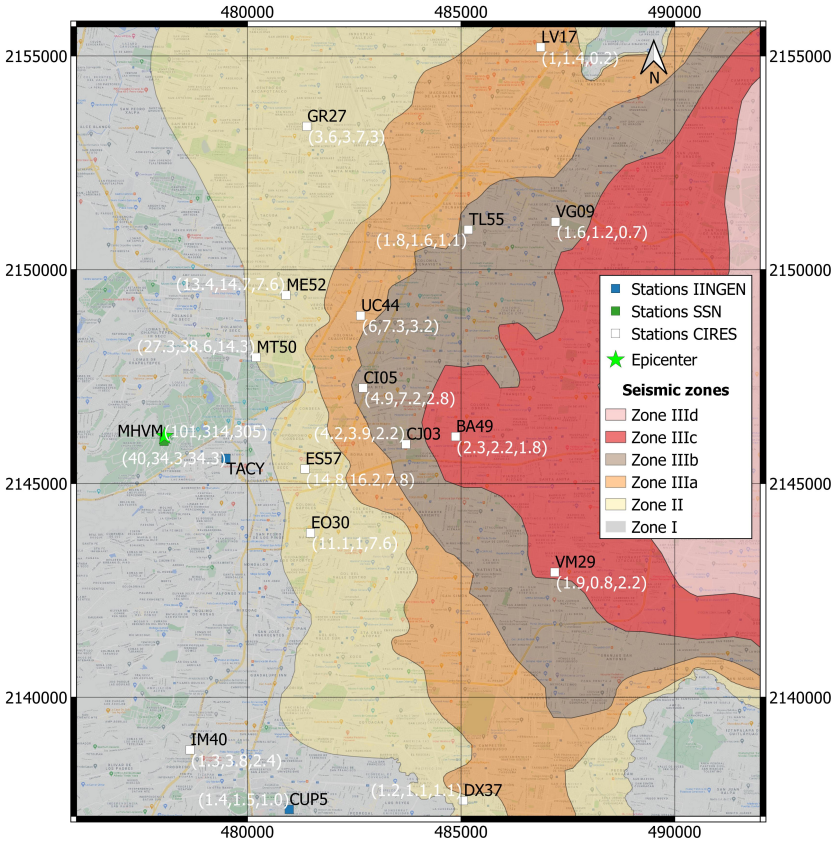

Figure 3.17: Ground motion stations active during the 17/07/2019 Mw3.0 earthquake. Values in white color represent the PGA for the NS, EW and Z components (in cm/s^2) for the corresponding station. The red star represents the epicenter of the event.

and Z components of acceleration at station MHVM for this event. Singh et al. (2020) have suggested that the high PGA resulted from high-frequency amplification at MHVM (about factor of ∼6 around 13 Hz), likely due to topographic site effects.

The main reasons to take this earthquake as study case is because of the good recording coverage that makes possible the verification of the results and calibration of the numerical model, and that its proximity to the Mexico City basin allows to have a model with reduced dimensions.

The focal mechanism for this event (Figure 3.19) was obtained by SSN (2019) from the polarities of the first arrivals. It shows a normal faulting with striking $\varphi = 259°$, dip angle $\delta = 70°$, and $\lambda = -89°$.

A different solution for the focal mechanism was obtained bySingh et al. (2020). Their moment tensor inversion of band-pass filtered (0.08 – 0.2 Hz) displacement traces yields $M_0 = 8x10^{13}\ N - m$ (Mw3.2) and a normal-

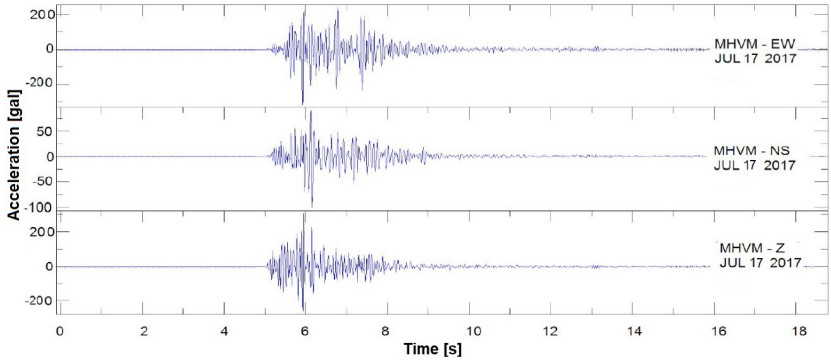

Figure 3.18: Vertical, north–south and east-west accelerograms, recorded at MHVM station during the 17/07/2019 Mw3.0 earthquake. [From SSN (2019)].

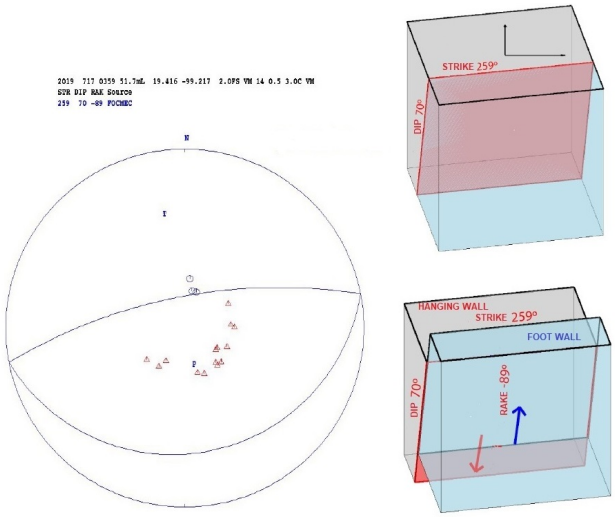

Figure 3.19: Focal mechanism for the 17/07/2019 Mw3.0 earthquake. [From SSN (2019)].

faulting event with NP1: $\varphi = 228°$, $\delta = 80°$, and $\lambda = -97°$, and NP2: $\varphi = 82°$, $\delta = 12°$, and $\lambda = -57°$. They considered NP1 as the fault plane since NE-SW strike of the fault agrees with mapped faults in the area (Figure 2.5).

3.6 Calibration with hill zone records

A calibration process was carried out in order to define three important parameters to be used in the 3D simulation with SPEED: (1) focal mechanism for the July 17, 2019 earthquake; (2) its slip velocity function; and (3) the V_S for the shallowest part of the crustal model. This was accomplished following a trial-and-error procedure to improve the agreement of synthetics with records by changing the different parameters.

Synthetics were computed using the Hisada method based on the analytical integration of Green's functions (Hisada and Bielak, 2003), assuming a horizontally layered model based on the parameters presented in Table 3.1 and the V_S profile of Figure 3.12. The July 17, 2019 earthquake was introduced as a point source, considering that this approximation is generally valid for distances much larger than the size of the fault, which is very small.

In the previous section two focal mechanism were presented for the July 17, 2019 earthquake. With the calibration process, a better agreement with records was obtained using the focal mechanism estimated by Singh et al. (2020), i.e., Mw3.2, $\varphi = 228°$, $\delta = 80°$, and $\lambda = -97°$.

Regarding the slip velocity function, two possibilities were evaluated (Figure 3.20), a box function and an exponential one:

$$Box \;\; s(t) = \begin{cases} 1/\tau, & 0 \leq t \leq \tau \\ 0, & \tau < t \end{cases} \tag{3.18}$$

$$Exponential \;\; s(t) = t \cdot exp(-t/\tau)/\tau^2 \tag{3.19}$$

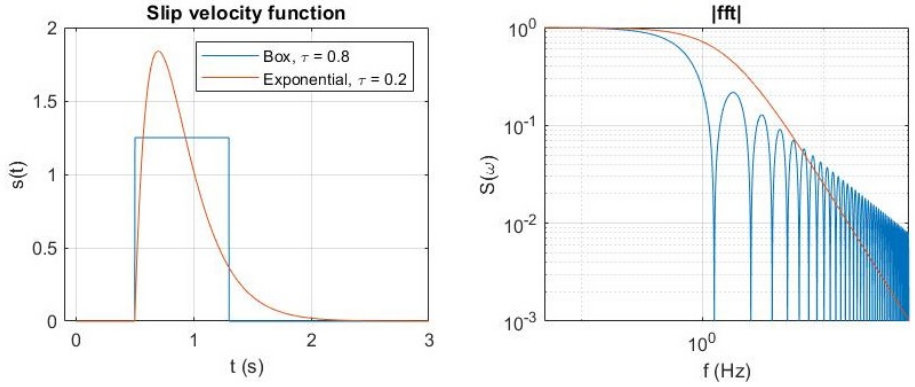

Figure 3.20: Evaluated slip velocity functions for the seismic source.

The parameter τ for both cases was chosen in such a way that the Fourier transform of the slip velocity functions presented an approximate flat portion up to around 0.8 Hz, which is in accordance to the source spectrum computed by Singh et al. (2020) for this event. The exponential function was found to be better suited.

Finally, different V_S profiles for the shallowest part of the crustal model were evaluated. As depicted in Figure 3.21, using V_S=750 m/s for the first 200 m there was a good agreement between synthetics and records, both in amplitude and polarities of first arrivals, for stations MHVM, TACY and CUP5, all of them in the hill zone of Mexico City.

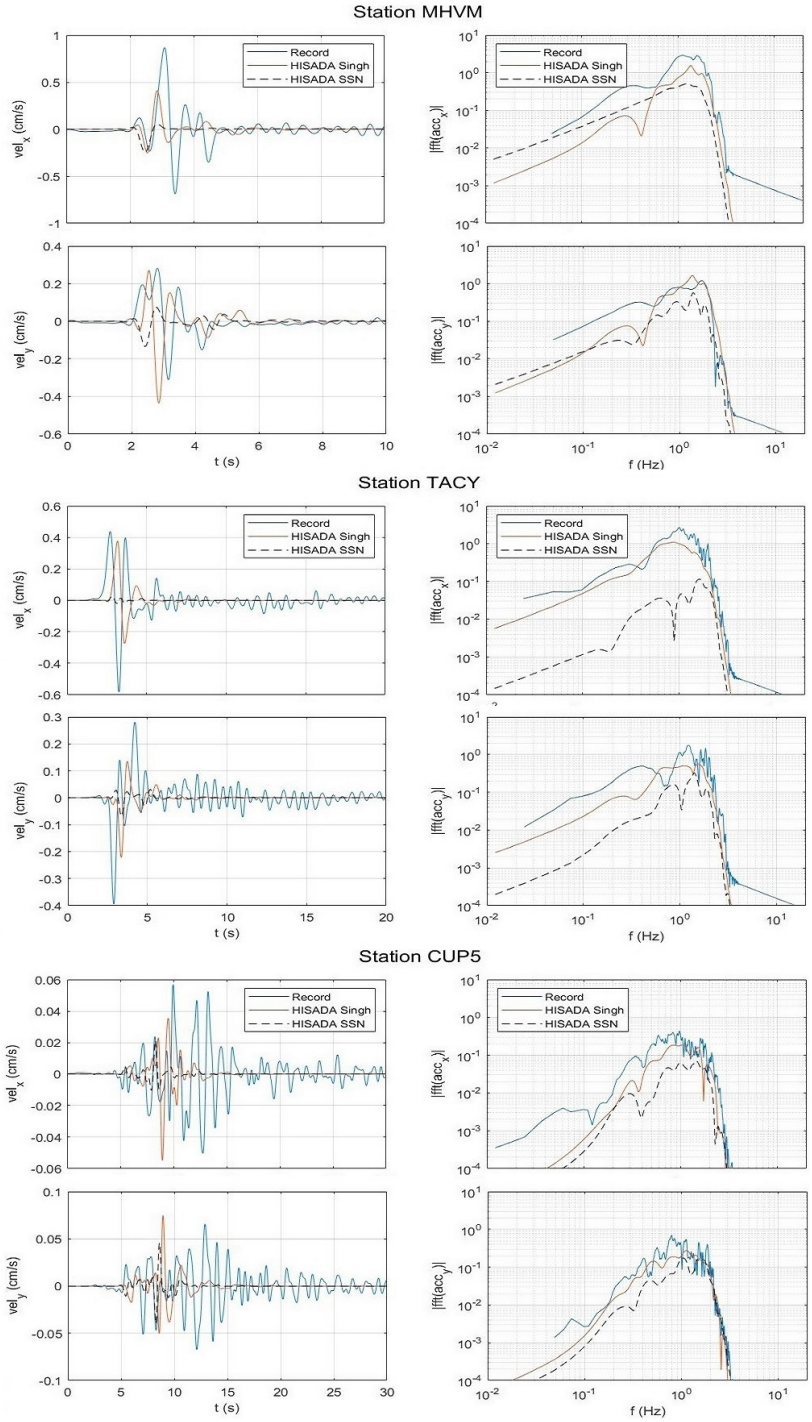

Figure 3.21: Comparison between synthetics (computed with the Hisada method) and records, for stations MHVM, TACY and CUP5. On the left side velocity traces are shown (low-pass filtered at 2 Hz), while on the right side FAS of accelerations are presented. The crustal model in Table 3.1 was used, taking V_S=750 m/s for the first 200 m. The good agreement using the focal mechanism estimated by Singh et al. (2020) is evident.

Chapter 4

Analysis of results

In this chapter the results of two simulations carried out with SPEED are presented. Two damping models for the clay deposits were evaluated as described in Section 3.4, viscous and hysteretic. Hereafter the simulation with viscous damping will be identified by the code 3D-Qv, while the simulation with hysteretic damping will be referred as 3D-Qh. The total observation time for the simulation 3D-Qv was 32 seconds, while for the case 3D-Qh it was 25 seconds. Simulations were performed on the Marconi100 cluster located at CINECA, Italy[1], with a walltime of 96 hours on 512 cores. For each simulation, a time step Δt=0.0002s was chosen for the time marching scheme, which is around 21% of the CFL condition.

It was previously mentioned that the mesh was designed to propagated frequencies up to 1 Hz (in the lake zone) considering condition (3.8), however, that condition is not a strict limit, it is a rule of thumb. Considering the comparison in Figure 4.1 of simulated (from simulation 3D-Qv) and recorded Fourier spectra of acceleration at some stations in the lake zone, it is evident that even at frequencies higher than 1 Hz the numerical results are still valid. The numerical mesh is considered to be able to propagate frequencies up to 1.3 Hz, hence, an acausal Butterworth low-pass filter of fourth order and cut-off frequency f_n=1.3 Hz will be applied to the results presented hereafter.

4.1 Results for case 3D-Qv

In this section the results of the simulation 3D-Qv (frequency proportional Q factor) are presented. Velocity snapshots for the E-W component are shown in Figure 4.2, from which amplification, diffraction and generation of surface waves at the basin edges are clearly observed. Trains of waves traveling at different speeds are also evident. Furthermore, topographic scattering is clearly seen near Cerro de la Estrella. Animations of

[1] www.hpc.cineca.it/hardware/marconi100

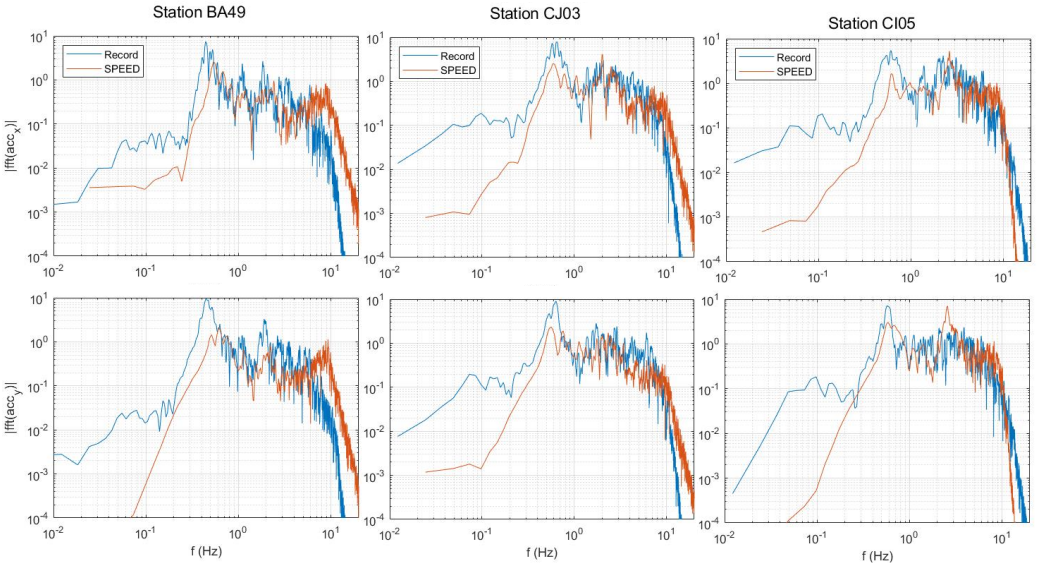

Figure 4.1: Comparison between computed (from simulation 3D-Qv) and recorded FAS of acceleration at some stations in the lake zone. From this results it is considered that the mesh is able to propagate frequencies up to 1.3 Hz.

velocity fields are available in `https://drive.google.com/drive/folders/1jDtSUVRQjC6_EJihRUBxH7VE-VpZXeoh?usp=sharing`.

Figure 4.3 shows the spatial distribution of the geometric mean of the horizontal components (gmh) of Peak Ground Acceleration (PGA). Accelerations of comparable magnitude were obtained in the vicinity of the epicenter and inside the basin.

Figure 4.4 shows maps of Peak Ground Velocity (PGV) for components E-W, N-S, Up-Down (U-D) and gmh, with superimposed velocity traces extracted at some stations. When comparing the velocity traces of station CJ03 (lake zone) with those of TACY and CUP5 (hill zone), the most evident difference is the long duration of the ground shaking in the lake zone. In the near field of the seismic point source, a two-lobed radiation pattern is evident from the PGV maps. The ability of the code SPEED in quantifying the spatial variability of ground motion at large period T has been widely proven in other studies (e.g., Smerzini, 2010; Paolucci et al., 2015). Improved results are obtained in terms of spatial variability of ground motion owing to a more accurate characterization of the seismic wavefield on a wide scale, including all the factors that affect seismic motion from the source to the site (i.e. azimuthal variability of ground motions due to details of fault rupture process, focal mechanism, directivity effects, topographic effects, and 3D site effects), which cannot be take into account by GMPEs (Infantino, 2016).

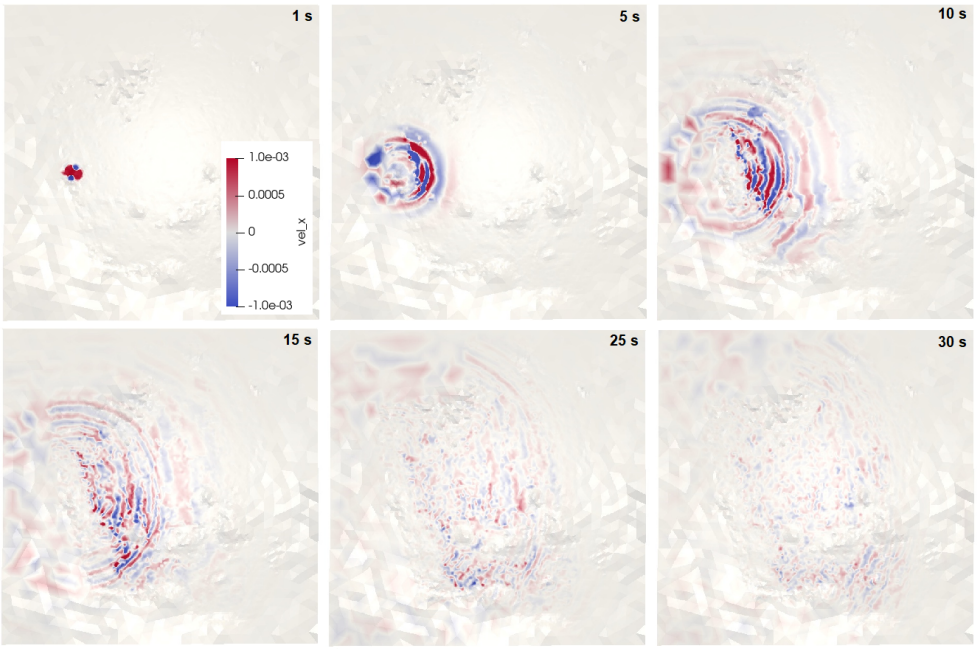

Figure 4.2: Snapshots of velocity (E-W component) from simulation 3D-Qv. Amplification, diffraction and generation of surface waves at the basin edges are clearly observed.

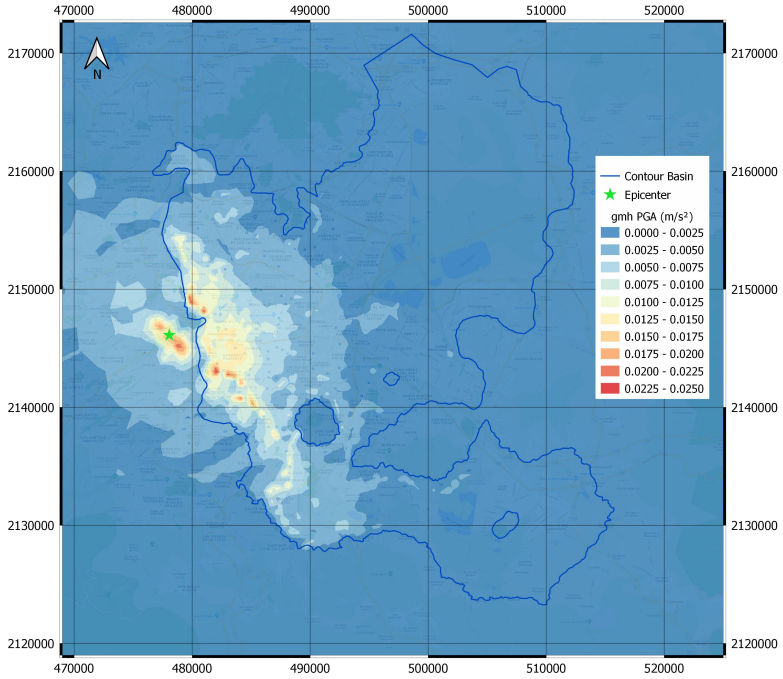

Figure 4.3: Spatial distribution of the geometric mean of the horizontal components (gmh) of PGA from simulation 3D-Qv.

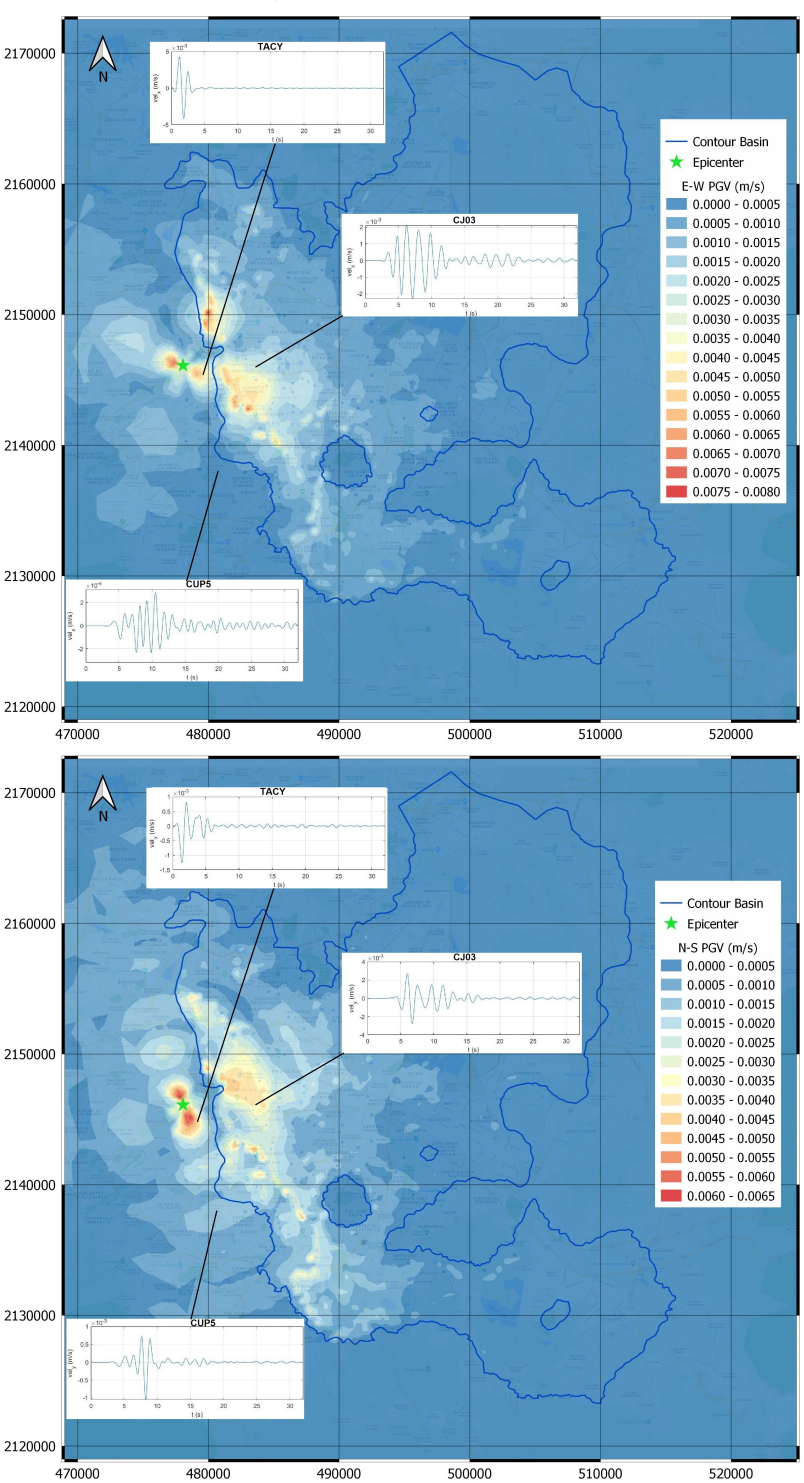

Figure 4.4: Spatial distribution of PGV from simulation 3D-Qv for components E-W and N-S, with superimposed velocity traces extracted at some stations. A two-lobed radiation pattern is evident.

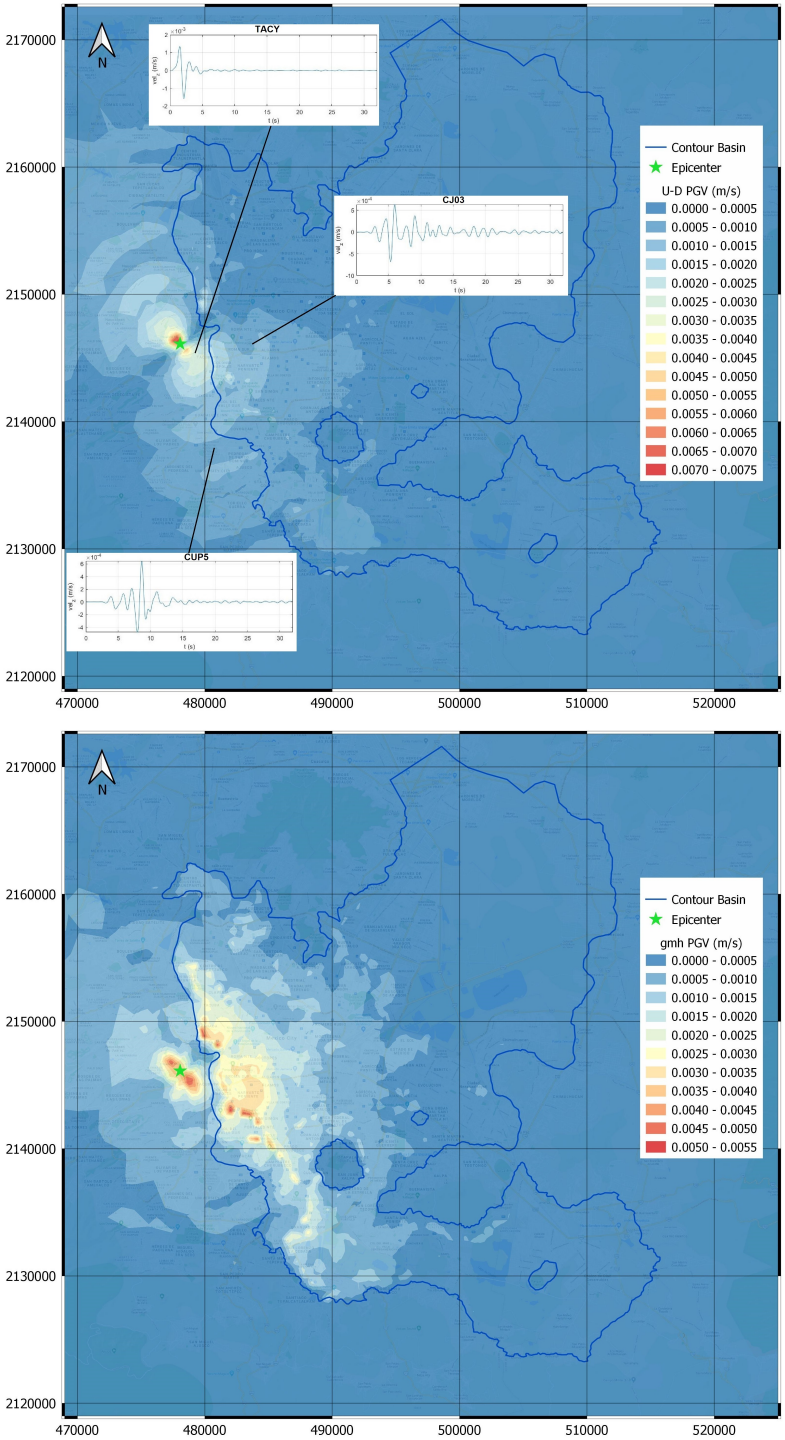

Figure 4.4: Spatial distribution of PGV from simulation 3D-Qv for components U-D and gmh, with superimposed velocity traces extracted at some stations. A two-lobed radiation pattern is evident (continued).

Another important outcome from physics-based simulations for seismic risk analyses are spectral accelerations. In Figure 4.5 are presented the maps of pseudo-acceleration response spectra (SA) at periods (T) 0.5, 1.0, 1.5 and 2.5 s. The highest spectral accelerations were obtained for a period equal to 1.5 Hz, which is similar to the natural vibration period of the eastern part of the lake zone.

4.1.1 Comparison with records

In Figures 4.6 (hill and transition zones) and 4.7 (lake zone), records and synthetics are compared in time and frequency domain. Both numerical results and records have been low-pass filtered at 1.3 Hz, for consistency with the spatial resolution of the numerical mesh. It is clear that for the hill and transition zones, in general terms there was a good agreement between synthetics and records. However, for station MT50 there was a clear under-prediction for the amplitude of the ground motion. The reason for this difference will be tackled later on.

The overall performance of the numerical simulations was quantitatively estimated through the Goodness-of-Fit (GoF) criteria proposed by (Anderson, 2004), considering only the peak parameters of ground motion, of interest for earthquake risk applications, namely: PGA, PGV, Peak Ground Displacement (PGD) and Spectral accelerations (Sa) at periods T = 0.5, 1, 1.5, ans 2 s. GoF score is computed as follows

$$GoF(p_1, p_2) = 10 \cdot exp\left(-\left[\frac{(p_1 - p_2)}{min(p_1, p_2)}\right]^2\right) \tag{4.1}$$

where p_1 and p_2 are the simulated and recorded ground motion parameters in consideration. GoF scores have a range from 0-10, and their interpretation is the following: $<$4, poor fit; 4–6, fair; 6–8, good; and 8, excellent.

Following Paolucci et al. (2015), final GoF scores were computed as a weighted average of the selected metrics, adopting a standard equal weighting for all the metrics under consideration. The GoF scores for the geometric mean of horizontal components, computed for each criteria, are shown in Figure 4.8 for the same subset of 14 stations considered in Figures 4.6 and 4.7.

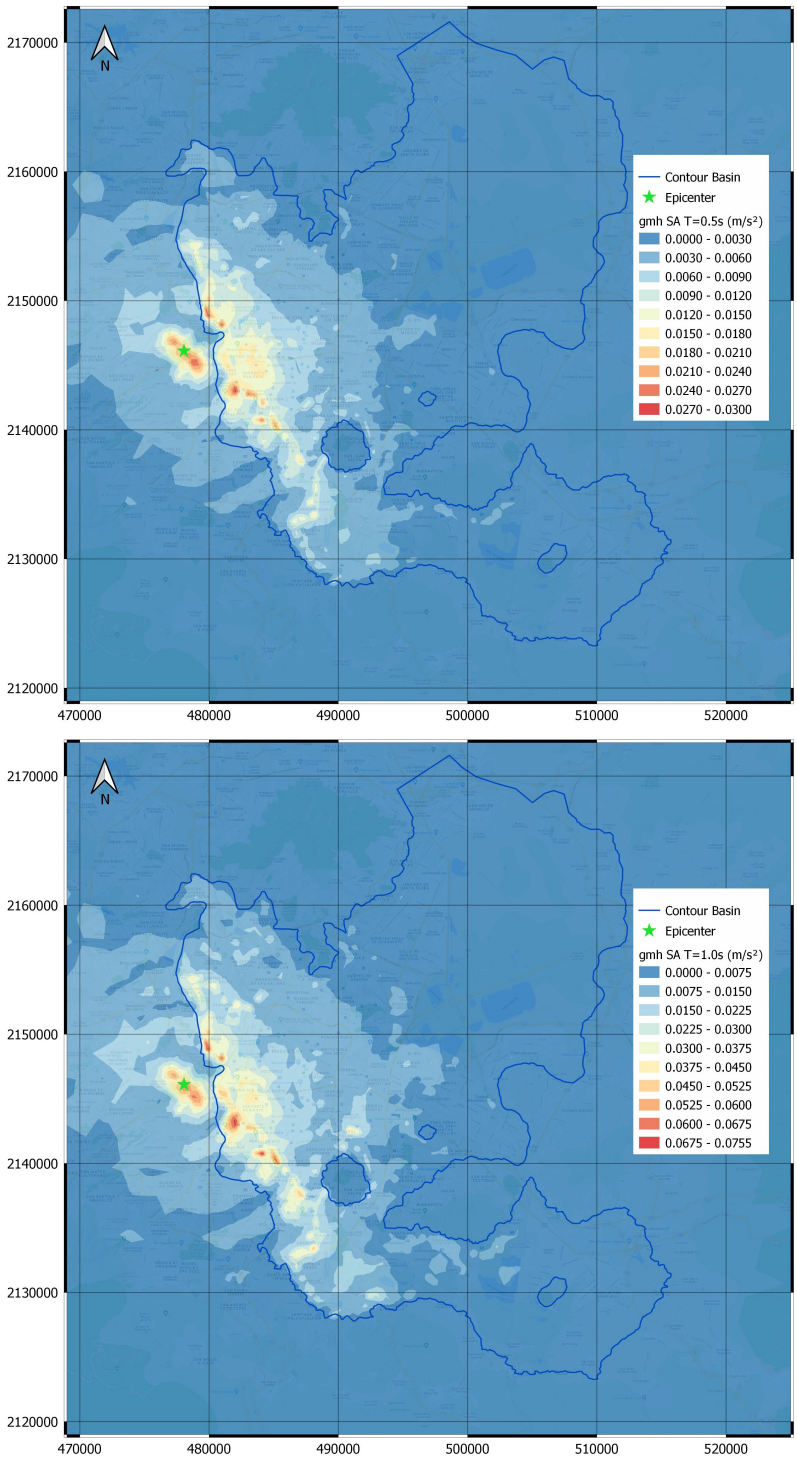

Figure 4.5: Spatial distribution of the gmh spectral acceleration (Sa) at T=0.5 s and 1 s, from simulation 3D-Qv.

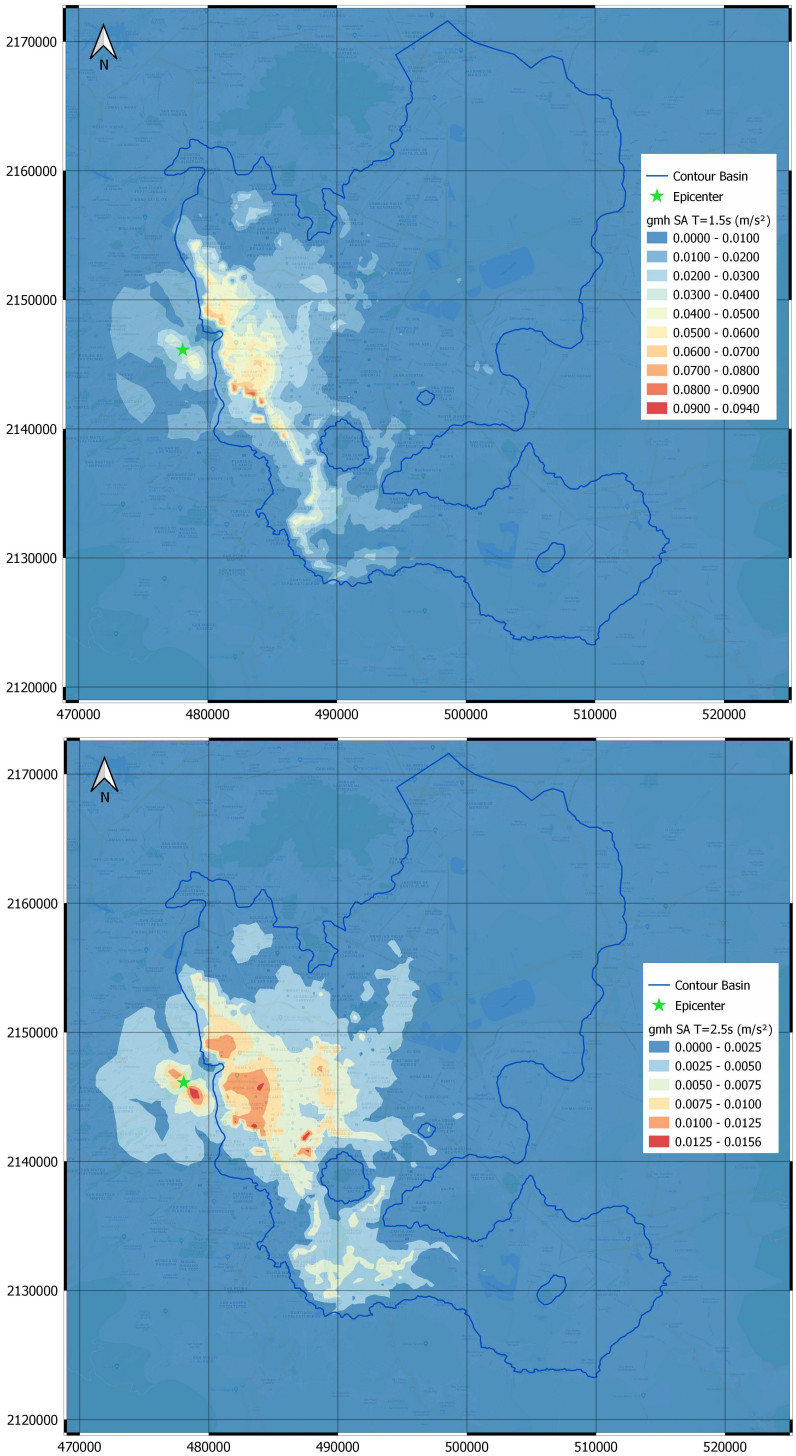

Figure 4.5: Spatial distribution of the gmh spectral acceleration (Sa) at T=1.5 s and 2.5 s, from simulation 3D-Qv(continued).

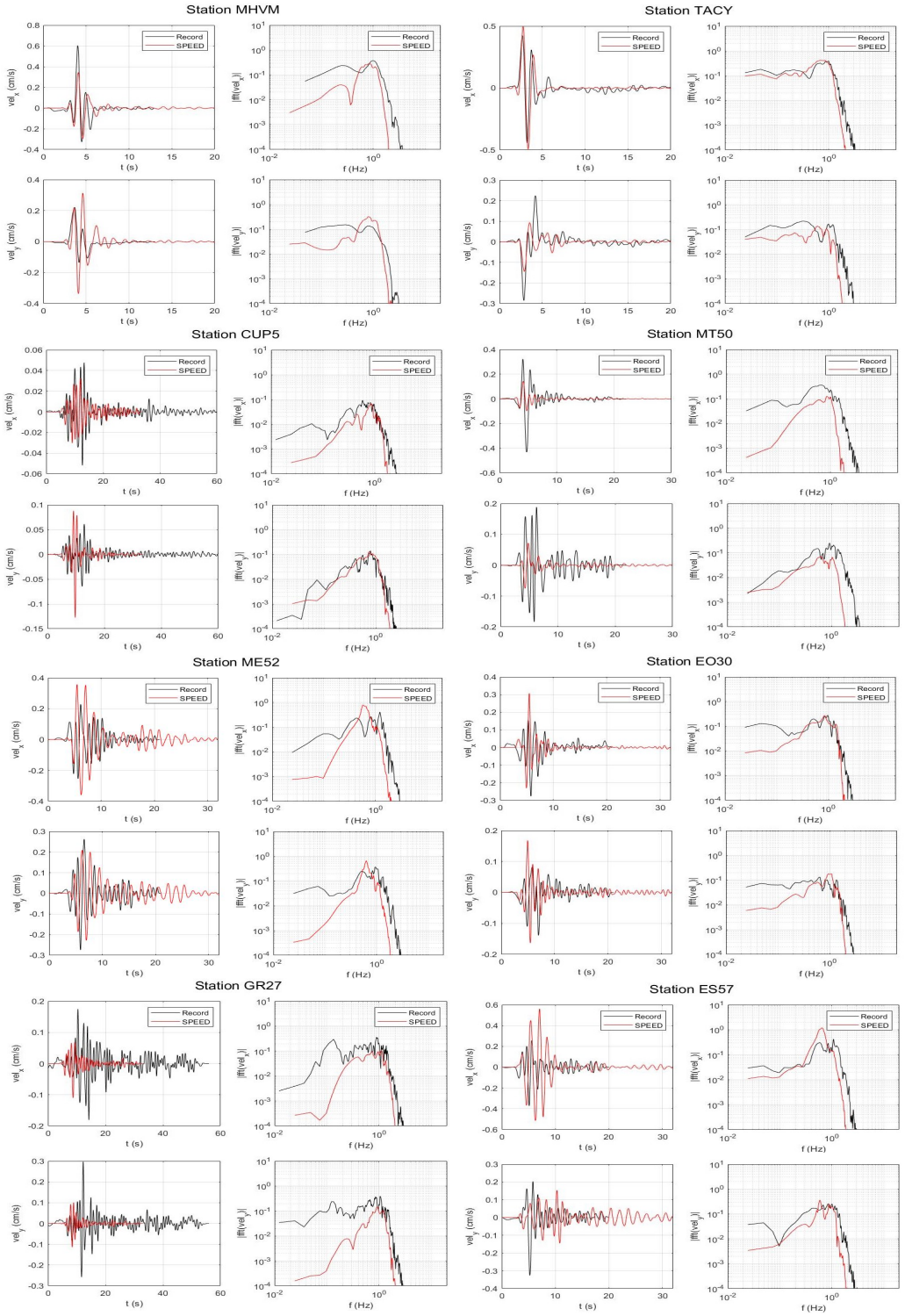

Figure 4.6: Comparison between computed (from simulation 3D-Qv) and recorded velocity time-histories and their corresponding FAS, at some stations in the hill and transition zones.

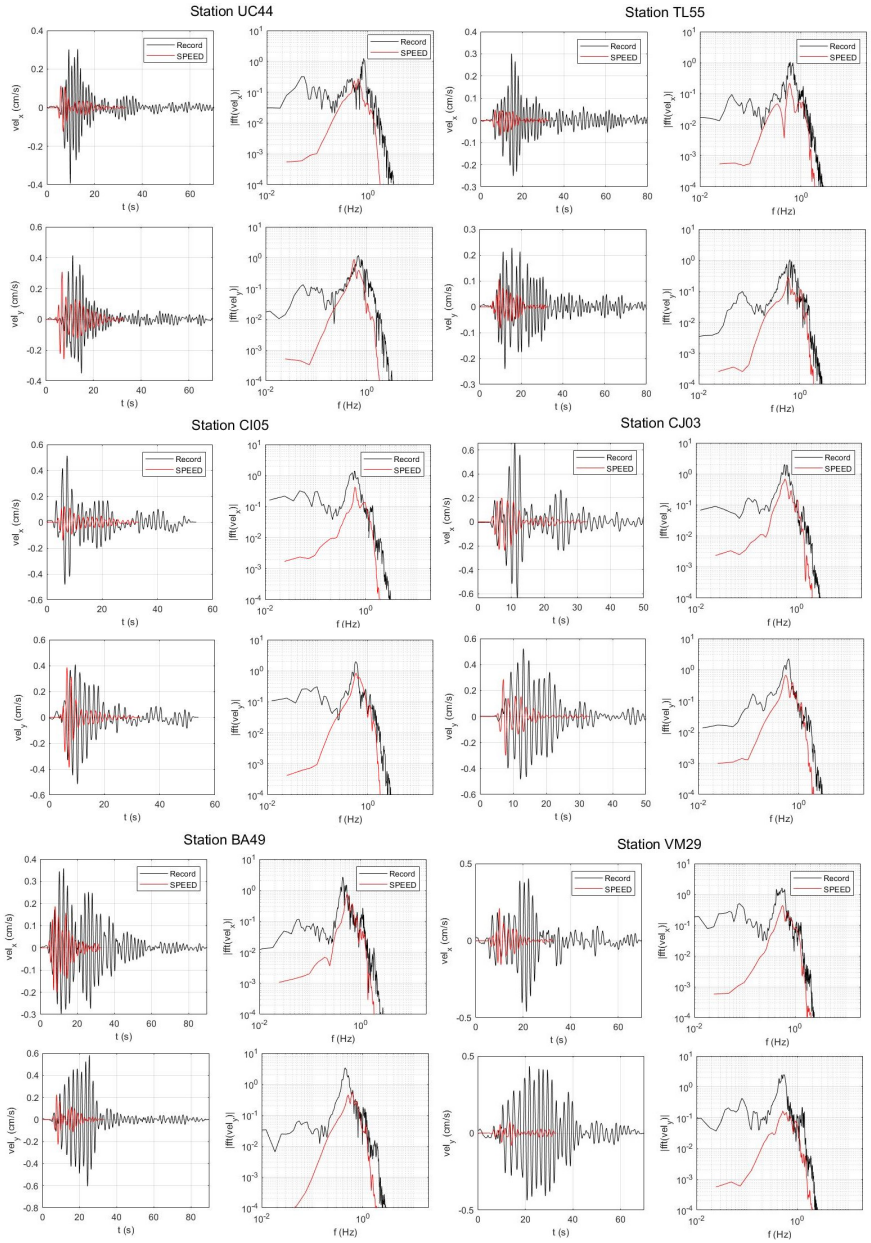

Figure 4.7: Comparison between computed (from simulation 3D-Qv) and recorded velocity time-histories and their corresponding FAS, at some stations in the lake zone.

For the hill and transition zones, there is an overall good agreement with records (GoF scores from good to excellent). It is notorious the case of station MT50, with a poor score. In reality, station MT50 is located around 200 m from the edge of the basin, however, in the numerical mesh it is located at just 10 m from the edge, therefore the assigned thickness of sediments to

that point is minimal. It's important to keep in mind that 3D physics-based simulations are meant to give a general picture of the ground shaking for its application to local-regional seismic risk analyses. PBS can't substitute site-specific ground response analyses, where a detailed subsoil characterization is available.

For lake zone, the numerical simulation provided results that are in fair and poor agreement with the records. Three might be the reasons for this:

1. The minimum V_S for the lake zone was set to 70 m/s to limit the number of degrees of freedom of the model. In reality V_S might be as low as 50 m/s in some parts of the city.
2. The adopted Q_s value might be too low. The mechanical properties assigned to the transition and lake zone are the same, the only difference between them is the thickness of sediments, however, the fit of the results for the transition zone is good while for the lake zone it is not. Q-factor might be playing an important role considering that the lake zone is farther to the epicenter than the transition zone, thus seismic waves do more cycles and get more attenuated.
3. The mechanical properties of the deep deposits are poorly known, especially the Q-factor. The assigned properties were based on few experimental results found on the literature.

4.1.2 Surface waves

In a horizontally layered medium, the surface wave propagation is a multimodal phenomenon: at each frequency, larger than a well-defined cut-off frequency, different modes of vibration exist. Each mode is characterized by its own propagation velocity, which always increases from the fundamental to the higher modes (overtones). The existence of higher modes of surface waves in heterogeneous media is due to constructive interference phenomena occurring among waves undergoing multiple reflections at the layer interfaces. Energy distribution is also a frequency dependent phenomenon: a mode can be strongly dominating within a certain frequency band, while negligible in other frequency bands (Foti et al., 2018).

As mention in section 2.5, Shapiro et al. (2001) shows that the wavefield in the lake-bed zone bed zone is dominated by higher-mode surface waves. Figure 4.9 shows the normalized vertical-component displacement measured by Shapiro et al. (2001) at different depths at four locations in the deep part of the lake zone, together with the theoretical eigenfunctions (profile of

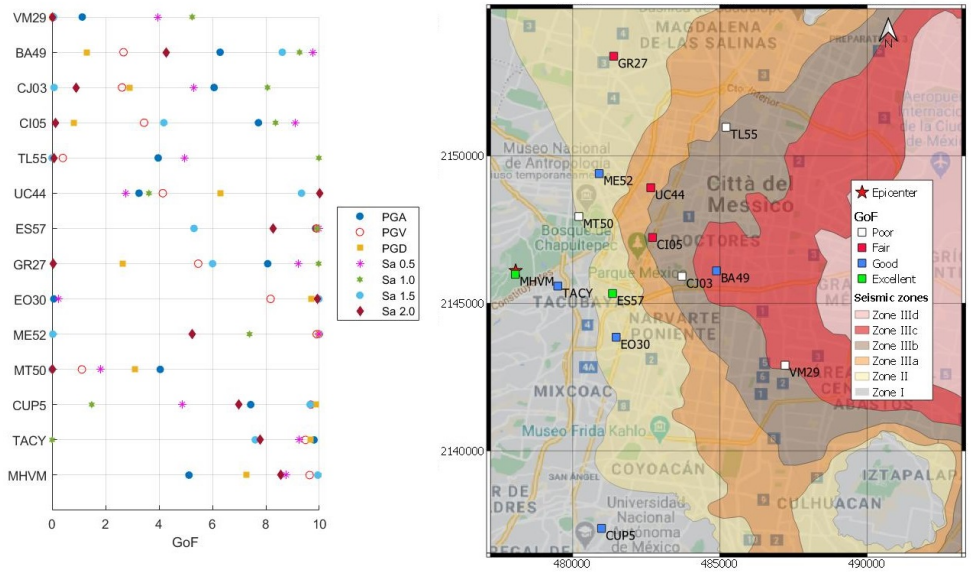

Figure 4.8: Goodness-of-Fit for simulation 3D-Qv. Left: GoF scores computed on the gmh of PGA, PGV, PGD, and Sa at T = 0.5, 1.0, 1.5, and 2.0 s. Right: map of the mean GoF scores.

displacements with depth) for the Rayleigh waves fundamental mode (black lines) and first overtone (blue lines), for the 1D velocity model that they considered representative for the lake-bed zone. The *Elastodynamics* toolbox for Matlab[2] (EDT) was used to compute the theoretical eigenfunctions in Figure 4.9.

EDT uses the direct stiffness method, in which the equilibrium of the medium is expressed in the frequency-wavenumber domain as $\underline{\mathbf{P}} = \underline{\underline{\mathbf{K}}}\,\underline{\mathbf{U}}$. If the load vector $\underline{\mathbf{P}}$ vanishes, non-trivial solutions for the displacements $\underline{\mathbf{P}}$ can be obtained if the determinant of the stiffness matrix $\underline{\underline{\mathbf{K}}}$ is zero. This equation corresponds to an eigenvalue problem in terms of the frequency ω and the complex horizontal wavenumber k_x. The eigenvalue problem is transcendental, has an infinite number of solutions, and is solved with search techniques. For each frequency ω, the phase velocity $C_R(\omega)$ of the Rayleigh wave is obtained as the ratio $\omega/Re[k_x]$ where (ω, k_x) is a solution of the characteristic equation.

[2] bwk.kuleuven.be/bwm/edt

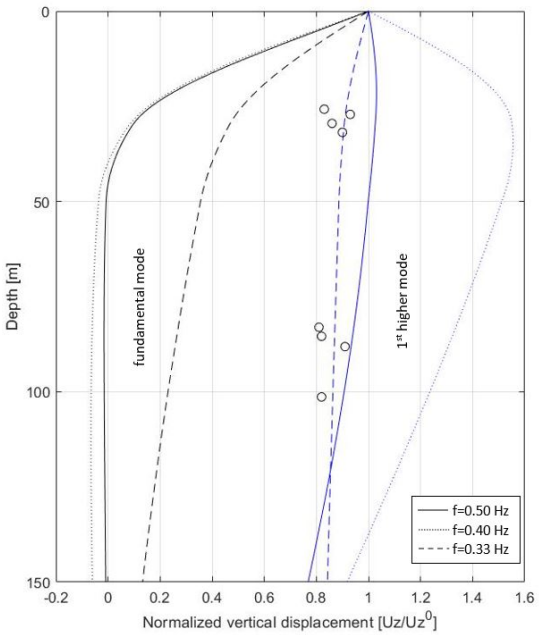

Figure 4.9: Dots represent the normalized vertical displacement measured by Shapiro et al. (2001) at different depths at four locations in the lake-bed zone, while the theoretical eigenfunctions for the Rayleigh waves fundamental mode and first overtone are represented by the black and blue lines, respectively. This experimental evidence shows that the wavefield in the lake-bed zone bed zone is dominated by higher-mode surface waves.

In Figure 4.10 are shown the Rayleigh waves dispersion curves for two representative 1D profiles, a "shallow" site (for sites within 2 to 5 kilometers from the basin edge) and a "deep" site (representative for the center of the basin). These curves were computed using the software HVInv (García-Jerez et al., 2016) which is based on the Thomson-Haskell propagator-matrix method.

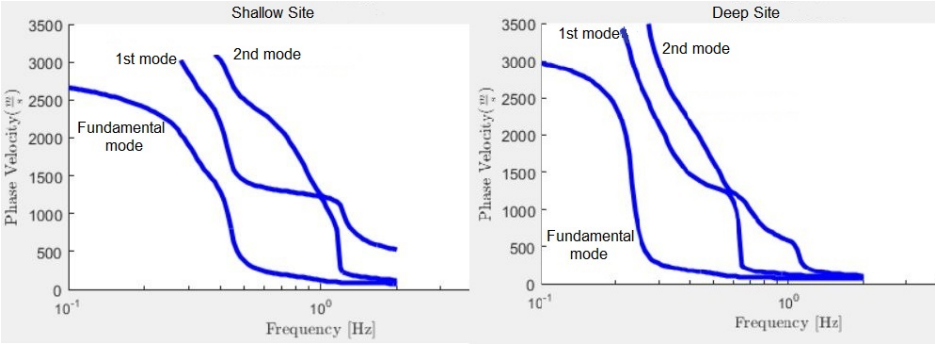

Figure 4.10: Dispersion curves of the Rayleigh waves phase velocity for two representative 1D profiles within the basin (shallow and deep sites).

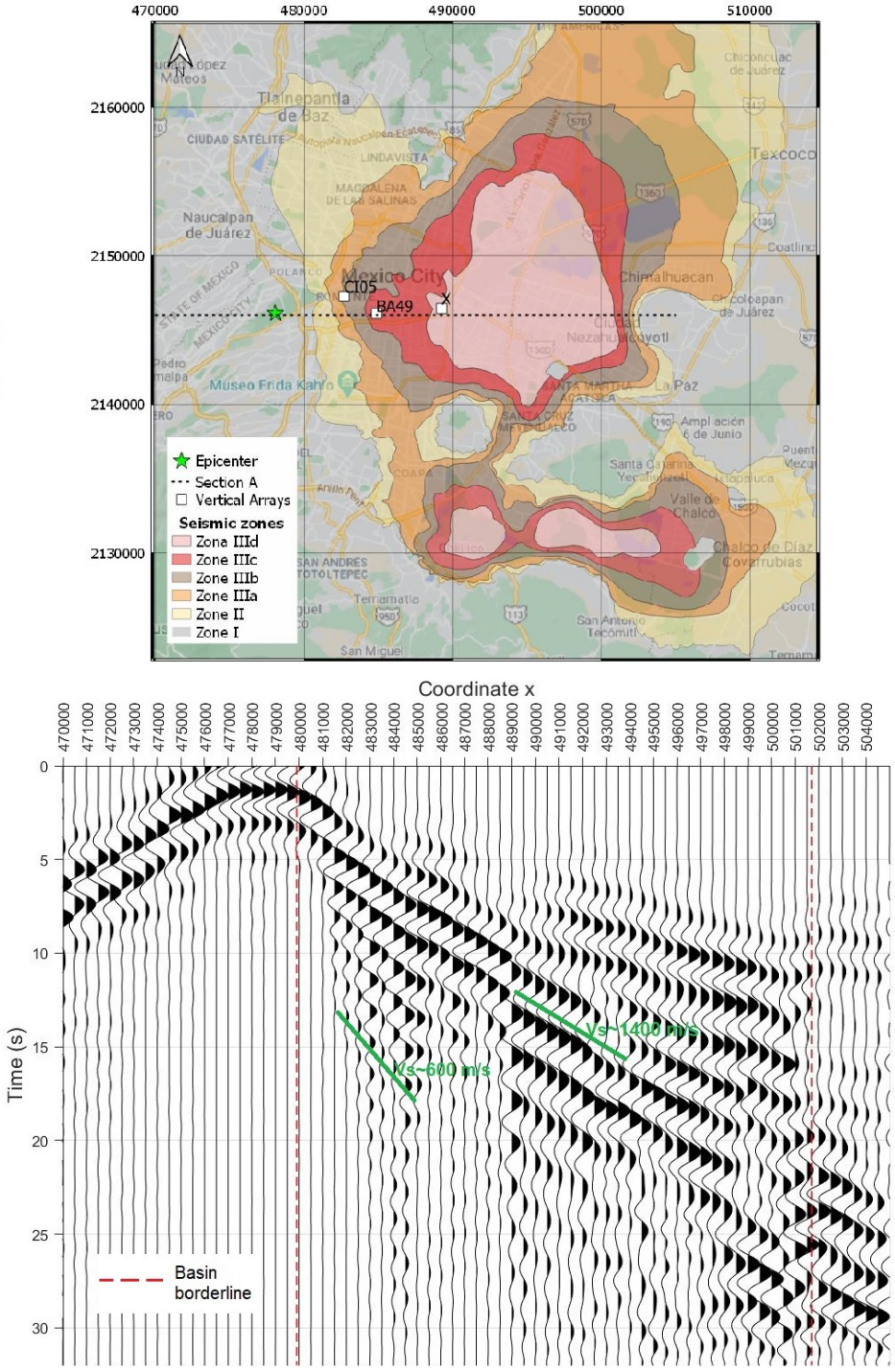

Figure 4.11: Upper panel: Map of Mexico City showing location of Section A for which a seismogram was extracted, and the points where vertical arrays were placed. Lower panel: Normalized seismic profiles of the E-W displacement along Section A, for simulation 3D-Qv at 0.5 Hz. The computed Rayleigh waves phase velocities correspond to the fundamental mode and first overtone.

Figure 4.11 shows normalized seismic profiles of the E-W displacement (radial component) at 0.5 Hz, along Section A with coordinate Y=2'146'000. After the direct S-wave arrivals, waves propagating with a phase velocity of ∼1400 m/s are clearly distinguished. Considering the Rayleigh waves dispersion curves in Figure 4.10, this train of waves most probably corresponds to the first overtone. At around 1 km from the basin edge, another surface wave becomes evident with a phase velocity of ∼600 m/s, which most likely corresponds to the fundamental mode. Since the energy of the fundamental model is concentrated in the superficial part of the basin, where quality factors are lower, this mode gets attenuated after few kilometers.

Vertical displacements (d_z) were extracted from three vertical arrays, whose locations are shown in Figure 4.11. From the results shown in Figure 4.12, for the three arrays the d_z (at 0.5 Hz) remains nearly constant with depth, clearly corresponding to a Rayleigh wave higher-mode.

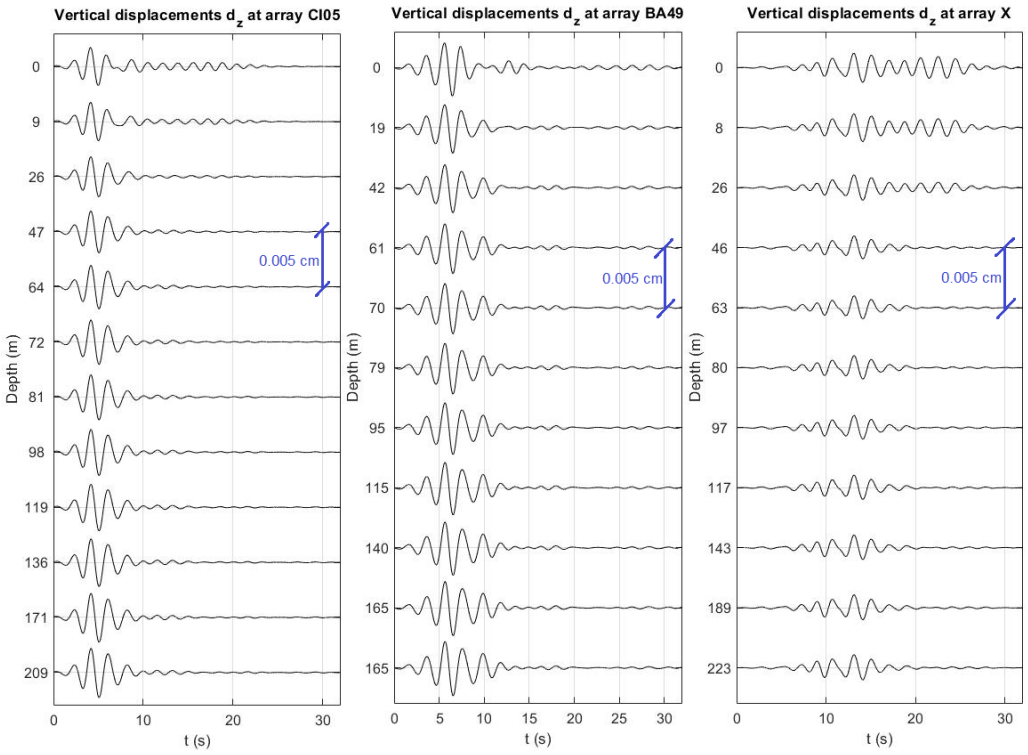

Figure 4.12: Distribution with depth of vertical displacements for simulation 3D-Qv (at 0.5 Hz), for the three arrays shown in Figure 4.11. The amplitude of displacements remains nearly constant with depth, confirming that higher mode surface waves dominate the ground motion within the basin.

Similarly than for Rayleigh waves, the phase-velocity dispersion curves

for Love waves were computed using HInv. Results are presented in Figure 4.13.

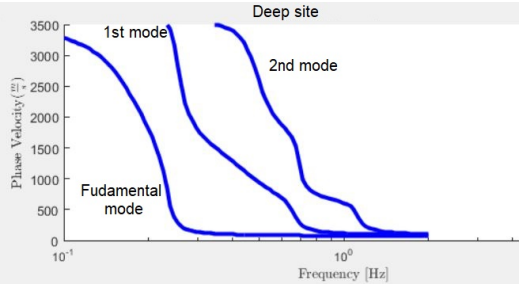

Figure 4.13: Dispersion curves of the Love waves phase velocity for a representative 1D profile at the basin center.

Figure 4.14 shows normalized seismic profiles of the N-S displacement (transverse component) at 0.5 Hz, along Section A. Various pulses with approximately the same phase velocities are observed after the direct arrivals. From figure 4.13 it is clear that the measured phase velocities do not correspond to the fundamental or the second mode, but rather they are similar to that of the first overtone.

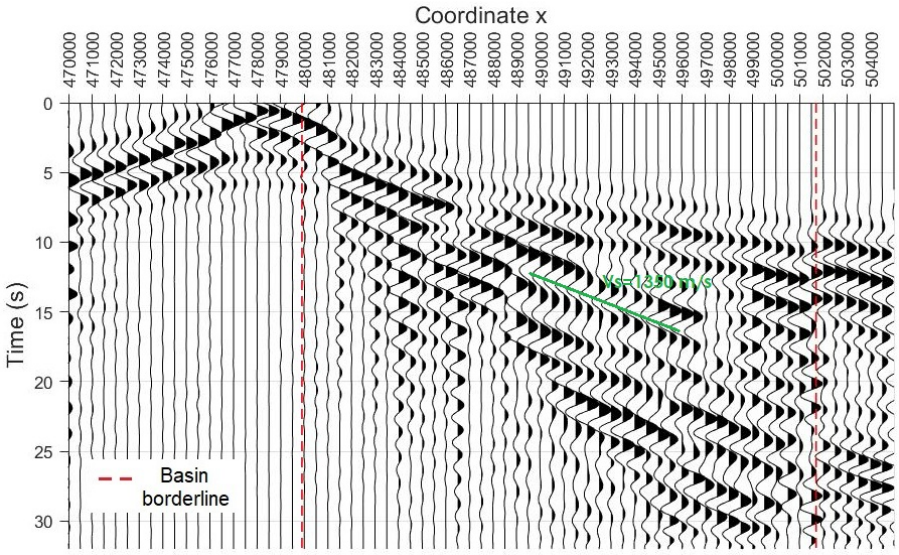

Figure 4.14: Normalized seismic profiles of the N-S displacement along Section A, for simulation 3D-Qv at 0.5 Hz. The observed Love waves phase velocities correspond to the first overtone.

The results presented in this subsection support the observations of Shapiro et al. (2001) and Cruz-Atienza et al. (2016), that higher-mode surface waves dominate the ground motion within the Mexico City basin.

4.2 Results for case 3D-Qh

In this section the results of the simulation 3D-Qh (constant Q factor) are presented. The simulation was stopped at 25.2 seconds for computational limitations. Velocity snapshots for the E-W component are shown in Figure 4.15, from which amplification, diffraction and generation of surface waves at the basin edges are clearly observed.

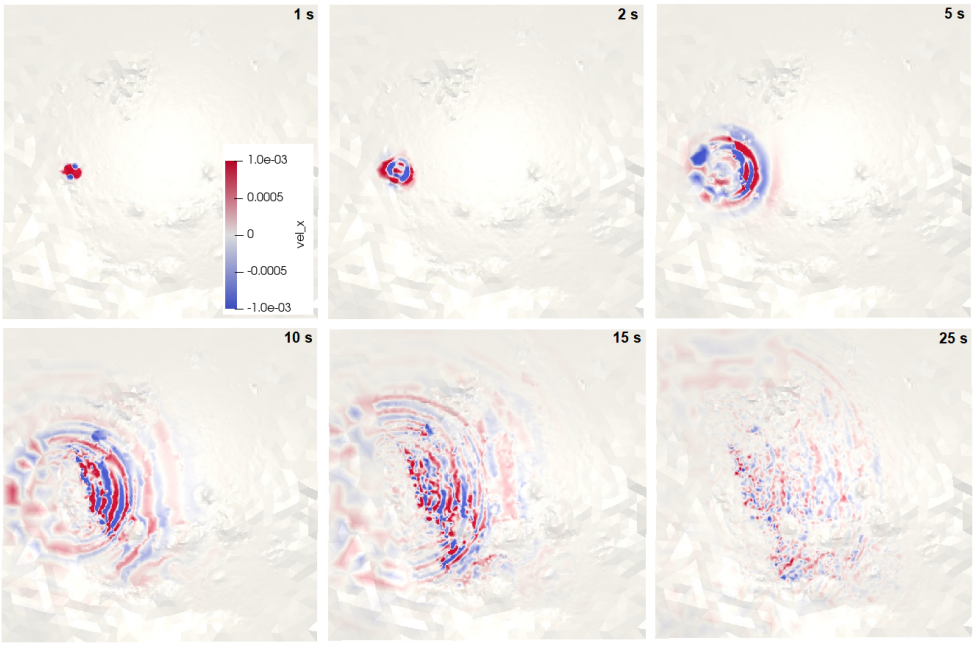

Figure 4.15: Snapshots of velocity (E-W component) from simulation 3D-Qh. Amplification, diffraction and generation of surface waves at the basin edges are clearly observed.

Figure 4.16 shows maps of Peak Ground Velocity (PGV) for components E-W, N-S, Up-Down (U-D) and gmh, with superimposed velocity traces extracted at some stations. When comparing the velocity traces of station CJ03 (lake zone) with those of TACY and CUP5 (hill zone), the most evident difference is the long duration of the ground shaking in the lake zone. In the near field of the seismic point source, a two-lobed radiation pattern is evident from the PGV maps.

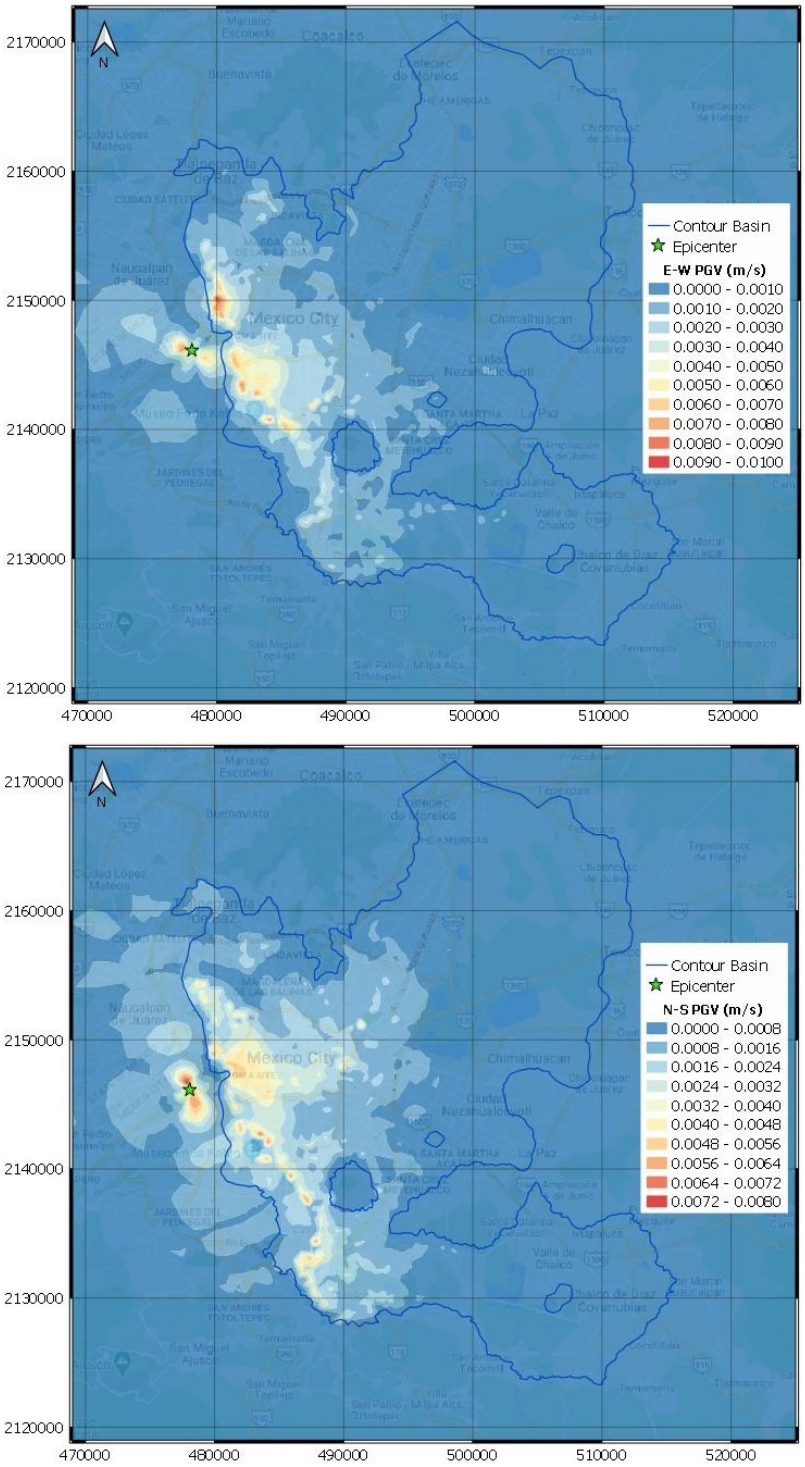

Figure 4.16: Spatial distribution of PGV from simulation 3D-Qh for components E-W and N-S, with superimposed velocity traces extracted at some stations. A two-lobed radiation pattern is evident.

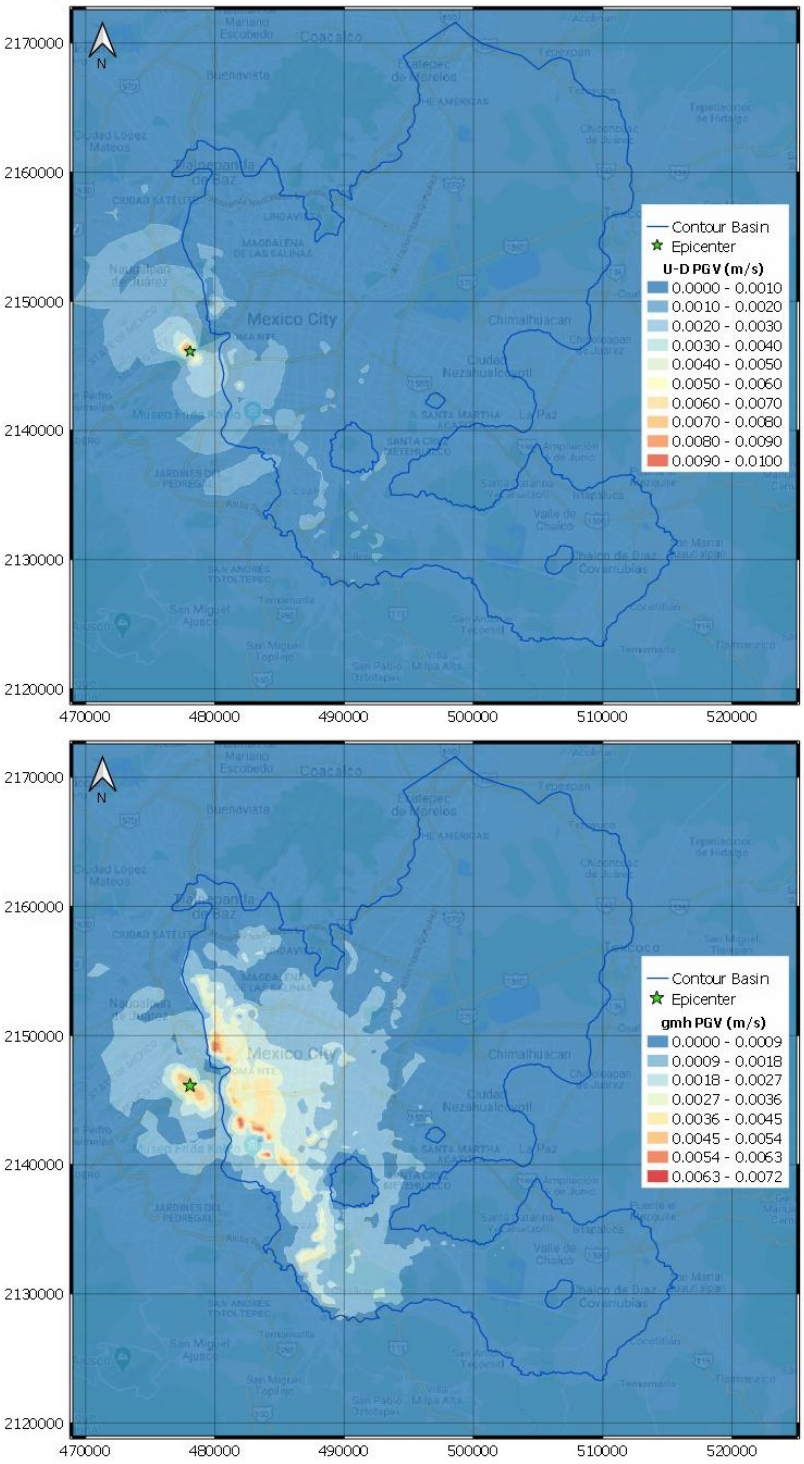

Figure 4.16: Spatial distribution of PGV from simulation 3D-Qh for components U-D and gmh, with superimposed velocity traces extracted at some stations. A two-lobed radiation pattern is evident (continued).

4.2.1 Comparison with records

In Figures 4.17 (lake zone) and 4.18 (hill and transition zones), records and synthetics are compared in time domain. It is evident from the results that the simulated time was not enough to completely simulate the ground shaking inside the basin. Since time histories are incomplete, Fourier spectra were not computed.

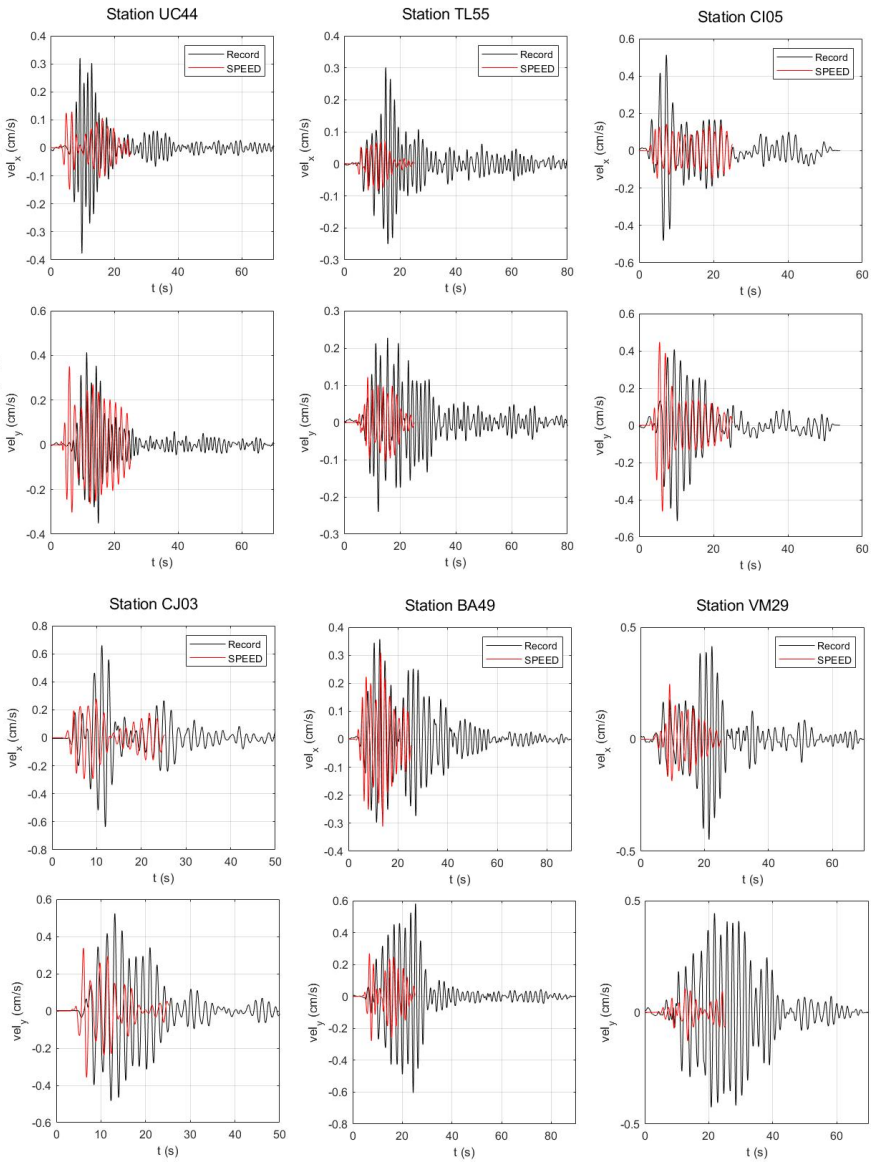

Figure 4.17: Comparison between computed (from simulation 3D-Qh) and recorded velocity time-histories at some stations in the lake zone.

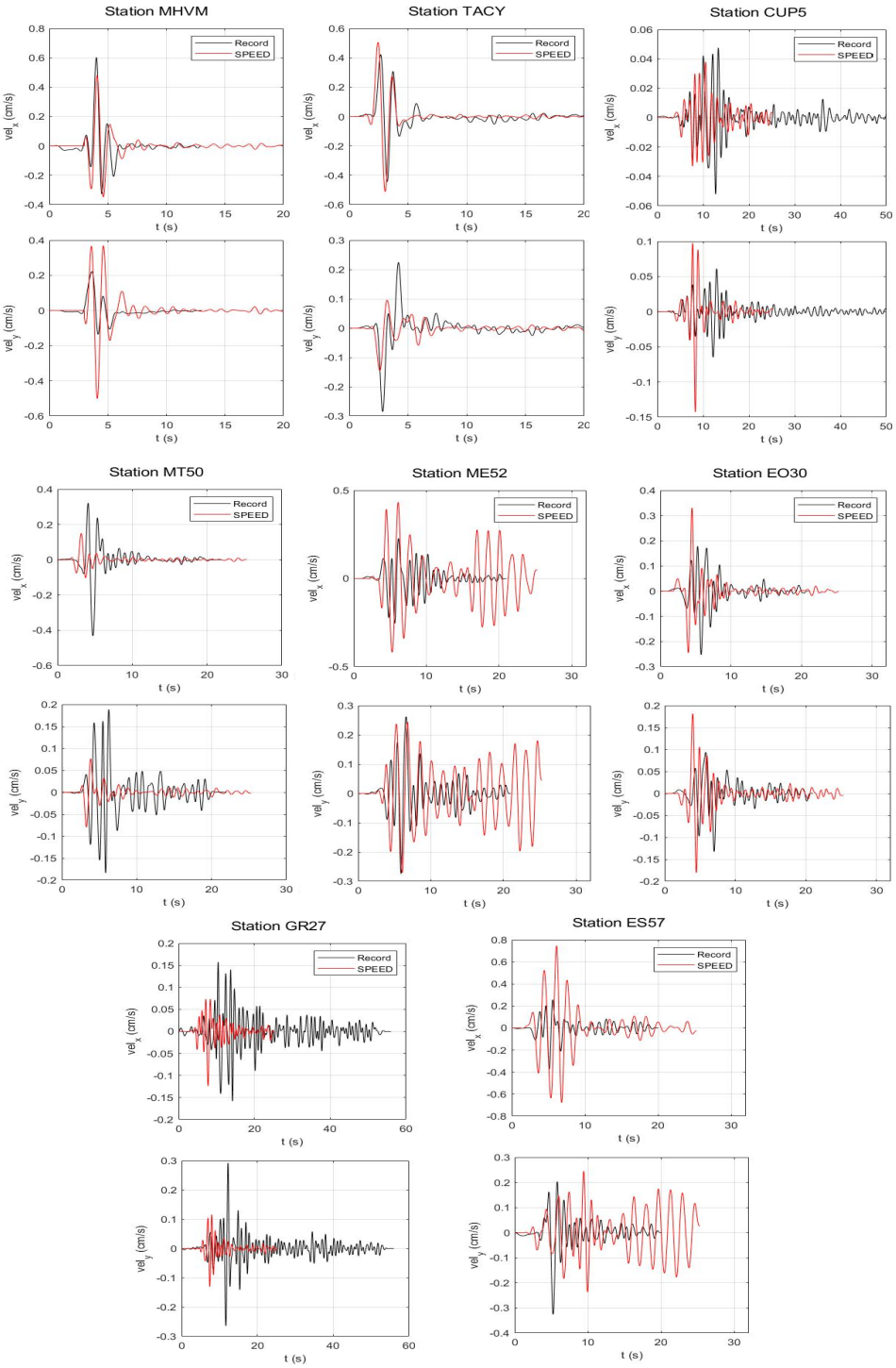

Figure 4.18: Comparison between computed (from simulation 3D-Qh) and recorded velocity time-histories at some stations in the hill and transition zones.

Similarly than for simulation 3D-Qv, the overall performance of the numerical simulations was quantitatively estimated through the Goodness-of-Fit. In this case just PGA, PGV and PGD were considered. Spectral accelerations could have been computed provided that the synthetics were tapered, however, they wouldn't have been comparable to the recorded ones. The GoF scores for the geometric mean of horizontal components, computed for each criteria, are shown in Figure 4.19.

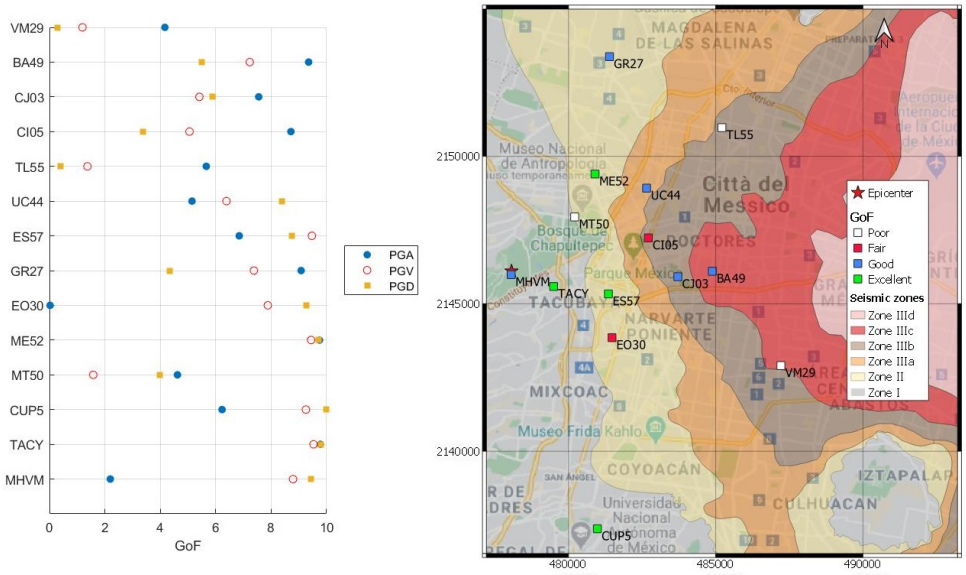

Figure 4.19: Goodness-of-Fit for simulation 3D-Qh. Left: GoF scores computed on the gmh of PGA, PGV and PGD. Right: map of the mean GoF scores.

For the hill and transition zones, once again there is an overall good agreement with records (GoF scores from good to excellent). As for the 3D-Qv case, the mean GoF for station MT50 is poor, for the reasons previously explained.

Differently than for the 3D-Qv simulation, station EO30 presents a fair agreement. Station ES57 which is close to station EO30, presents an excellent agreement on the evaluated peak values, however, from its time history (figure 4.17), it's possible to observe that there is an overestimation on duration and amplitude. These two stations are located in the transition zone, where the thickness of the clay deposits should be around 10 m, however, from a close inspection to that part of the mesh, it was observed that the assigned thickness in the model was ∼27 m, which might explain the overestimation in duration and amplitude. For stations TL55 and VM29 in the lake zone, which have a poor GoF score, the opposite happened, there is an

underestimation of duration and amplitude of the ground motion. The real clay thickness for these sites should be around 35 and 40 m, respectively, but the assigned thickness in the model was ∼27 m, most probably leading to an underestimation of the response.

4.2.2 Surface waves

Figure 4.20 shows normalized seismic profiles of the E-W (radial component) displacement at 0.5 Hz, along Section A with coordinate Y=2'146'000. As for the 3D-Qv simulation, one main wave train is observed propagating phase velocity of ∼1350 m/s. Considering the Rayleigh waves dispersion curves in Figure 4.10, this train of waves most probably corresponds to the first overtone. At around 1 km from the basin edge, another surface wave appears with a phase velocity of ∼650 m/s, which seems to be the fundamental mode.

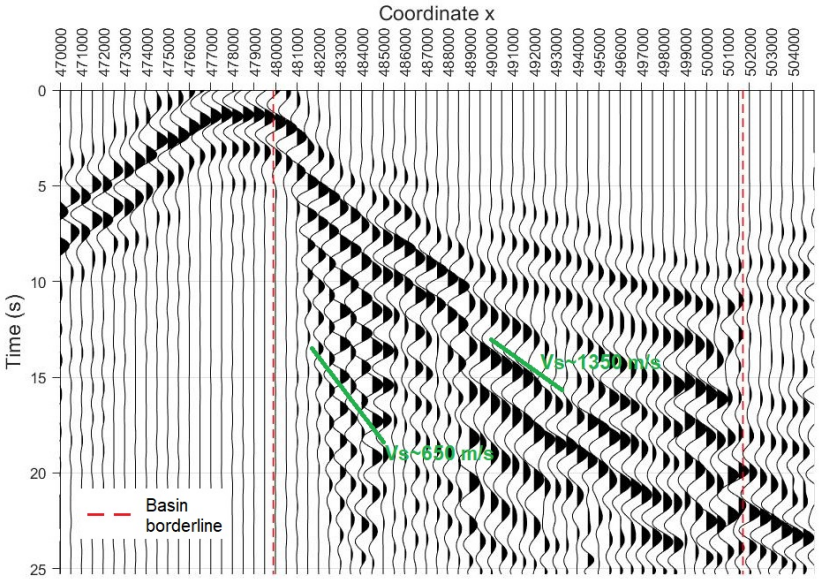

Figure 4.20: Normalized seismic profiles of the E-W displacement along Section A, for simulation 3D-Qh at 0.5 Hz. The observed Rayleigh waves phase velocities correspond to the fundamental mode and first overtone.

More evidence of the propagation of Rayleigh waves is presented in Figure 4.21, that shows the particle's motion (odograms) in the radial-vertical plane for stations CI05 and BA49. Prograde ellipses typical of higher mode Rayleigh waves are evident.

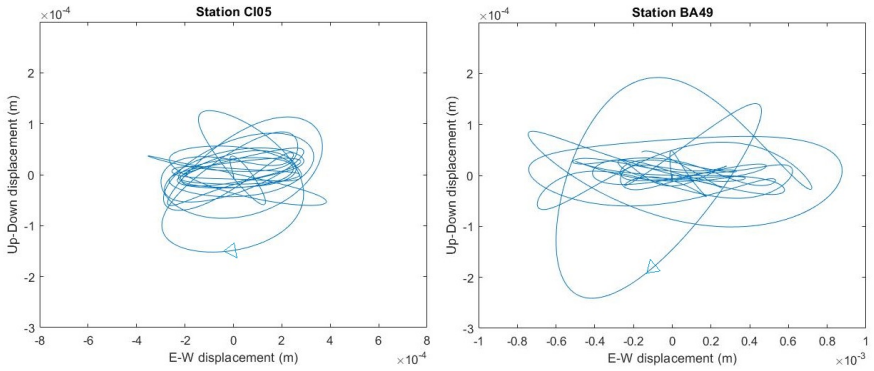

Figure 4.21: Particle motion trajectories in the radial-vertical plane for stations CI05 (left) and BA49 (right). Displacements are low-pass filtered at 1.3 Hz.

4.3 Comparison and Discussion

In the previous section it was mentioned that poor GoF scores might be related to differences in the real clay thickness and the assigned thickness in the numerical model. It is important to keep in mind that the basin was modeled using the not-honoring technique, for which it is evaluated whether a LGL node is located above or below the surface representing the boundary between the caly and deep deposits. Mechanical properties of the clay are assigned to the nodes above the surface. Spectral elements in the uppermost part of the basin have a degree n=5 and their dimensions are approximately 100 m in the horizontal directions and 75 m in the vertical one, as shown in Figure 4.22. For instance, for site VM29 where a poor GoF score was obtained, the real clay thickness is around 40 m, and although the clay basin surface had approximately the correct depth, clay mechanical properties were assigned just to the LGL nodes up to a depth of ∼27 m.

A good idea might be to edit the clay base surface (figure 3.11), in order to have better estimates of the layer thickness. Furthermore, the not-honoring technique could be modified to assign clay mechanical properties also to the LGL nodes that are below the surface within some range. With this modification, most probably the numerical results for the basin will be more accurate.

Results for the hill zone were very similar for both analyses. For analysis 3D-Qv, reference quality factors were assigned for a reference frequency f_0=0.9 Hz, therefore, for lower frequencies their values are smaller. On the other hand, for analysis 3D-Qh, quality factors are identical to the reference values of analysis 3D-Qv, but they are constant for the entire frequency band of interest. Figure 4.23 shows a comparison of the results at station CUP5

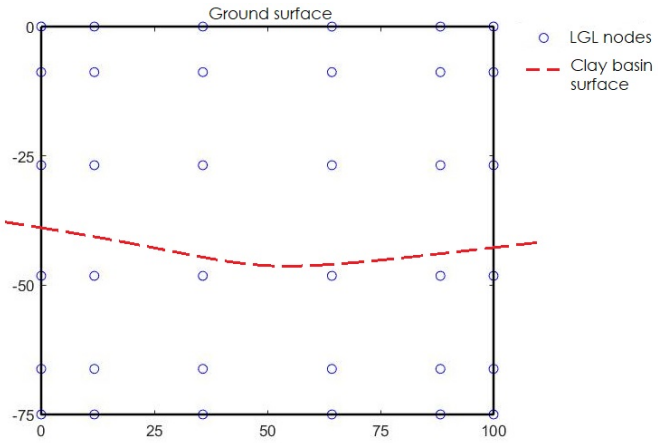

Figure 4.22: Representative spectral element for the uppermost part of the basin. LGL nodes are shown with small circles (for degree n=5). Using the not-honoring technique, clay mechanical properties are assigned to the LGL nodes above the clay basin surface.

for both analyses. As expected, for frequencies lower that the reference one, amplitudes for 3D-Qv case are slightly smaller that those of 3D-Qh due to the smaller quality factors.

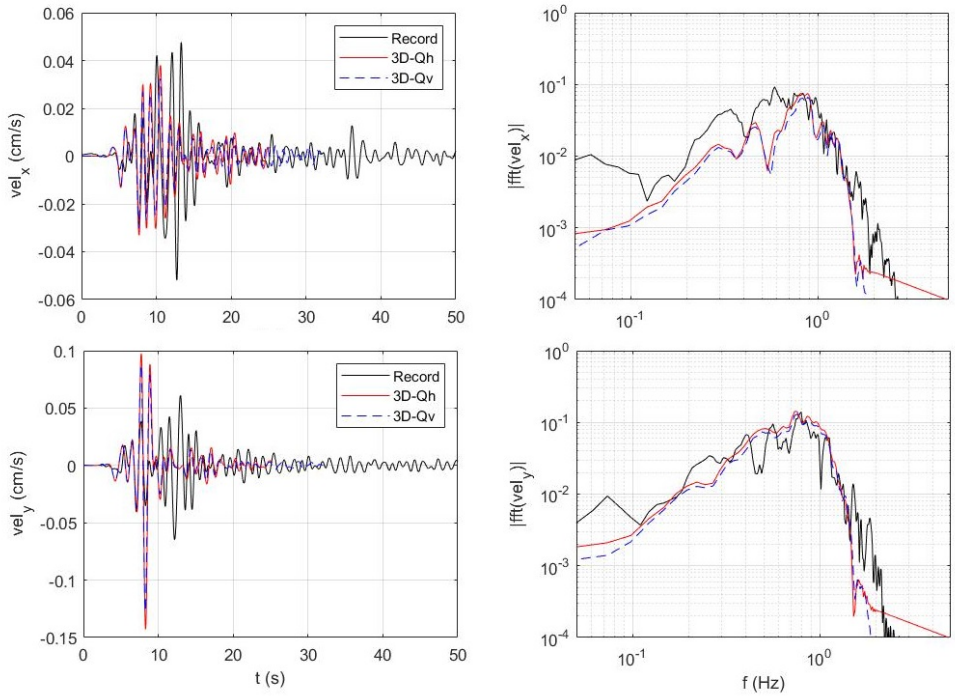

Figure 4.23: Comparison of velocity time-histories and their corresponding FAS, between simulations 3D-Qv and 3D-Qh, at station CUP5 in the hill zone.

In contrast, results for the basin were quite different for both analyses. Apart from the difference in the type of damping, S-wave quality factors of clay deposits for case 3D-Qh were computed as $Q_s = V_S/2$, while for case 3D-Qv as $Q_s = V_S/3$. Evidently, amplitudes and duration of ground shaking for analysis 3D-Qh were higher due to the lower attenuation. The difference between both analyses becomes clear when analyzing Figure 4.24, where normalized seismic profiles of the E-W displacement along Section A, low-pass filtered at 1.3 Hz, are presented. Both seismograms have the same scaling factor. As mentioned in the previous sections, fundamental mode surface waves are more affected by the clay deposits than higher mode surface waves, therefore, the difference in results is more important in the part of the basin enclosed by the blue circle, between coordinates X=481'000 and 485'000, because there, fundamental mode surface waves propagate. Furthermore, it can be seen that in the deeper part of the basin, amplitude of surface waves is even higher than the direct arrivals.

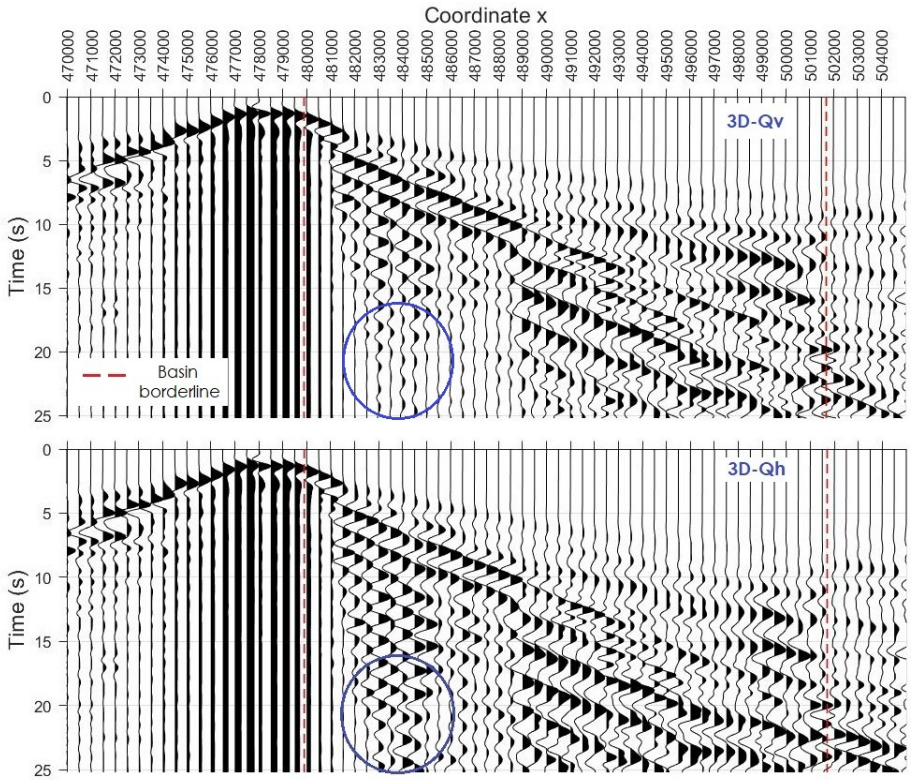

Figure 4.24: Comparison between normalized seismic profiles of the E-W displacement along Section A, for simulations 3D-Qv (upper panel) and 3D-Qh (lower panel). Results were low-pass filtered at 1.3 Hz.

From Figure 4.24 it is also observed that there is a huge difference in

ground shaking duration between the hill and lake-bed zone. Basin-edge generated surface waves, in addition to the wavefield dispersion and diffraction across the 3D basin structure, elongates the duration of ground motion. This implies that duration of the incoming wavefield from subduction and intermediate-depth intraplate earthquakes should be significantly shorter than the observed duration in the lake-bed zone, and the ground motion at hard-rock sites should not be considered as the basin incoming wavefield (Cruz-Atienza et al., 2016).

Much has been said about the dominance of surface waves in the Mexico City basin, but how are they generated? When lateral heterogeneities are present, surface waves, which propagate horizontally across the basin even in the case of body wave incidence, are mainly generated at the basin edge. They are caused by the complex interaction of incident body waves and diffracted waves (Pilz et al., 2018). Both Love and Rayleigh waves are generated by the incidence of SH and P-SV waves, respectively. Theoretical evidences of such basin-induced surface waves have been demonstrated by many researchers (e.g., Trifunac, 1971; Bard and Bouchon, 1980a,b; Narayan, 2005). Observational evidence was first reported by Hanks (1975) with reference to the 1971 San Fernando earthquake. The excitation strength of basin-induced surface waves is strongly affected by source spectra (frequency content) and angle of incidence (e.g., Furumura et al., 1997), shape of the basin and impedance contrast (e.g., Bard and Bouchon, 1980a), and soil thickness (e.g., Narayan, 2005).

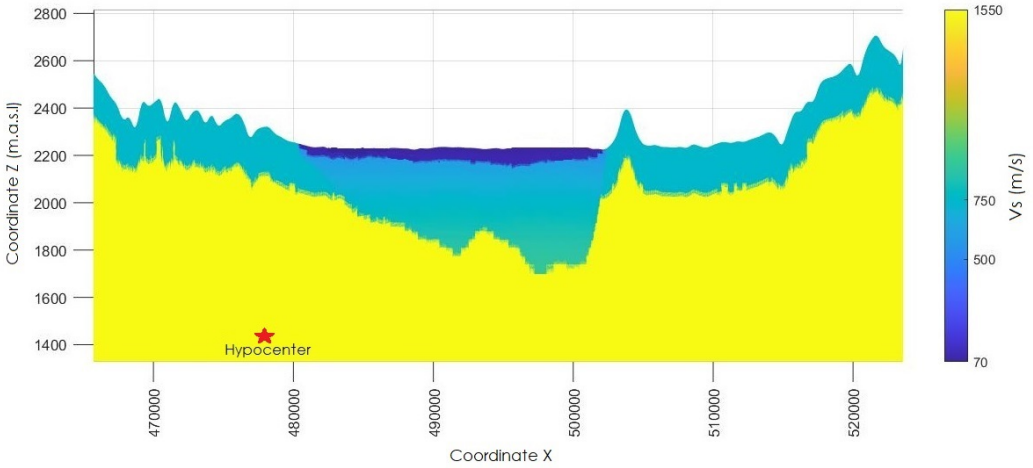

Figure 4.25: Cross-section (with coordinate Y=2'146'000) with V_S values. The shape of the basin is clearly seen and the location of the hypocenter is shown with a red star.

Figure 4.25 shows a cross-section (along section A), with Vs values, where

the shape of the basin is clearly seen and the location of the hypocenter is shown with a red star. The seismic source produces P and S body waves, that generate surface waves when they reach the basin-edge. The large incidence angle to the edge ($\sim$70° w.r.t the vertical) might be related the observed strong excitation of surface waves. For different earthquake scenarios, e.g. subduction earthquakes, in addition to the excitation of the basin by body waves (with an approximate vertical incidence), incoming surface waves will be transduced into the basin and amplified.

Chapter 5

Conclusions

Tools for earthquake ground motion predictions are one of the key elements in seismic hazard assessment. In general, ground motion prediction equations (GMPEs) are adopted for this purpose, however they suffer of some intrinsic limitations. To overcome these limitations, 3D physics-based numerical simulations (PBS) of earthquake ground motion has emerged as a powerful alternative tool to the use of GMPEs.

This research work aimed to investigate the possibility to generate realistic synthetic ground motions in the low frequency range for the Mexico City basin, using 3D physics-base numerical simulations. The study of the Mexico City case was motivated for the unique subsoil condition prevailing in its lake-bed zone, leading to the well-known large local amplification phenomenon. Furthermore, the need to reevaluate the seismic hazard posed by local crustal earthquakes has been recently brought to light.

A three-dimensional conforming numerical mesh for the Mexico City area was created. The model consists in approximately $308.7 \text{x} 10^6$ total degrees of freedom, and allows to resolve frequencies up 1.3 Hz. Event though the maximum frequency is relatively low, it allows to model the main features of the basin's lacustrine sediments.

Based on the results from the numerical simulations carried out using the high-performance spectral element code SPEED, it can be concluded that using a hysteretic damping model (simulation 3D-Qh) it is possible to compute synthetics that are in a general fair and good agreement with recorded ground motions. Results for the hill zone are all in good and excellent agreement, however, inside the basin there were some stations with a poor agreement. For the sites where the agreement with records was worst, it was observed that the assigned thickness of clay in the mesh was different to the thickness the sites should have according to their seismic zones. In order to improve the accuracy of the results, some refinements could be made to the numerical model. The most important one is the geometrical redefinition of the clay deposits surface.

With the use of 3D PBS, the obtained synthetics reflect the spatial variability of ground motion, as shown in the maps for peak parameters. SPEED allows to obtain improved results, owing to the inclusion of all factors that affect seismic motion from the source to the site, such as focal mechanism, topographic effects, 3D site effects, which cannot be take into account by ground motion prediction equations.

An important part of this thesis was dedicated to analyze the September 19, 1985 and September 19, 2017 earthquakes. They were completely different events, but both of them had disastrous consequences, especially for Mexico City. It was shown that the main difference between these events was the frequency content, that lead to a completely different pattern of damage. The 1985 earthquake mainly affected the areas of the city with dominant site periods around 2 seconds, while for the 2017 earthquake, the damage was concentrated in the zones with periods between 0.5-1.5 seconds. This points out the relevance of seismic microzonation studies.

The Michoacán earthquake put in evidence the exceptionally long shaking duration and the large site effects in the basin. Some of the first attempts to evaluate site effects in Mexico City used vertical S-wave propagation models, however these models fail completely to account for the difference in the duration of strong ground motion between the different geotechnical zones. The use of 2D models including the deep deposits highlighted their importance, because they are responsible for important spectral amplifications. The importance of the basin-edge generated surface waves was also pointed out, however, in early attempts just the fundamental mode was considered, which is attenuated significantly over short distances.

The numerical results presented in chapter 4 suggested that body waves arriving to the basin edge generate surfaces waves, because of the finiteness of the basin. A more complex incoming wavefield would also include amplification of surfaces waves transduced into the basin. To model these two phenomena, 2D and 3D models are necessary.

Moreover, it was found that in the deep sites of the basin, higher mode surface waves dominate the wavefield. The main difference between fundamental and higher mode is that energy of the fundamental model is concentrated in the superficial clay, while the higher modes propagate mainly in the deep deposits, where the attenuation is lower, hence, they can propagate longer distances inside the basin. Therefore, the effect of the mechanical properties of the deep basin should be relevant. Mechanical properties for the deep deposits are poorly known, and the parameters used in the simulations were assigned based on few experimental results available on the literature. Thus,

a better characterization of the deep deposits is needed.

Future endeavors related to this thesis might include the following:

- Optimization of the DG algorithm in order to reduced the set-up time. The impedance contrast between the clay deposits and the surrounding materials, makes the Mexico City case well suited for the use of a discontinuous mesh.
- Refine the mesh for the lake zone, to get better estimates of the clay thickness.
- Carry out further simulations using the same reference earthquake, in order the better calibrate the mechanical parameters of the deep deposits and the attenuation properties of the clay deposits.
- Introduce finite-fault local earthquake scenarios with a larger magnitude, in order to reevaluate the seismic hazard of Mexico City.

Bibliography

Aki, K. (1966). Estimation of earthquake moment, released energy, and stress-strain drop from G-wave spectrum. *Bulletin of Earthquake Research Institute*, 44(12):73–88.

Aki, K. and Richards, P. G. (2002). *Quantitative seismology*. University Science Books.

Anderson, J. G. (2004). Quantitative measure of the goodness-of-fit of synthetic seismograms. *Proceedings of the 13th World Conference on Earthquake Engineering*, (243):243.

Anderson, J. G., Bodin, P., Brune, J. N., Prince, J., Singh, S. K., Quaas, R., and Onate, M. (1986). Strong ground motion from the Michoacan, Mexico, earthquake. *Science*, 233(4768):1043–1049.

Anderson, J. G. and Quaas, R. (1988). The Mexico Earthquake of September 19, 1985—Effect of Magnitude on the Character of Strong Ground Motion: An Example from the Guerrero, Mexico Strong Motion Network.

Antonietti, P. F., Mazzieri, I., Quarteroni, A., and Rapetti, F. (2012). Non-conforming high order approximations of the elastodynamics equation. *Computer Methods in Applied Mechanics and Engineering*, 209-212:212–238.

Arce, J. L., Layer, P. W., Macías, J. L., Morales-Casique, E., García-Palomo, A., Jiménez-Domínguez, F. J., Benowitz, J., and Vásquez-Serrano, A. (2019). Geology and stratigraphy of the Mexico Basin (Mexico City), central Trans-Mexican Volcanic Belt. *Journal of Maps*, 15(2):320–332.

Arroyo, D., Ordaz, M., Ovando-Shelley, E., Guasch, J. C., Lermo, J., Perez, C., Alcantara, L., and Ramírez-Centeno, M. S. (2013). Evaluation of the change in dominant periods in the lake-bed zone of Mexico City produced by ground subsidence through the use of site amplification factors. *Soil Dynamics and Earthquake Engineering*, 44:54–66.

Auvinet, G., Méndez, E., and Juárez, M. (2013). Soil fracturing induced by land subsidence in Mexico City. *18th International Conference on Soil Mechanics and Geotechnical Engineering*, 4(Figure 2):2921–2924.

Auvinet, G., Méndez, E., and Juárez, M. (2017). *The subsoil of Mexico City vol. III*. Instituto de Ingeniería, UNAM, Ciudad de México.

Avilés, J. and Pérez-Rocha, L. E. (2010). Regional subsidence of Mexico City and its effects on seismic response. *Soil Dynamics and Earthquake Engineering*, 30(10):981–989.

Babuška, I. and Suri, M. (1987). The h-p version of the finite element method with quasiuniform meshes. *ESAIM: Mathematical Modelling and Numerical Analysis*, 21(2):199–238.

Babuška, I., Szabo, B. A., and Katz, I. N. (1981). The p-version of the finite element method. *SIAM Journal of Numerical Analysis*, 18(3):515–545.

Bard, P.-Y. and Bouchon, M. (1980b). The seismic response of sediment-filled valleys. Part 1. The case of incident SH waves. *Bull. Seismol. Soc. Am.*, 70(4):1263–1286.

Bard, P.-Y. and Bouchon, M. (1980a). The seismic response of sediment-filled valleys. Part 2. The case of incident P and SV waves. *Bull. Seismol. Soc. Am.*, 70(5):1921–1941.

Bard, P. Y., Campillo, M., Chavez-Garcia, F. J., and Sanchez-Sesma, F. (1988). Mexico earthquake of September 19, 1985 - a theoretical investigation of large- and small-scale amplification effects in the Mexico City valley. *Earthquake Spectra*, 4(3):609–633.

Barker, J. S., Campillo, M., Sanchez-Sesma, F. J., Jongmans, D., and Singh, S. K. (1996). Analysis of wave propagation in the Valley of Mexico from a dense array of seismometers. *Bull. Seismol. Soc. Am.*, 86(6):1667–1680.

Bayona-Viveros, J. A., Suárez-Reynoso, G., and Ordaz-Schroeder, M. G. (2017). A probabilistic seismic hazard assessment of the Trans-Mexican Volcanic Belt, Mexico based on historical and instrumentally recorded seismicity. *Geofisica Internacional*, 56(1):87–101.

Bielak, J., Ghattas, O., and Kim, E. J. (2005). Parallel octree-based finite element method for large-scale earthquake ground motion simulation. *CMES - Computer Modeling in Engineering and Sciences*, 10(2):99–112.

Bielak, J., Graves, R. W., Olsen, K. B., Taborda, R., Ramírez-Guzmán, L., Day, S. M., Ely, G. P., Roten, D., Jordan, T. H., Maechling, P. J., Urbanic, J., Cui, Y., and Juve, G. (2010). The ShakeOut earthquake scenario: Verification of three simulation sets. *Geophysical Journal International*, 180(1):375–404.

Boore, D. M. (2003). Simulation of Ground Motion Using the Stochastic Method. *Pure and Applied Geophysics*, 160(3):635–676.

Borcherdt, R. D. (1970). Effects of Local Geology on Ground Motion Near San Francisco Rbay. *Bull. Seismol. Soc. Am.*, 60(1):29–61.

Brune, J. N. (1970). Tectonic Stress and the Spectra of Seismic Shear Waves from Earthquakes. *Journal of Geophysical Research*, 75(27):4997–5009.

Campillo, M., Bard, P. Y., Nicollin, F., and Sanchez-Sesma, F. (1988). Mexico earthquake of September 19, 1985 - the incident wavefield in Mexico City during the great Michoacan earthquake and its interaction with the deep basin.

Campillo, M., Gabriel, J., Aki, K., and Sanchez-Sesma, F. (1989). Destructive strong ground motion in Mexico City: Source, path, and site effects during the great 1985 Michoacfin earthquake. *Bull. Seismol. Soc. Am.*, 79:1718–1735.

Campillo, M., Sánchez-Sesma, F. J., and Aki, K. (1990). Influence of small lateral variations of a soft surficial layer on seismic ground motion. *Soil Dynamics and Earthquake Engineering*, 9(6):284–287.

Canuto, C., Hussaini, M., Quarteroni, A., and Zang, T. (2006). *Spectral Methods: Fundamentals in Single Domains*, volume 23. Springer.

Chaljub, E., Moczo, P., Tsuno, S., Bard, P. Y., Kristek, J., Käser, M., Stupazzini, M., and Kristekova, M. (2010). Quantitative comparison of four numerical predictions of 3D ground motion in the Grenoble Valley, France. *Bull. Seismol. Soc. Am.*, 100(4):1427–1455.

Chaussard, E., Wdowinski, S., Cabral-Cano, E., and Amelung, F. (2014). Land subsidence in central Mexico detected by ALOS InSAR time-series. *Remote Sensing of Environment*, 140:94–106.

Chavez-Garcia, F. J. and Bard, P. Y. (1993). Gravity waves in Mexico City?-I. Gravity perturbed waves in elastic solid. *Bull. Seismol. Soc. Am.*, 83(6):1637–1655.

Chávez-García, F. J. and Bard, P. Y. (1994). Site effects in Mexico City eight years after the September 1985 Michoacan earthquakes. *Soil Dynamics and Earthquake Engineering*, 13(4):229–247.

Chávez-Pérez, S. and Sanchez-Sesma, F. J. (1992). Discussion of the paper 'Subsoil geology and soil amplification in Mexico Valley'. *Soil Dynamics and Earthquake Engineering*, 11:243–4.

Clayton, R. and Engquist, B. (1977). Absorbing boundary conditions for acoustic and elastic wave equations. *Bull. Seismol. Soc. Am.*, 67:1529–1540.

CRED (2020). Human Cost of Disaster: An Overview of the Last 20 Years (2000 - 2019). *Center for Research on the Epidemiology of Disasters and UN Office or Disaster Risk Reduction.*

Cruz-Atienza, V. M., Iglesias, A., Pacheco, J. F., Shapiro, N. M., and Singh, S. K. (2010). Crustal structure below the valley of Mexico estimated from receiver functions. *Bull. Seismol. Soc. Am.*, 100(6):3304–3311.

Cruz-Atienza, V. M., Tago, J., Sanabria-Gómez, J. D., Chaljub, E., Etienne, V., Virieux, J., and Quintanar, L. (2016). Long Duration of Ground Motion in the Paradigmatic Valley of Mexico. *Scientific Reports*, 6(December).

DDF (1975). *Memorias de las Obras del Sistema de Drenaje Profundo del Distrito Federal.* Departamento del Distrito Federal, Ciudad de México.

De Basabe, J. D., Sen, M. K., and Wheeler, M. F. (2008). The interior penalty discontinuous Galerkin method for elastic wave propagation: Grid dispersion. *Geophysical Journal International*, 175(1):83–93.

DeMets, C., Gordon, R. G., and Argus, D. F. (2010). Geologically current plate motions. *Geophysical Journal International*, 181(1):1–80.

Diaz-Rodriguez, J. A. (1989). Effects of repeated loading on the strength of Mexico City clay. In *IVth International Conference on Soil Dynamics and Earthquake*

Engineering, Mexico City.

Diaz-Rodriguez, J. A., Leroueil, S., and Aleman, J. D. (1992). Yielding of Mexico City clays and other natural clays. *Journal of Geotechnical Engineering, ASCE*, 118(7):981–995.

Diaz-Rodriguez, J. A. and Santamarina, J. (2001). Mexico City Soil Behavior at Different Strains: Observations and Physical Interpretation. *Journal of Geotechnical and Geoenvironmental Engineering*, 127(9):783–789.

Douglas, J. (2011). *Ground-motion prediction equations 1964-2010*. Report BRGM/RP-59356-FR.

Eissler, H., Astiz, L., and Kanamori, H. (1986). Tectonic Setting and Source Parameters of the September 19, 1985 Michoacan, Mexico Earthquake. *Geophysical Research Letters*, 13(6):569–572.

Emmerich, H. and Korn, M. (1987). Incorporation of Attenuation Into Time-Domain Computations of Seismic Wave Fields. *Geophysics*, 52(9):1252–1264.

Esteva, L. (1988). Mexico earthquake of September 19, 1985 - consequences, lessons, and impact on research and practice.

Faccioli, E. (1976a). A stochastic approach to soil amplification. *Bull. Seismol. Soc. Am.*, 66(August 1976):1277– 1291.

Faccioli, E. (1976b). Proyecto UNAM-UNESCO de investigación en dinámica de suelos. Technical report, Instituto de Ingeniería, UNAM.

Faccioli, E., Maggio, F., Paolucci, R., and Quarteroni, A. (1997). 2D and 3D elastic wave propagation by a pseudo-spectral domain decomposition method. *Journal of Seismology*, 1:239–248.

Faccioli, E., Tagliani, A., and Paolucci, R. (1989). Effect of Wave Propagation in Random Earth Media on the Seismic Radiation Spectrum. In *Fourth International Conference on Soil Dynamics and Earthquake Engineerin*, Mexico City.

Ferrari, L., Orozco-Esquivel, T., Manea, V., and Manea, M. (2012). The dynamic history of the Trans-Mexican Volcanic Belt and the Mexico subduction zone. *Tectonophysics*, 522-523:122–149.

Flores-Estrella, H., Yussim, S., and Lomnitz, C. (2007). Seismic response of the Mexico City Basin: A review of twenty years of research. *Natural Hazards*, 40(2):357–372.

Foti, S., Hollender, F., Garofalo, F., Albarello, D., Asten, M., Bard, P. Y., Comina, C., Cornou, C., Cox, B., Di Giulio, G., Forbriger, T., Hayashi, K., Lunedei, E., Martin, A., Mercerat, D., Ohrnberger, M., Poggi, V., Renalier, F., Sicilia, D., and Socco, V. (2018). Guidelines for the good practice of surface wave analysis: a product of the InterPACIFIC project. *Bulletin of Earthquake Engineering*, 16(6):2367–2420.

Furumura, M., Sasatani, T., and Fururuma, T. (1997). Generation of Basin-Induced Tokachi Basin , Waves Observed in the. *J. Phys. Earth*, 45:287–305.

Furumura, T. and Kennett, B. L. (1998). On the nature of regional seismic phases-

III. The influence of crustal heterogeneity on the wavefield for subduction earthquakes: The 1985 Michoacan and 1995 Copala, Guerrero, Mexico earthquakes. *Geophysical Journal International*, 135(3):1060–1084.

Furumura, T. and Singh, S. K. (2002). Regional wave propagation from Mexican subduction zone earthquakes: The attenuation functions for interplate and inslab events. *Bull. Seismol. Soc. Am.*, 92(6):2110–2125.

Galvis, F., Miranda, E., Heresi, P., Dávalos, H., and Silos, J. R. (2017). Preliminary Statistics of Collapsed Buildings in Mexico City in Puebla-Morelos Earthquake. *Technical Report*, (October):17.

García, D., Singh, S. K., Herráiz, M., Pacheco, J. F., and Ordaz, M. (2004). Inslab earthquakes of Central Mexico: Q, source spectra, and stress drop. *Bull. Seismol. Soc. Am.*, 94(3):789–802.

García-Jerez, A., Piña-Flores, J., Sánchez-Sesma, F. J., Luzón, F., and Perton, M. (2016). A computer code for forward calculation and inversion of the H/V spectral ratio under the diffuse field assumption. *Computers and Geosciences*, 97:67–78.

GCDMX (2017). *Reglamento de construcciones para la Ciudad de México*. Gobierno de la Ciudad de México, 15 de Diciembre de 2017.

Graves, R. W. (1996). Simulating seismic wave propagation in 3D elastic media using staggered-grid finite differences. *Bull. Seismol. Soc. Am.*, 86(4):1091–1106.

Hall, J. F. and Beck, J. L. (1986). Structural damage in Mexico City. *Geophysical Research Letters*, 13(6):589–592.

Hanks, T. C. (1975). Strong Ground Motion of the San Fernando, California, Earthquake: Ground Displacements. *Bulletin of the Seismological Society of America*, 65(1):193–225.

Hisada, Y. and Bielak, J. (2003). theoretical method for computing nearfault ground motions in layered half-spaces considering static offset due to surface faulting, with a physical interpretation of fling step and rupture directivity. *Bull. Seismol. Soc. Am.*, 93(3).

HRW (2011). World report 2011 Human Right Watch. Technical report, Human Rights Watch.

Hyndman, R. D. and Wang, K. (1995). The rupture zone of Cascadia great earthquakes from current deformation and the thermal regime. *Journal of Geophysical Research*, 100:22.

Iglesias, A., Singh, S. K., Pacheco, J. F., and Ordaz, M. (2002). A source and wave propagation study of the Copalillo, Mexico, earthquake of 21 July 2000 (Mw 5.9): Implications for seismic hazard in Mexico City from inslab earthquakes. *Bull. Seismol. Soc. Am.*, 92(3):1060–1071.

Iida, M. and Kawase, H. (2004). A comprehensive interpretation of strong motions in the Mexican Volcanic Belt. *Bull. Seismol. Soc. Am.*, 94(2):598–618.

Infantino, M. (2016). *From 3D Physics-Based Scenarios to Advances Methods Meth-*

ods for Seismic Hazard Assesment: The case of Istambul. Msc thesis, Politecnico di Milano.

Jaime, A. (1987). *Características Dinámicas de la Arcilla del Valle México*. Phd thesis, UNAM.

Jongmans, D., Demanet, D., Horrent, C., Campillo, M., and Sanchez-Sesma, F. J. (1996). Dynamic soil parameters determination by geophysical prospecting in Mexico City: Implication for site effect modeling. *Soil Dynamics and Earthquake Engineering*, 15(8):549–559.

Juárez-Camarena, M., Auvinet-Guichard, G., and Méndez-Sánchez, E. (2016). Geotechnical Zoning of Mexico Valley Subsoil. *Ingeniería, Investigación y Tecnología*, 17(3):297–308.

Kawase, H. and Aki, K. (1989). A study of the response of a soft basin for incident S, P, and Rayleigh waves with special reference to the long duration observed in Mexico City. *Bull. Seismol. Soc. Am.*, 79(5):1361–1382.

Kobayashi, H., Seo, K., and Midoriwaka, S. (1986). Report on seismic microzoning studies of the Mexico City earthquake of September 19, 1985. Technical report, Tokyo Institute of Technology, Yokohama, Japan.

Komatitsch, D., Tsuboi, S., and Tromp, J. (2005). The Spectral-Element Method in Seismology. *Seismic Earth: Array Analysis of Broadband Seismograms*, 157:205–227.

Komatitsch, D. and Vilotte, J. P. (1998). The spectral element method: An efficient tool to simulate the seismic response of 2D and 3D geological structures. *Bull. Seismol. Soc. Am.*, 88(2):368–392.

Kosloff, R. and Kosloff, D. (1986). Absorbing boundaries for wave propagation problems. *Journal of Computational Physics*, 63(2):363–376.

Kramer, S. L. (1996). *Geotechnical Earthquake Engineering*. Prentice-Hall, Inc.

Langridge, R., Weldon, R., Moya, J., and Suarez, G. (2000). Paleoseismology of the 1912 Acambay earthquake and the Acambay-Tixmadejé fault, Trans-Mexican Volcanic Belt. *Journal of Geophysical Research*, 105:3019–3037.

León, J. L., Jaime, A., and Rábago, A. (1974). Propiedades dinámicas de los suelos. Technical report, Instituto de Ingeniería, UNAM, Ciudad de México.

Lomnitz, C. (1990). Mexico 1985: the case for gravity waves. *Geophysical Journal International*, 102(3):569–572.

Madariaga, R. (2015). *Seismic Source Theory*, volume 4. Elsevier B.V.

Maday, Y. and Patera, A. T. (1989). Spectral element methods for the incompressible Navier-Stokes equations. In *IN: State-of-the-art surveys on computational mechanics (A90-47176 21-64). New York*, pages 71–143.

Mai, P. M., Imperatori, W., and Olsen, K. B. (2010). Hybrid broadband ground-motion simulations: Combining long-period deterministic synthetics with high-frequency multiple s-to-s backscattering. *Bull. Seismol. Soc. Am.*, 100(5 A):2124–2142.

Margottini, C. and Menoni, S. (2018). Hazard Assessment. In *Advances in Global Change Research*, volume 47, pages 1–26.

Marsal, R. and Graue, R. (1969). *El subsuelo del lago de Texcoco.* Secretaría de Hacienda y Crédito Público, México.

Marsal, R. and Mazari, M. (1959). *The subsoil of Mexico City.* Facultad de Ingeniería, UNAM, Ciudad de México.

Martínez-González, J. A., Lermo, J., Sanchez-Sesma, F. J., Angulo-Carrillo, J., Valle-Orozco, R., Ordoñez-Alfaro, J., and Pérez-Rocha, L. E. (2012). Effects of the Subsidence on the Changes of Dominant Periods of Soils within Mexico City Valley. In *15th World Conference on Earthquake Engineering.*

Martínez-Robledo, P. I. (2019). *Perfil de velocidad de onda de corte de la Ciudad de México utilizando interferometría sísmica.* Bsc. thesis, UNAM.

Mateos, J. L., Flores, J., Novaro, O., Seligman, T. H., and Alvarez-Tostado, J. A. (1993). Resonant response models for the Valley of Mexico—II. The trapping of horizontal P waves. *Geophysical Journal International*, 113(2):449–462.

Mayoral, J. M., Asimaki, D., Tepalcapa, S., Wood, C., Roman-de la Sancha, A., Hutchinson, T., Franke, K., and Montalva, G. (2019). Site effects in Mexico City basin: Past and present. *Soil Dynamics and Earthquake Engineering*, 121(March):369–382.

Mayoral, J. M., Castañon, E., Alcantara, L., and Tepalcapa, S. (2016). Seismic response characterization of high plasticity clays. *Soil Dynamics and Earthquake Engineering*, 84:174–189.

Mayoral, J. M., Hutchinson, T. C., and Franke, K. W. (2017). *Geotechnical Engineering Reconnaissance of The 19 September 2017 Mw 7.1 Puebla-Mexico City Earthquake.* Geotechnical Extreme Events Reconnaissance. Report GEER-055A.

Mazzieri, I. (2012). *Non-conforming high order methods for the elastodynamic equation.* Phd thesis, Politecnico di Milano.

Mazzieri, I., Stupazzini, M., Guidotti, R., and Smerzini, C. (2013). SPEED: SPectral Elements in Elastodynamics with Discontinuous Galerkin: a non-conforming approach for 3D multi-scale problems. *International Journal for Numerical Methods in Engineering*, 95:991–1010.

Melgar, D., Pérez-Campos, X., Ramirez-Guzman, L., Spica, Z., Espíndola, V. H., Hammond, W. C., and Cabral-Cano, E. (2018). Bend Faulting at the Edge of a Flat Slab: The 2017 Mw7.1 Puebla-Morelos, Mexico Earthquake. *Geophysical Research Letters*, 45(6):2633–2641.

Mena, E., Carmona, C., Delgado, R., Alcántara, L., and O. Domínguez (1986). Catálogo de acelerogramas procesados del sismo del 19 de Septiembre de 1985. *Series del Instituto de Ingeniería, UNAM, México.*

Mooser, F. (1975). Mapa geológico del valle de México. Technical report, Dirección General de Obras del Departamento del Distrito Federal, México.

Mooser, F. (1996). Nuevo mapa geológico de las Cuencas de México, Toluca y

Puebla. Technical report, Comisión Federal de Electricidad, México.

Munich Re (2018). TOPICS Geo, Natural catastrophes 2017. Technical report, Münchener Rück AG, München, Germany.

Nanto, D. K. and Cooper, W. H. (2011). CRS Report for Congress Japan's 2011 Earthquake and Tsunami: Economic Effects and Implications for the United States Specialist in Industry and Trade. Technical report, Congressional Research Service.

Narayan, J. P. (2005). Study of basin-edge effects on the ground motion characteristics using 2.5-D modelling. *Pure and Applied Geophysics*, 162(2):273–289.

Ordaz, M. and Singh, S. K. (1992). Source spectra and spectral attenuation of seismic waves from Mexican earthquakes, and evidence of amplification in the hill zone of Mexico City. *Bull. Seismol. Soc. Am.*, 82:24–43.

Ovando-Shelley, E. (2011). Some geotechnical properties to characterize Mexico City Clay. *Pan-Am CGS Geotechnical Conference*.

Ovando-Shelley, E., Ossa, A., and Romo, M. P. (2007). The sinking of Mexico City: Its effects on soil properties and seismic response. *Soil Dynamics and Earthquake Engineering*, 27(4):333–343.

Pacheco, J. F. and Singh, S. K. (2010). Seismicity and state of stress in Guerrero segment of the Mexican subduction zone. *Journal of Geophysical Research: Solid Earth*, 115(1):1–14.

Paolucci, R. and Faccioli, E. (1991). Analysis of Spatial Variation of Earthquake Ground Motion in the Mexico City Area. In *Fourth International Conference on Seismic Zonation*.

Paolucci, R., Gatti, F., Infantino, M., Smerzini, C., Özcebe, A. G., and Stupazzini, M. (2018). Broadband ground motions from 3D physics-based numerical simulations using artificial neural networks. *Bull. Seismol. Soc. Am.*, 108(3):1272–1286.

Paolucci, R., Mazzieri, I., and Smerzini, C. (2015). Anatomy of strong ground motion: Near-source records and three-dimensional physics-based numerical simulations of the Mw 6.0 2012 may 29 po plain earthquake, Italy. *Geophysical Journal International*, 203(3):2001–2020.

Paolucci, R., Mazzieri, I., Smerzini, C., and Stupazzini, M. (2014). Physics-Based Earthquake Ground Shaking Scenarios in Large Urban Areas. In Ansal, A., editor, *Perspectives on European Earthquake Engineering and Seismology, Geotechnical, Geological and Earthquake Engineering*, volume 34, pages 331–359.

Pardo, M. and Suarez, G. (1995). Shape of the subducted Rivera and Cocos plates in southern Mexico: seismic and tectonic implications. *Journal of Geophysical Research*, 100(B7).

Pasquaré, G., Vezzoli, L., and Zanchi, A. (1987). Morphological and structural model of Mexican Volcanic Belt. *Geofisica Internacional*, 26(6):159–176.

Patera, A. T. (1984). A spectral element method for fluid dynamics: Laminar flow in a channel expansion. *Journal of Computational Physics*, 54(3):468–488.

Pérez-Campos, X., Kim, Y. H., Husker, A., Davis, P. M., Clayton, R. W., Iglesias, A., Pacheco, J. F., Singh, S. K., Manea, V. C., and Gurnis, M. (2008). Horizontal subduction and truncation of the Cocos Plate beneath central Mexico. *Geophysical Research Letters*, 35(18).

Pérez-Cruz, G. (1988). *Estudio sismológico de reflexión del subsuelo de la Ciudad de México*. Tesis de maestría, UNAM.

Pilz, M., Parolai, S., Petrovic, B., Silacheva, N., Abakanov, T., Orunbaev, S., and Moldobekov, B. (2018). Basin-edge generated Rayleigh waves in the almaty basin and corresponding consequences for ground motion amplification. *Geophysical Journal International*, 213(1):301–316.

Quarteroni, A., Sacco, R., and Saleri, F. (2007). *Numerical Mathematics*, volume 37 of *Texts in Applied Mathematics*. Springer New York, New York, NY.

Romo, M. and Ovando-Shelley, E. (1996). Modelling the dynamic behaviour of Mexican clays. In *XI International Conference on Earthquake Engineering*.

Romo, M. P., Jaime, A., and Reséndiz, D. (1988). General Soil Conditions and Clay Properties in the Valley of Mexico. *Earthquake Spectra*, 4(4):731–752.

Rosenblueth, E. (1952). Teoría del diseño sísmico sobre mantos blandos. *Ediciones ICA, Serie B*, 14:3–12.

Rosenblueth, E., Ordaz, M., Sanchez-Sesma, F. J., and Singh, S. K. (1989). Design spectra for Mexico's Federal District.

Sanchez-Sesma, F., Chavez-Pérez, S., Suarez, M., Bravo, M., and Pérez-Rocha, L. (1988). On the seismic response of the valley of Mexico. *Earthquake Spectra*, 4(569-589).

Sánchez-Sesma, F. J., Pérez-Rocha, L. E., and Reinoso, E. (1993). Ground motion in Mexico City during the April 25, 1989, Guerrero earthquake. *Tectonophysics*, 218(1-3):127–140.

Santoyo-Villa, E., Ovando-Shelley, E., Mooser, F., and Leon-Plata, E. (2005). *Síntesis Geotécnica de la Cuenca del Valle de Mexico*, volume 1. TGC Ingeniería, México.

Seed, H. B., Romo, M. P., Sun, J. I., Jaime, A., and Lysmer, J. (1988). Mexico earthquake of September 19, 1985 - Relationships between soil conditions and earthquake ground motions.

Seligman, T. H., Alvarez-Tostado, J., Mateos, J. L., and Flores, J. (1989). Resonant response models for the Valley of Mexico-I; the elasic inclusion approach. *Geophysical Journal International*, pages 789–799.

Servicio Sismológico Nacional (2017). Sismo del día 19 de Septiembre de 2017, Puebla-Morelos (M 7.1). *Reporte Especial*, pages 1–11.

Shapiro, N. M., Campillo, M., Paul, A., Singh, S. K., Jongmans, D., and Sánchez-Sesma, F. J. (1997). Surface-wave propagation across the Mexican Volcanic Belt and the origin of the long-period seismic-wave amplification in the Valley of Mexico. *Geophysical Journal International*, 128(1):151–166.

Shapiro, N. M., Olsen, K. B., and Singh, S. K. (2002). On the duration of seismic motion incident onto the Valley of Mexico for subduction zone earthquakes. *Geophysical Journal International*, 151(2):501–510.

Shapiro, N. M., Singh, S. K., Almora, D., and Ayala, M. (2001). Evidence of the dominance of higher-mode surface waves in the lake-bed zone of the Valley of Mexico. *Geophysical Journal International*, 147(3):517–527.

Silva, V., Amo-Oduro, D., Calderon, A., Dabbeek, J., Despotaki, V., Martins, L., Rao, A., Simionato, M., Viganò, D., Yepes-Estrada, C., Acevedo, A., Crowley, H., Horspool, N., Jaiswal, K., Journey, M., and Pittore, M. (2018). Global Earthquake Model (GEM) Seismic Risk Map.

Singh, S. K., Anderson, J. G., and Rodríguez, M. (1998). Triggered seismicity in the Valley of Mexico from major Mexican earthquakes. *Geofisica Internacional*, 37(1):3–15.

Singh, S. K., Cruz-Atienza, V., Pérez-Campos, X., Iglesias, A., Hjörleifsdóttir, V., Reinoso, E., Ordaz, M., and Arroyo, D. (2018). Deadly intraslab Mexico earthquake of 19 September 2017 (Mw 7.1): Ground motion and damage pattern in Mexico City. *Seismological Research Letters*, 89(6):2193–2203.

Singh, S. K., Lermo, J., Dominguez, T., Ordaz, M., Espinosa, J. M., Mena, E., and Quaas, R. (1988a). A study of amplification of seismic waves in the valley of Mexico with respect to a hill zone site.

Singh, S. K., Mena, E., and Castro, R. (1988b). Some aspects of source characteristics of the 19 September 1985 Michoacan earthquake and ground motion amplification in and near Mexico City from strong motion data. *Bull. Seismol. Soc. Am.*, 78(2):451–477.

Singh, S. K., Mori, A., Mena, E., Krüger, F., and Kind, R. (1990). Evidence for anomalous body-wave radiation between 0.3 and 0.7 Hz from the 1985 September 19 Michoacan, Mexico earthquake. *Geophysical Journal International*, 101(1):37–48.

Singh, S. K. and Ordaz, M. (1993). On the Origin of long coda observed in the lake-bed strong-motion records of Mexico City. *Bull. Seismol. Soc. Am.*, 83(3):1298–1306.

Singh, S. K., Ordaz, M., Pacheco, J. F., Quaas, R., Alcántara, L., Alcocer, S., Gutierrez, C., Meli, R., and Ovando, E. (1999). A preliminary report on the Tehuacán, México earthquake of June 15, 1999 (Mw = 7.0). *Seismological Research Letters*, 70(5):489–504.

Singh, S. K., Ordaz, M., Pérez-Campos, X., and Iglesias, A. (2015). Intraslab versus interplate earthquakes as recorded in Mexico City: Implications for seismic hazard. *Earthquake Spectra*, 31(2):795–812.

Singh, S. K., Ordaz, M., and Pérez-Rocha, L. E. (1996). The great Mexican earthquake of 19 June 1858: Expected ground motions and damage in Mexico City from a similar future event. *Bull. Seismol. Soc. Am.*, 86(6):1655–1666.

Singh, S. K., Ponce, L., and Nishenko, S. (1985a). The great Jalisco, Mexico, earthquakes of 1932: Subduction of the Rivera plate. *Bull. Seismol. Soc. Am.*, 75(5):1301–1313.

Singh, S. K., Quaas, R., Ordaz, M., Mooser, F., Almora, D., Torres, M., and Vásquez, R. (1995). Is there truly a "hard" rock site in the Valley of Mexico? *Geophysical Research Letters*, 22(4):481–484.

Singh, S. K., Quintanar, L., Cruz-atienza, V. M., and Ordaz, M. (2020). Lessons from a Small Local Earthquake (Mw 3.2) which Produced the Highest Acceleration Ever Recorded in Mexico City. *Accepted for publication in Seismological Research Letters*.

Singh, S. K., Suárez, G., and Domínguez, T. (1985b). The Oaxaca, Mexico, Earthquake of 1931: Lithospheric normal faulting in the subducted cocos plate. *Nature*, 317(6032):56–58.

Smerzini, C. (2010). *The Earthquake Source in Numerical Modeling of Seismic Wave Propagation in Heterogeneous Earth Media*. Phd thesis, ROSE School, IUSS Pavia.

Smerzini, C. and Pitilakis, K. (2018). Seismic risk assessment at urban scale from 3D physics-based numerical modeling: the case of Thessaloniki. *Bulletin of Earthquake Engineering*, 16(7):2609–2631.

Smerzini, C. and Villani, M. (2012). Broadband numerical simulations in complex near-field geological configurations: The case of the 2009 Mw 6.3 L'Aquila earthquake. *Bull. Seismol. Soc. Am.*, 102(6):2436–2451.

SSN (2019). Secuencia sísmica del 12 al 18 de Julio De 2019, Cuenca De México (M 3.0). Technical report, Servicio Sismológico Nacional, Instituto de Geofísica, Universidad Nacional Autónoma de México, Ciudad de México.

SSN (2020). *Catálogo de sismos*. UNAM, I. d. G., Servicio Sismológico Nacional. http://www2.ssn.unam.mx:8080/catalogo/%0A%0A.

Stacey, R. (1988). Improved transparent boundary formulations for the elastic-wave equation. *Bull. Seismol. Soc. Am.*, 78(6):2089–2097.

Stupazzini, M., Paolucci, R., and Igel, H. (2009). Near-fault earthquake ground-motion simulation in the Grenoble Valley by a high-performance spectral element code. *Bull. Seismol. Soc. Am.*, 99(1):286–301.

Suarez, M., Sanchez-Sesma, F. J., Bravo, M., and Lermo, J. (1987). Características de los depósitos superficiales del Valle de México. In *VII Congreso Nacional de Ingeniería Sísmica, Querétaro, México*, pages A61–A84.

Suter, M., Lopez-Martínez, M., Quintero-Legorreta, O., and Carrillo-Martínez, M. (2001). Quaternary intra-arc extension in the central Trans-Mexican volcanic belt. *GSA Bulletin*, 113(6):693–703.

Taborda, R. and Bielak, J. (2013). Ground-motion simulation and validation of the 2008 chino Hills, California, earthquake. *Bull. Seismol. Soc. Am.*, 103(1):131–156.

Tectonics Observatory at Caltech (2009). *The unusual case of the Mexican subduction zone*. http://www.tectonics.caltech.edu/outreach/highlights/mase/.

Trifunac, M. D. (1971). Surface motion of a semi-cylindrical alluvial valley for incident plane SH waves. *Bulletin of the Seismological Society of America*, 61(6):1755–1770.

UNAM Seismology Group (1986). The September 1985 Michoacan Earthquakes: Aftershock Distribution and History of Rupture. *Geophysical Research Letters*, 13(6):573–576.

UNDRO (1980). *Natural Disasters and Vulnerability Analysis*. Report of Experts Group Meeting, Geneva.

UNDRR (2015). Sendai Framework for Disaster Risk Reduction 2015 - 2030. Technical report, United Nations Office for Disaster Risk Reduction.

United Nations (2018). The World 's Cities in 2018. Technical report, https://www.un.org/en/events/citiesday/assets/pdf/the_worlds_cities_in_2018_data_booklet.pdf.

Urbina, F. and Camacho, H. (1913). La zona megasísmica de Acambay-Tixmadejé, Estado de México, conmovida el 19 de noviembre de 1912. *Boletin de la Sociedad Geologica Mexicana*, 32.

Vazquez-Sanchez, E. and Jaimes-Palomera, R. (1989). Geologia de la Cuenca de Mexico.

White, G. F., Kates, R. W., and Burton, I. (2001). Knowing better and losing even more: The use of knowledge in hazards management. *Environmental Hazards*, 3(3):81–92.

Yamamoto, J., Jimenez, Z., and Mota, R. (1984). El temblor de huajuapan de León, Oaxaca, México, del 24 de octubre de 1980. *Geofisica Internacional*, 23(1).

Yang, T., Grand, S. P., Wilson, D., Guzman-Speziale, M., Gomez-Gonzalez, J. M., Dominguez-Reyes, T., and Ni, J. (2009). Seismic structure beneath the Rivera subduction zone from finite-frequency seismic tomography. *Journal of Geophysical Research: Solid Earth*, 114(1):1–12.

Ye, L., Lay, T., Bai, Y., Cheung, K. F., and Kanamori, H. (2017). The 2017 Mw 8.2 Chiapas, Mexico, Earthquake: Energetic Slab Detachment. *Geophysical Research Letters*, 44(23):11,824–11,832.

Zeevaert, L. (1964). Strong ground motions recorded during earthquakes of May 11th and 19th, 1962 in Mexico City. *Bull. Seismol. Soc. Am.*, 54:209–231.

Zeevaert, L. (1967). Free vibration torsion tests to determine the shear modulus of elasticity of soils. In *Third Pan-American Conference on Soil Mechanics and Foundation Engineering*, pages Vol. 1, p.III, Caracas, Venezuela.

Zienkiewicz, O. C. and Taylor, R. L. (2000). *The Finite Element Method:Its basis and Fundamentals*. Butterworth-Heinemann, Oxford, sixth edition.

Appendices

Appendix A

Basic Engineering Seismology Concepts

The earth has four major layers: the inner core, outer core, mantle and crust. The temperature of each layer increases with depth. The temperature gradient in the mantle causes the semimolten rock to move slowly by convection. The crust and the top of the mantle make up a thin skin on the surface of our planet, named Lithosphere, which is formed by many plates, called tectonic plates (Figure A.1). Shear stresses on the bottoms of the plates, caused by lateral movement of the convecting mantle, and gravitational forces cause the plates to move with respect to each other.

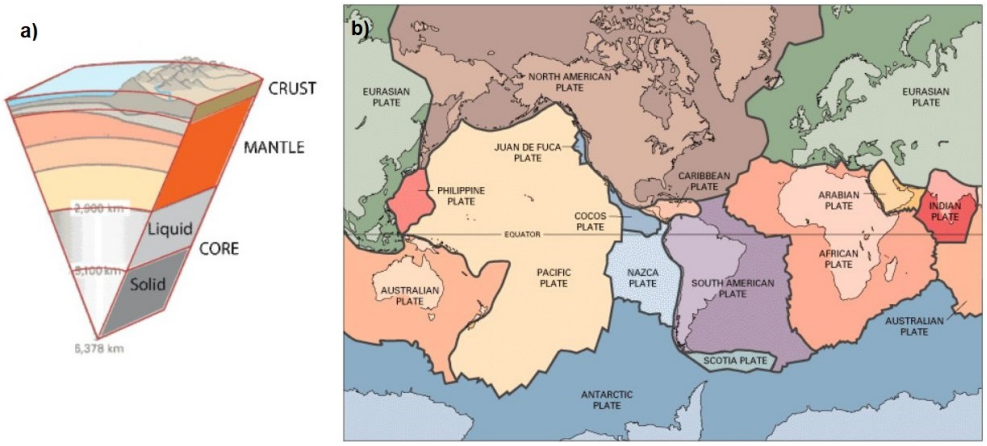

Figure A.1: (a) Diagram of the layers forming the Earth: crust, mantle, outer core and inner core; and (b) tectonic plates forming the Lithosphere.

As relative movement of the plates occurs, elastic strain energy is stored in the materials near the boundary and shear stresses increase in the fault planes that separate the plates. When the stress reaches the shear strength of the rock along the fault, the rock fails and the accumulated strain energy is released, partly in the form of heat and partly in the form of the stress waves that are felt as earthquakes. The theory of *elastic rebound* (Reid, 1911) describes this process of the successive buildup and release of strain

energy in the rock adjacent to faults. There are three main types of fault which can cause earthquakes: normal, reverse (thrust) and strike-slip (Figure A.2). The plate boundaries are made up of many faults, and most of the earthquakes around the world occur on these areas. The location below the earth's surface where the earthquake starts is called the hypocenter, and the location directly above it on the surface of the earth is called the epicenter.

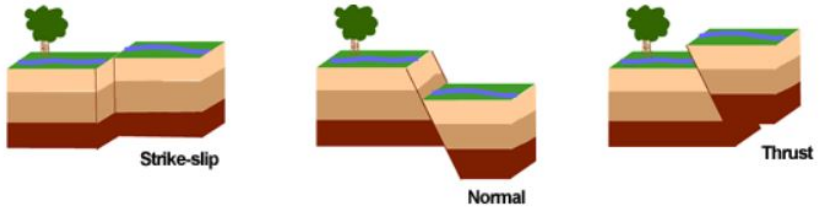

Figure A.2: Main types of faults causing earthquakes.

The effects of an earthquake at a particular location can be qualitatively measured by means of its *intensity* (e.g., Mercalli intensity), based on the observed damage and human reactions at that location such as the. The size of an earthquake can be quantitatively measured by the *earthquake magnitude*. Most of the magnitude scales are based on measured ground motion characteristics (e.g., Richter local magnitude, M_L, and Surface wave magnitude, M_S). The concept of elastic rebound theory can be used to develop a useful measure of the size of an earthquake, the moment magnitude given by

$$M_w = \frac{2}{3}\left(log10\frac{M_0}{N \cdot m} - 9.1\right) \tag{A.1}$$

where M_0 is the seismic moment of an earthquake given by

$$M_0 = \mu A\overline{D} \tag{A.2}$$

where μ is the rupture strength of the material along the fault, A the rupture area, and $\overline{D}$ the average amount of slip.

A.1 Seismic waves

When an earthquake occurs, different types of seismic waves are produced: body waves and surface waves. Body waves, which travel from the source through the interior of earth and follow paths refracted by the varying density and stiffness of the materials encountered, are of two types: P-waves and S-waves (Figure A.3). P waves are known as primary or compressional waves,

involve compression and rarefraction of the material through which they pass, and particles subjected to a P-wave move in the same direction that the wave is moving in. S-waves are transversal waves and induce on the material oscillations perpendicular to their propagating direction. The direction of particle movement can be used to subdivide S-waves into two components, SV (vertical plane movement) and SH (horizontal plane movement). The speed at which body waves travel varies with the stiffness of the materials they travel through. Since geological materials are stiffest in compression, P-waves travel faster than other seismic waves (Kramer, 1996).

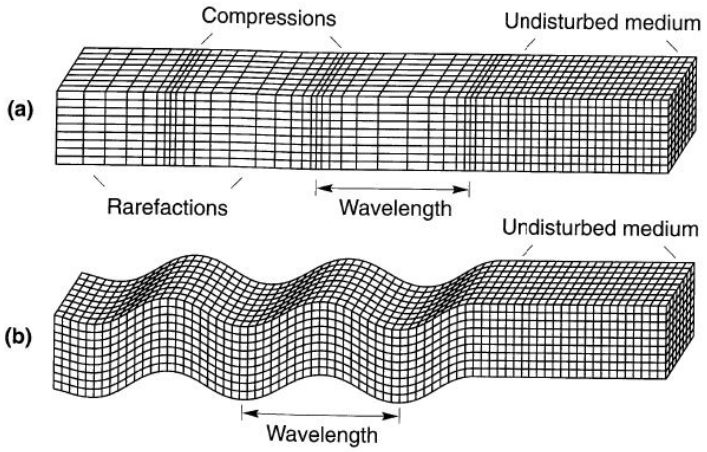

Figure A.3: Deformations produced by body waves: (a) P-wave; (b) SV-wave. [From Kramer (1996)].

Surface waves result from the interaction between body waves and the surface and surficial layers of the earth. They travel along the earth's surface with amplitudes that decrease exponentially with depth (Figure A.4). The most important surface waves, for engineering purposes, are Rayleigh waves and Love waves. Rayleigh waves, produced by the interaction of P- and SV-waves with the earth's surface, involve both vertical and horizontal particle motion. On the other hand, Love waves result from the interaction of SH-waves with a soft surficial layer and have no vertical component of particle motion (Kramer, 1996).

Surface waves are *dispersive*, i.e., harmonic waves of different wavelengths λ propagate within different depth ranges (Figure A.5a) and, hence, for each wavelength the phase velocity V depends on the elastic properties and density of the subsurface within the propagation depth range (Figure A.5b). Distribution of phase velocities as a function of frequency or wavelength is called a dispersion curve (Figure A.5c).

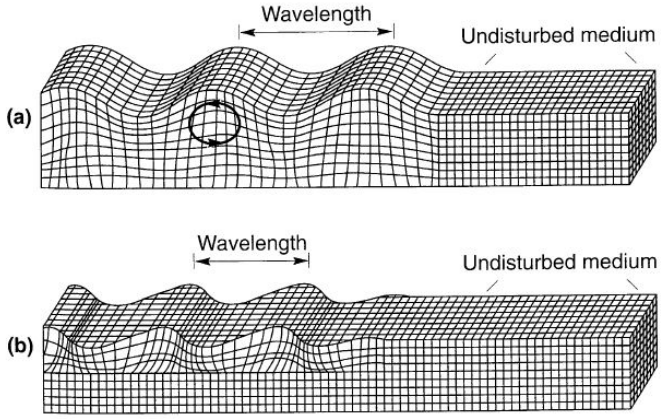

Figure A.4: Deformations produced by surface waves: (a) Rayleigh wave; and (b) Love wave. [From Kramer (1996)].

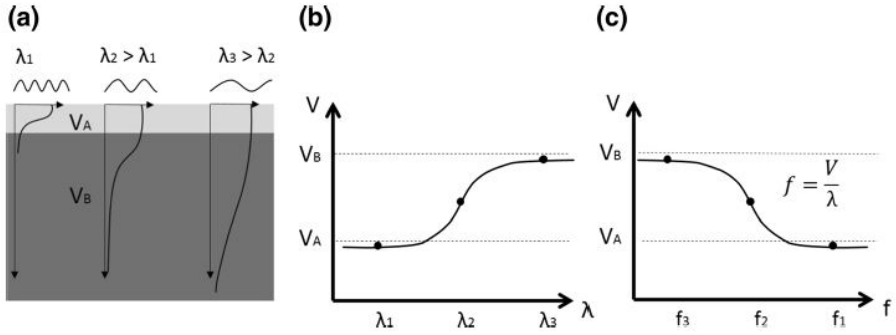

Figure A.5: Geometric dispersion of surface waves in vertically heterogeneous media: (a) qualitative sketch of amplitude decay of the fundamental mode at different wavelength; (b) dispersion curve in the wavelength- phase velocity domain; and (c) dispersion curve in the frequency- phase velocity domain. [From Foti et al. (2018)].

A.2 Strong ground motion

Evaluation of the effects of earthquakes at a particular site requires objective, quantitative ways of describing strong ground motion. Various instruments are available for ground motion measurement. Seismographs are used to measure relatively weak ground motion; the records they produce are called seismograms. Strong ground motions are usually measured by accelerographs and expressed in the form of accelerograms. For engineering purposes, three characteristics of earthquake motion are of primary significance (Kramer, 1996): (1) the amplitude, (2) the frequency, and (3) duration of the motion.

The most common way of describing a ground motion is with a time his-

tory. The motion parameter may be acceleration, velocity, or displacement. Typically, only one of these quantities is measured directly with the others computed from it by integration and/or differentiation. Peak horizontal acceleration (PHA) is the most commonly used measure of the amplitude of a particular ground motion. It is simply the largest (absolute) value of the horizontal acceleration obtained from the accelerogram of that component. Ground motions with high PHA are usually, but not always, more destructive than motions with lower peak accelerations.

Any periodic function $x(t)$ with period T_f can be expressed as Fourier series, that are the sum of a series of simple harmonic terms of different frequency, amplitude and phase

$$x(t) = \sum_{n=-\infty}^{\infty} c_n e^{i\omega_n t} \tag{A.3}$$

where $\omega_n = 2\pi n/T_f$, and the complex Fourier coefficients, c_n, can be determined directly from $x(t)$ as

$$c_n = \frac{1}{T_f} \int_0^{T_f} x(t) e^{-i\omega_n t} dt \tag{A.4}$$

A plot of Fourier amplitude ($2|c_n|$) versus frequency (ω_n) is known as a Fourier amplitude spectrum. Considering an accelerogram as one cycle of a function with very long period, its frequency content, describing how the amplitude of a ground motion is distributed among different frequencies, can be described by its Fourier amplitude spectrum.

The duration of strong ground motion can have a strong influence on earthquake damage. A motion of short duration may not produce enough load reversals for damaging response to build up in a structure, even if the amplitude of the motion is high (Kramer, 1996). Significant duration may be computed from the *bracketed duration*, defined as the time between the first and the last exceedances of a a threshold acceleration (usually 0.05g); or from the time interval between the 5% and the 95% of the Arias intensity I_a, computed as

$$I_a = \frac{\pi}{2g} \int_0^{\infty} [a(t)]^2 dt \tag{A.5}$$

Figure A.6a shows six accelerograms from earthquakes of different magnitude, recorded at about the same distance from the source. The influence of earthquake magnitude on duration and amplitude are evident. In Figure

A.6b are shown the Fourier spectra of the same accelerograms fro which a clear a difference in frequency content is visible. Large earthquakes produce greater low-frequency motions than do smaller earthquakes.

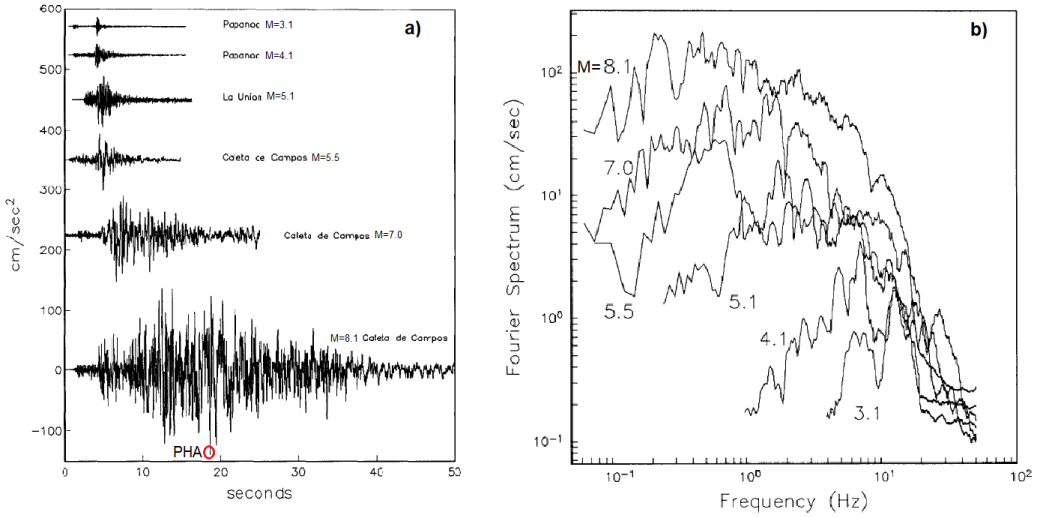

Figure A.6: (a) Accelerograms from events with different magnitude in the Pacific coast of Mexico, recorded at about 25 km from the corresponding epicenter; and (b) Fourier amplitude spectra for the same accelerograms. [From Anderson and Quaas (1988)].

A.3 Ground motion prediction equations

Ground motion prediction equations (GMPEs), are commonly used to estimate ground motion parameters (Y) as functions of magnitude (M), distance from source to site (R), and in some cases other variables (P_i, used to characterize the earthquake source, wave propagation path, and/or local site conditions), for example

$$Y = f(M, R, P_i)$$

GMPEs are developed by regression analyses of recorded strong motion databases. As such, they change with time as additional strong motion data become available. The functional form of the predictive relationship is usually selected to reflect the mechanics of the ground motion process as closely as possible. Common forms for predictive relationships are based on the following observations (Kramer, 1996)

1. Peak values of strong ground motion parameters are approximately lognormally distributes. As a result, the regression is usually performed on the logarithm of Y rather than on Y itself

2. Earthquake magnitude M is typically defined as the logarithm of some peak motion parameter. Consequently, ln Y should be approximately proportional to M.

3. The spreading of stress waves as they travel away from the source of an earthquake causes body wave amplitudes to decrease according to 1/R and surface wave amplitudes to decrease according to $1/\sqrt{R}$.

4. The area over which a fault rupture occurs increases with increasing magnitude. As a result, some of the waves arrive from a distance, R, and some arrive from greater distances. The effective distance, therefore, is greater that R by an amount that increases with increasing magnitude.

5. Some of the energy carried by stress waves is absorbed by the materials they travel through (material damping). This material damping causes ground motion amplitudes to decrease exponentially with R.

6. Ground motion parameters may be influenced by source characteristics (e.g., strike-slip, normal or reverse faulting) or site characteristics (e.g., hard rock, soft rock, alluvium, etc.).

Combining these observations, a typical GMPE may have the form

$$ln\,Y = C_1 + C_2 M + C_3 M^{C_4} + C_5 ln[R + C_6 exp(C_7 M)] + C_8 R + f(source) + f(site) \tag{A.6}$$

A.4 Response spectrum

A simple way to represent a structure is with a Single Degree of Freedom System (SDOF, Figure A.7), with mass m, stiffness k and damping ratio ξ. The dynamic equilibrium equation for the SDOF is

$$m\ddot{x}(t) + c\dot{y}(t) + ky(t) = 0\ddot{y}(t) = 2\omega_n \xi \dot{y}(t) + \omega_n^2 y(t) = -\ddot{u}(t) \tag{A.7}$$

where $\omega_n = \sqrt{k/m}$ is the natural frequency of the SDOF, $\xi = c/2m\omega_n$ is the damping ratio, $x(t)$ is the absolute displacement of the SDOF, $u(t)$ is the absolute displacement of the support, and $y(t) = x(t) - u(t)$ is the relative displacement of the SDOF.

The solution of the dynamic equilibrium equation (A.7) for a given excitation (earthquake) gives us the response of the system. The general solution

of (A.7) is composed by the complementary solution (y_h, free vibrations) and the particular solution (y_p, forced vibrations, Duhamel's integral) as follows

$$y(t) = y_h(t) + y_p(t) =$$
$$e^{-\xi\omega_n t}(Asin\omega_d t + Bcos\omega_d t) - \frac{1}{\omega_d}\int_0^t \ddot{u}(\tau)e^{-\xi\omega_n(t-\tau)}sin\omega_d(t-\tau)d\tau \quad \text{(A.8)}$$

where $\omega_d = \omega_n\sqrt{1-\xi^2}$ is the damped circular frequency of the SDOF, and constants A and B are determined based on the initial conditions.

However, in practice, the dynamic equilibrium equation is integrated using a numerical method, e.g., Newmark's method.

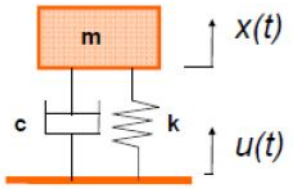

Figure A.7: Single degree of freedom system (SDOF).

The response spectrum (Figure A.8), concept initiated by M. A. Biot (1932) and widespread by G. W. Housner, provides a convenient means to summarize the peak response of all possible linear SDFS to a particular component of ground motion. A plot of the peak value of a response quantity as a function of the natural vibration period T_n of the system, is called the response spectrum for that quantity. Such plot is for SDOF systems having a fixed damping ratio, usually 5% (Chopra, A., 1995). Response spectra reflect strong ground motion characteristics indirectly, since they are filtered by the response of a SDOF structure (Kramer, 1996).

A.5 One-dimensional ground response analysis

One-dimensional ground response analyses are based on the assumption that all boundaries are horizontal and that the response of a soil deposit is predominantly caused by SH-waves propagating vertically from the underlying bedrock.

The ground response analysis can be made in the frequency domain with the use of transfer functions. The transfer functions are a way to represent the frequencies that a soil deposit amplifies. If the input motion (bedrock) is represented as a Fourier amplitude spectrum and multiplied by the transfer

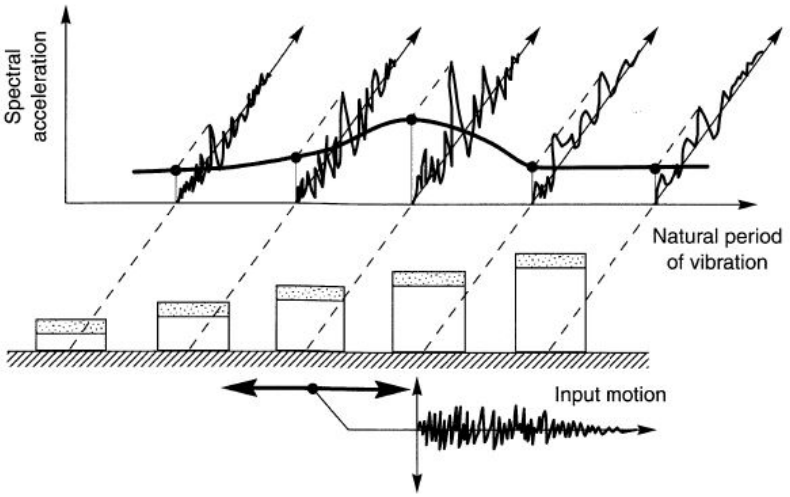

Figure A.8: Response spectrum. Spectral accelerations are the maximum acceleration amplitudes of SDOF systems in response to the same input motion. The response spectrum is obtained by plotting the spectral accelerations against the periods of vibrations of the SDOF systems. [From Kramer (1996)].

function of the soil deposit through which the motion has been propagated, it's possible to obtain the Fourier spectrum on the ground surface. Applying the inverse Fourier transform to the ground surface motion, the output motion can be obtained in the time domain.

Considering an homogeneous elastic soil layer of thickness H overlying an elastic half-space, excited by an unitary harmonic plane shear wave traveling in the x direction and giving rise to a displacement field v that acts only in the y direction is considered, the dynamic equilibrium equation of the problem is

$$\frac{\partial \tau_{xy}}{\partial x} = \rho \frac{\partial^2 v}{\partial t^2} \tag{A.9}$$

Using the constitutive law of the elastic medium, equation (A.9) can be expressed as follows

$$\tau_{xy} = \mu \cdot \gamma_{xy} = \mu \cdot \frac{\partial v}{\partial x} \rightarrow \frac{\partial^2 v}{\partial x^2} = \frac{1}{\beta^2} \frac{\partial^2 v}{\partial t^2}$$

where μ is the shear modulus, ρ is the mass density, and $\beta = \sqrt{\mu/\rho}$ is the shear wave velocity.

Since the applied stresses are harmonic, the general solution of the wave equation is

$$v = A(\omega)e^{i\omega(t+x/\beta)} + B(\omega)e^{i\omega(t-x/\beta)} \tag{A.10}$$

Let β_1 and β_2 denote the shear wave velocities in the soil layer and in the elastic half-space, respectively, ρ_1 and ρ_2 the corresponding mass densities, and $v_1(x,t)$, $v_2(\xi,t)$ the associated displacements (Figure A.9), then

$$v_1 = A(\omega)e^{i\omega(t+x/\beta_1)} + B(\omega)e^{i\omega(t-x/\beta_1)}$$

$$v_2 = (\omega)e^{i\omega(t+\xi/\beta_2)} + B(\omega)e^{i\omega(t-\xi/\beta_2)}$$

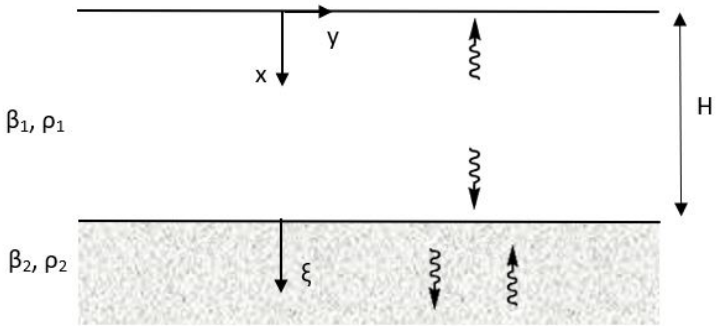

Figure A.9: Geometry of the soil layer overlying an elastic halfspace.

Applying the free surface boundary condition

$$\mu_1 \frac{\partial v_1}{\partial x}(x=0) = 0 \rightarrow \frac{i\omega}{\beta_1}A(\omega)e^{i\omega t} - \frac{i\omega}{\beta_2}B(\omega)e^{i\omega t} = 0 \rightarrow A(\omega) = B(\omega) \tag{A.11}$$

Applying equality of displacements at the contact of the soil layer with the elastic half-space

$$v_1(H,t) = v_2(0,t) \rightarrow A(\omega)e^{i\omega\frac{H}{\beta_1}} + A(\omega)e^{-i\omega\frac{H}{\beta_1}} = 1 + C$$

$$\text{using } cos(\omega) = \frac{e^{i\omega} + e^{-i\omega}}{2} \rightarrow 2Acos\left(\omega\frac{H}{\beta_1}\right) = 1 + C \tag{A.12}$$

Applying equilibrium at the contact of the soil layer with the elastic half-space

$$\rho_1\beta_1^2\frac{\partial v_1}{\partial x}(x=H) = \rho_2\beta_2^2\frac{\partial v_2}{\partial \xi}(\xi=0) - 2\eta Asin\left(\omega\frac{H}{\beta_1}\right) = i(1-c) \tag{A.13}$$

where $\eta = \frac{\rho_1\beta_1}{\rho_2\beta_2}$ is the impedance ratio. Summing (A.12) and (A.13)

$$2A\left[cos\left(\omega\frac{H}{\beta_1}\right)+i\eta sin\left(\omega\frac{H}{\beta_1}\right)\right]=(1+C)+(1-C)=2$$

$$A=\frac{1}{cos\left(\omega\frac{H}{\beta_1}\right)+i\eta sin\left(\omega\frac{H}{\beta_1}\right)}$$

Hence

$$v_1(x,t)=\frac{2cos\left(\omega\frac{x}{\beta_1}\right)}{cos\left(\omega\frac{H}{\beta_1}\right)+i\eta sin\left(\omega\frac{H}{\beta_1}\right)}e^{i\omega t} \tag{A.14}$$

Finally, the transfer or amplification function $F(\omega)$ (Figure A.10 defined as the ratio of the soil surface displacement amplitude to the bedrock displacement amplitude is

$$|F(\omega)|=\frac{1}{\sqrt{cos^2\left(\omega\frac{H}{\beta_1}\right)+\eta^2 sin^2\left(\omega\frac{H}{\beta_1}\right)}} \tag{A.15}$$

From which, for the natural frequencies $f_n=(2n+1)\beta_1/4H$, being the fundamental frequency $f_0=\beta_1/4H=0.5\,Hz$, the maxima of amplification is obtained

$$|F(f_n)|=\frac{1}{\eta}=\frac{\rho_2\beta_2}{\rho_1\beta_1}$$

Considering a rigid bedrock, i.e., η=0, the transfer function is simplified as

$$|F(\omega)|=\frac{1}{|cos\left(\omega\frac{H}{\beta_1}\right)|} \tag{A.16}$$

From which $|F(f_n)|=\infty$.

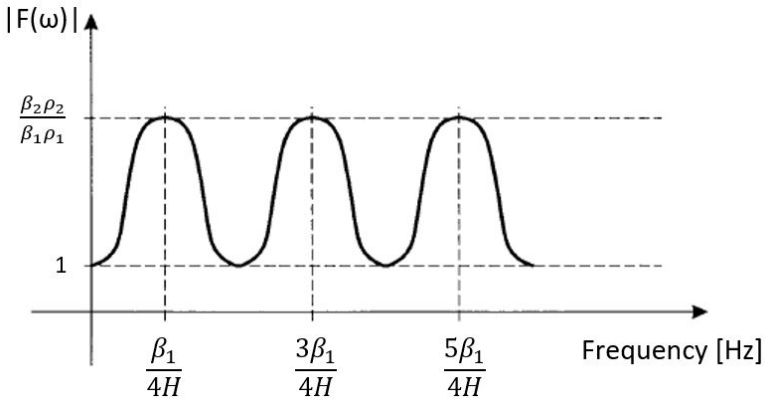

Figure A.10: Transfer function for a soil layer overlying an elastic half-space.

The concept of transfer function just presented can be extended to a more realistic case in which a dissipation of elastic energy is consider, by means of the Kelvin-Voigth constitutive model (visco-elastic model)

$$\tau = \mu\gamma + \eta\dot{\gamma}$$

where η is the viscosity of the material.